Measurement of $\sigma \cdot B(W \to \mu\nu)$, $\sigma \cdot B(Z^0 \to \mu^+\mu^-)$ and $R_\mu = \sigma \cdot B(W \to \mu\nu)/\sigma \cdot B(Z^0 \to \mu^+\mu^-)$ and Extraction of $BR(W \to \mu\nu)$ and $\Gamma(W)$ in $p\bar{p}$ Collisions at $\sqrt{s} = 1.8$ TeV

by

William Farris Badgett, Jr.

A dissertation submitted in partial fulfillment
of the requirements for the degree of
Doctor of Philosophy
(Physics)
in The University of Michigan
1994

Doctoral Committee:

Associate Professor Myron K. Campbell, Chair
Professor Carl W. Akerlof
Professor J. Wehrley Chapman
Associate Professor Richard L. Sears
Professor York-Peng E. Yao

AAD6340

" *Freedom, free reason, and science will lead them into such a maze, and confront them with such miracles and insoluble mysteries...* "

Fyodor Dostoevsky, The Brothers Karamazov *[1]*

— ◇ —

" *My Sallade dayes,*
When I was greene in judgement, cold in blood,
To say, as I saide then. "

William Shakespeare, Antony and Cleopatra *[2]*

— ◇ —

" *For of such Doctrine never was there School,*
But the heart of the Fool,
And no man therein Doctor but himself.
Yet more there be who doubt his ways not just,
As to his own edicts, found contradicting,
Then give the rains to wandring thought,
Regardless of his glories diminution ;
Till by thir own perplexities involv'd
They ravel more, still less resolv'd,
But never find self-satisfying solution. "

John Milton, Samson Agonistes *[3]*

Acknowledgments

Within the range of a dissertation, I necessarily cannot convey the scope of all the work required to produce the data analyzed herein. Without the dedicated effort of many of the members of the CDF collaboration and of those of the Fermilab Accelerator Division, the data run would not have been possible. The chapter describing the detector will give no hint of the effort required to acquire the data: the months of commissioning time; the long hours of debugging the system; the phone calls from the control room in the middle of the night; and the painstaking verification of the data quality – all of this taking place in a demanding, highly charged environment. All of the people involved have my sincerest thanks.

My work on the CDF trigger was a collaborative effort, for which I thank Myron (my advisor), Soo Bong and David. Together we got through the insanity of that long commissioning period, defeating the multi-headed Hydra in the end (I'm not going to say that word!). Special thanks go to Kevin, who assumed my responsibilities towards the end of the run with such ease, and for being willing to commiserate about being caught in the maelstrom.

For pushing me forward in the early stages of my analysis and for taking an interest in my work, I thank Sarah. The CDF electroweak group lost a very fine convener after she left for Maryland. Acknowledgment also goes to the all the people that blazed the trail of the muon analysis during the 1988-89 run.

Thanks go to Jay (my first advisor) for giving me my first opportunity in experimental HEP on the SDC test beam and to Myron (my second advisor) for introducing me to the world of CDF.

Of course, to get this far I had to pass through the early days of graduate school. Getting through those all-night problem set sessions probably wouldn't have been possible without the company of others in my class: Leah, Chris, Jim, Ofer, Uli, Mark, Rich. In the later years, we all must thank Ofer for taking on the rôle of the ultimate grad student guru.

Thanks to my family, Mom, Dad, Lee, Ann, Branden (rest in peace), and Helix, for providing moral support even when I didn't do a good job of explaining what I was doing. And to Andy, your friendship was invaluable, especially in those dark days when I complained too much, and to you and Paula for providing a window outside the sometimes hermetic world of physics. And thanks to Thomas for being around, even when far away.

Table of Contents

Acknowledgments ii

List of Tables vii

List of Figures viii

List of Appendices x

Chapter

1. Introduction 1
- 1.1 The Electroweak and Kinematic Regime at the Tevatron 2
- 1.2 Theory Motivation for Measurement 3
- 1.3 Outline of Paper 6

2. Description of the Experimental Apparatus 8
- 2.1 The Tevatron at Fermilab 8
- 2.2 Overview of the CDF Detector 10
- 2.3 Muon Chambers 13
- 2.4 Tracking Systems 16
- 2.5 Calorimeters 18
- 2.6 Hardware Trigger 19
  - 2.6.1 Level 1 20
  - 2.6.2 Level 2 23
  - 2.6.3 Level 3 25

3. Event Selection 27
- 3.1 W and Z Decay Characteristics 27
- 3.2 $W \rightarrow \mu\nu$ Identification 28
- 3.3 $Z \rightarrow \mu\mu$ Identification 29
- 3.4 Experimental Cross Section Measurement 30
- 3.5 Inclusive Muon Identification Variables 31
  - 3.5.1 Parameter Definitions 34
  - 3.5.2 Hadronic Particle Rejection 36
  - 3.5.3 Fiducial and Quality Cuts 38
- 3.6 Primary Muon Selection 40
- 3.7 Z Candidate Events 42
- 3.8 W Candidate Events 43

3.9 Inclusive Muons from non W and Z Processes 44

4. Geometric and Kinematic Acceptance 54
4.1 Monte Carlo Generator and Detector Model 56
4.2 Systematic Uncertainties 58
4.2.1 Parton Distribution Functions 58
4.2.2 M_W and $sin^2\theta_W$ 59
4.2.3 Boson P_T Distribution 60
4.2.4 Underlying Event Model 61
4.2.5 Track Curvature and Polar Angle Smearing 62
4.2.6 Event z Vertex Distribution 62
4.3 Summary of Acceptances and Uncertainties 64
4.4 Comparison to Data 64

5. Detector and Identification Efficiencies 67
5.1 Muon Selection Efficiencies 67
5.2 Muon Identification Cut Efficiencies 68
5.3 Trigger Efficiencies 69
5.3.1 Level 1 Efficiency 70
5.3.2 Level 2 Efficiency 70
5.3.3 Level 3 Efficiency 72
5.3.4 Combined Trigger Efficiency 73
5.4 Detector Efficiencies 73
5.4.1 Tracking Efficiencies 73
5.4.2 Muon Chamber Efficiencies 74
5.5 Combined Results 75
5.5.1 Combined Muon Identification Efficiencies 76
5.5.2 Combining W,Z and R_μ Efficiencies 76

6. Backgrounds to W and Z Production 81
6.1 W Backgrounds 81
6.1.1 General QCD Backgrounds to $W \to \mu\nu$ 81
6.1.2 Modelling QCD Backgrounds 84
6.1.3 $Z \to \mu\mu$ Lost Muon W Backgrounds 85
6.1.4 Cosmic Ray Background 86
6.1.5 $W \to \tau\nu$ and $Z \to \tau\tau$ Backgrounds 87
6.1.6 Top Quark Production as potential W Background 88
6.2 Z Backgrounds 88
6.2.1 Cosmic Ray Background to Z 89
6.2.2 General QCD Background to Z 89
6.2.3 $Z \to \tau\tau$ Background to Z 90
6.3 Drell Yan Correction to Z Cross Section 90
6.4 Summary of W and Z Backgrounds 91

7. Luminosity 96
7.1 Luminosity Measurement and Normalization 96
7.2 Sources of Error 99
7.3 Event Vertex Correction 99

7.3.1 Vertex Distribution Models 99
7.3.2 Computing the Event Vertex Correction 102
7.3.3 Uncertainties in the Event Vertex Correction 103

8. Results and Conclusions 106
8.1 Measurement of Cross Sections 106
8.2 Measurement of R_μ 107
8.3 Extraction of $BR(W \rightarrow \mu\nu)$ and $\Gamma(W)$ 108
8.4 Limits on Unknown Decay Channels 109
8.5 Conclusions 110

Appendices 115

References 124

List of Tables

Table

2.1 Tracking and Muon Chambers, Coverage and Resolution 16
2.2 Calorimeter Components, Coverage and Resolution 18

3.1 Processes Contributing to the High P_T Inclusive Muon Sample 31
3.2 Inclusive Muon Selection Cuts 34
3.3 Primary Muon Selection Cuts 40
3.4 Z Candidate Cuts 47
3.5 Z Candidate Secondary Muon Classifications 47
3.6 W Candidate Secondary Muon Classifications 48

4.1 Effect of Parton Distribution Functions on Acceptances 59
4.2 Effect of W Mass on Acceptances 59
4.3 Effect of Boson P_T on Acceptance 60
4.4 Effect of Underlying Event Model on Acceptance 61
4.5 Effect of Track Smearing on Acceptance 63
4.6 Effect of Event z Vertex Distribution on Acceptance 63
4.7 Summary of Acceptance Uncertainties 64

5.1 Basic Muon Identification Efficiencies 69
5.2 Level 2 Trigger Studies 72
5.3 Trigger Efficiencies 73
5.4 Chamber Efficiencies 75
5.5 Combined Efficiencies 75

6.1 Regions in the $\not\!\!E_T$ vs. $E_T(0.4)$ Plane 82
6.2 $W \rightarrow \mu\nu$ General QCD Backgrounds 84
6.3 $W \rightarrow \mu\nu$ Backgrounds 95
6.4 $Z \rightarrow \mu\mu$ Backgrounds 95

7.1 Variation of ϵ_{vertex} 105

8.1 Summary of Results 109
8.2 Sources of Error 111

List of Figures

Figure

2.1 Diagram of the Tevatron and associated Accelerators 9
2.2 Isometric View the CDF Detector 10
2.3 Longitudinal Profile of the CDF Detector 12
2.4 Central Muon Drift Chambers, Sectional View 14
2.5 Central Muon Chambers, 15° Wedge (left) and Longitudinal Extent (right) . 15
2.6 Central Tracking Chamber, Endplate View 17

3.1 Dominant W and Z Production Processes with Muonic Decay 28
3.2 Predicted Muon Calorimeter Energy Deposition 32
3.3 Predicted Muon Track Matching Parameter δx, CMU Chambers (left) and CMP Chambers (right) 36
3.4 Comparison of Muon and Pion Energy Deposition (left) and Track Matching (right) 38
3.5 Inclusive Muon Transverse Momentum Spectrum 40
3.6 Inclusive Muon Energy Deposition 41
3.7 Inclusive Muon Track Matching 42
3.8 Inclusive Muon z Vertex Quantities 43
3.9 Monte Carlo Prediction, Isolation vs. $\not{E}_T$, Background (left) and Signal (right) 44
3.10 Primary Muon Matching Quantities 45
3.11 Primary Muon Isolation and Missing Transverse Energy 46
3.12 Dimuon Mass Spectrum with Z Candidates 48
3.13 W Candidates Transverse Mass Spectrum 49
3.14 Muon Transverse Momentum Spectra by Class 50
3.15 Predicted $b \rightarrow \mu + X$ Muon P_T Spectrum 51
3.16 Extraction of Punch through Transverse Momentum Spectrum 52
3.17 Predicted Non-Isolated or Low $\not{E}_T$ W Muon P_T Spectrum 52
3.18 Fit of Non W and Z Muon P_T Spectrum to Two Exponentials 53
3.19 Fit of Non W and Z Muon P_T Spectrum to Models 53

4.1 Fiducial Response Regions of the Central Muon Chambers 55
4.2 Associated Gluon Jet Production Processes and Gluon Vertex Correction . . 61
4.3 W Candidates ϕ and η Distributions 65
4.4 Z Candidates η Distribution 66

5.1 $W \rightarrow e\nu$ CFT Efficiencies 72
5.2 Tracking Efficiency vs. Pseudorapidity 79

6.1 Isolation vs. Missing Transverse Energy 92
6.2 Average Isolation vs. Missing Transverse Energy, Various Jet Requirements 93
6.3 Missing Transverse Energy: from $b \rightarrow \mu + X$ Monte Carlo (left); data with fit to signal and background (right) 94
6.4 Z Candidates Muon Isolation 94
6.5 Comparison of Z and $Z + \gamma$ Dimuon Mass Spectra for Drell Yan Correction 95

7.1 Instantaneous Luminosity Profile 97
7.2 Event Vertex Distributions, Single and All Runs 100
7.3 Variation of ϵ_{vertex} and fit quality with β^*_{eff} 103
7.4 Best Luminosity Curve compared with min-bias z distribution, fit region and full region 105

8.1 W and Z Cross Sections vs. $p\bar{p}$ Center of Mass Energy 112
8.2 Comparison of W Total Width to Theory and other Experiments 113
8.3 Top Quark Mass vs. Inverse Branching Ratio 114

List of Appendices

Appendix

A. Prospects for Future Measurements . . . 116
A.1 Immediate Prospects for Cross Section Measurements . . . 116
A.1.1 Improvements . . . 116
A.1.2 Disadvantages . . . 117
A.2 Prospects for Direct W Width Measurement . . . 118
A.3 Far Future Prospects for W Physics . . . 118

B. CDF Collaboration . . . 120

Chapter 1

Introduction

Just over ten years have past since the UA1 Collaboration reported the first evidence for direct production of the W and Z bosons at the CERN $S\bar{p}pS$ proton-antiproton collider [4]. The intervening years have brought continuing highly successful confirmation of the unified theory governing the interactions of matter with the electroweak fields γ (photon), $W^{\pm}$ and Z^0. Following the $S\bar{p}pS$ collider and continuing today, the Tevatron proton-antiproton collider at Fermilab; the LEP electron-positron collider at CERN; and the SLC electron-positron collider at SLAC all provide unprecedented precision measurements of the standard model of electroweak interactions through direct production of W and Z bosons, complementing fixed target studies of charged and neutral current interactions.

Such success represents remarkable confirmation of this unified electroweak theory, first proposed by Glashow [5], Weinberg [6] and Salam [7]. The roots of electroweak theory go back to Fermi's four point theory of muon decay [12] in 1933 and Klein's first proposal of the existence of an W boson mediating the reaction [13] in 1938. In 1954, Yang and Mills [14] paved the way with their work on non-Abelian massless gauge fields. In the following few years, Nambu [8], Goldstone [9] and Higgs [10] extended the Yang-Mills theory with symmetry breaking mechanisms, explaining how the gauge fields can acquire mass. The critical final theoretical development by t 'Hooft [11] in 1971 proved that the unified electroweak theory is renormalizable. The first reported experimental evidence for weak neutral currents [15] in 1974 provided evidence of the existence of the intermediate neutral weak boson, the Z^0, setting the stage for the subsequent searches for direct W and Z boson production. With electroweak theory, combined with quantum chromodynamics (QCD) describing the strong interactions of quarks, we have the standard model of fundamental particle interactions.

With the discovery of the direct production of W and Z bosons established, we are able to make numerous precision tests of the various quantities predicted by the standard model. The thesis of this paper is a measurement of the W and Z boson cross sections produced in proton-antiproton collisions at a center of mass energy of $\sqrt{s} = 1.8\ TeV$, in the muon decay channel:

$$\sigma(p\bar{p} \to W \to \mu\nu) \qquad \sigma(p\bar{p} \to Z \to \mu^+\mu^-)$$

Electroweak theory, combined with the proton's parton momentum distribution functions and QCD production corrections, predicts with precise theoretical accuracy the W and Z cross sections and muonic decays rates. We also measure the ratio of cross sections:

$$R_\mu = \frac{\sigma(p\bar{p} \to W \to \mu\nu)}{\sigma(p\bar{p} \to Z \to \mu^+\mu^-)}$$

From the ratio, we are able to extract the W total width and the $W \to \mu\nu$ branching ratio, which represent a precision test primarily of the electroweak sector of the standard model.

1.1 The Electroweak and Kinematic Regime at the Tevatron

Today the ongoing operation of the Tevatron collider at a center of mass energy of $\sqrt{s} = 1.8\ TeV$ allows the direct production of real (non-virtual) W and Z bosons through the process of quark-antiquark annihilation, as indicated in the diagrams of figure 3.1. The LEP and SLC electron positron colliders, operating at the Z resonance, are capable of producing copious Z bosons, but the Tevatron is currently the only collider which can create on shell W bosons.

The hard scattering production processes $p\bar{p} \to W$ and $p\bar{p} \to Z$ probe the distribution of the partons making up the proton and antiproton. At $\sqrt{s} = 1.8\ TeV$, the interaction of sea and valence quarks dominates [38] W and Z production with a typical parton momentum fraction, x, and momentum transfer squared, Q^2:

$$x \sim \frac{M_{W,Z}}{\sqrt{s}} \sim 0.05 \quad Q^2 \sim M^2_{W,Z}$$

This kinematic regime of proton-antiproton collisions is unique to the Tevatron. The momentum fraction is quite distinct from the $S\bar{p}pS$ collider operating at $\sqrt{s}$ = 540 GeV or $\sqrt{s}$ = 630 GeV. The Q^2 regime is far above that found in deep-inelastic neutrino experiments.

As we shall see in the following chapters, precision electroweak measurements tend to be statistics limited. Therefore, collecting ever larger samples of W and Z decay candidates allows successively better tests of the theory, all in a unique kinematic regime of the standard model.

1.2 Theory Motivation for Measurement

The measured W and Z cross sections in the muon decay channel can be factored into two parts: the W and Z production cross sections in proton-antiproton collisions at $\sqrt{s} = 1.8\ TeV$, and the muonic branching ratios of the W and Z:

$$\sigma(p\bar{p} \to W) \cdot B(W \to \mu\nu) \qquad \sigma(p\bar{p} \to Z) \cdot B(Z \to \mu^+\mu^-)$$

The process $p\bar{p} \to W$ is factored in terms of the process $q\bar{q}' \to W$ with the inclusion of the parton distribution functions and the rapidity dependence y [38]:

$$\frac{d\sigma}{dy}(p\bar{p} \to W^+ + X) = K(y)\frac{2\pi G_F}{3\sqrt{2}}\times$$

$$x_1x_2(\cos^2\theta_C[u(x_1)d(x_2) + \bar{d}(x_1)\bar{u}(x_1)] + \sin^2\theta_C[u(x_1)s(x_2) + \bar{s}(x_1)\bar{u}(x_2)])$$

$$x_1 = \frac{M_W}{\sqrt{s}}e^y \qquad x_2 = \frac{M_W}{\sqrt{s}}e^{-y}$$

Similarly, we have an equivalent expression for the Z cross section. (A more detailed expression for the leading order contribution is given in chapter 4.) Through the $K(y)$ factor, the production cross sections also tests QCD theory with associated jet production through higher order diagrams as indicated in figure 4.2. The K factor can be expressed in terms of several constituent processes:

$$K(y) = \frac{\sigma_{DY}(y) + \sigma_{gr} + \sigma_{gv}(y) + \sigma_{qg}(y)}{\sigma_{DY}}$$

where we have: σ_{DY} as the lowest order process (figure 3.1); σ_{gr} associated real gluon radiation (figure 4.2 left); σ_{gv} gluon vertex correction (figure 4.2, right); and σ_{qg} quark gluon scattering (figure 4.2, center). Similar but more complicated diagrams exist at higher order. (See reference [53].)

One of the more interesting numbers that can be measured from W and Z production in the muon decay channel is the ratio of cross sections. The ratio can be expressed as:

$$R_\mu = \frac{\sigma \cdot B(W \to \mu\nu)}{\sigma \cdot B(Z \to \mu\mu)} = \frac{\sigma(W)}{\sigma(Z)} \cdot \frac{\Gamma(W \to \mu\nu)}{\Gamma(W)} \cdot \frac{\Gamma(Z)}{\Gamma(Z \to \mu\mu)}$$

Where $\sigma(W)$ and $\sigma(Z)$ are the production cross sections. From this ratio, we can extract a number of important electroweak parameters. We take the ratio of production cross sections and the ratio of partial widths from theory:

$$\frac{\sigma(W)}{\sigma(Z)} = 3.33 \pm 0.03 \quad [50] \qquad \frac{\Gamma(W \to \mu\nu)}{\Gamma(Z \to \mu\mu)} = 2.696 \pm 0.018 \quad [48]$$

The four LEP experiments, operating around the $e^+e^- \to Z$ resonance, have measured the partial and total widths of the Z to unprecedented accuracy:

$$\Gamma(Z) = 2.489 \pm 0.007 \;\; GeV \qquad \Gamma(Z \to \mu\mu) = 83.78 \pm 0.40 \;\; MeV \quad [16]$$

Using the theory predictions and LEP numbers, we extract values for the W muonic branching ratio and total W width:

$$BR(W \to \mu\nu) = \frac{\Gamma(W \to \mu\nu)}{\Gamma(W)} \qquad\qquad \Gamma(W)$$

The branching ratio and width can be expressed as well-defined functions of the basic electroweak parameters. Besides the fermion and higgs masses and the quark mixing angles, there are three free parameters in the electroweak model. In the most basic theoretical parameterization the parameters are: the $SU(2)_L$ and $U(1)_Y$ gauge coupling constants g_1 and g_2 (respectively), and the vacuum expectation value of the higgs field, v. In this basic parameterization, we have the manifestly $SU(2)_L \times U(1)_Y$ gauge invariant fields $\mathbf{W}_\mu$ ($SU(2)_L$) and B_μ ($U(1)_Y$). We transform these fields into the physically observable fields $W_\mu^\pm$, Z_μ and A_μ, and we have:

$$W_\mu^\pm = \frac{1}{\sqrt{2}}(W_\mu^1 \pm W_\mu^2)$$

$$Z_\mu = \cos^2\theta_W W_\mu^3 + \sin\theta_W B_\mu \qquad A_\mu = -\sin\theta_W W_\mu^3 + \cos\theta_W B_\mu$$

From the higgs field interactions with the above observable gauge fields, we can obtain the following relations between the fundamental constants:

$$M_W = \frac{1}{2} g_2 v \qquad M_Z = \frac{1}{2}\sqrt{g_2^2 + g_1^2} v$$

$$\cos\theta_W = \frac{M_W}{M_Z} = \frac{g_2}{\sqrt{g_2^2 + g_1^2}} \qquad \sin^2\theta_W = 1 - \frac{M_W^2}{M_Z^2}$$

$$e = \frac{g_1 g_2}{\sqrt{g_2^2 + g_1^2}} \qquad (e = \sqrt{4\pi\alpha})$$

We are free to choose the electroweak parameters with which to express the theoretical prediction for these values. The most relevant set for our kinematic regime is the W mass (M_W), the Fermi constant (G_F) as fixed from muon decay measurements, and the electromagnetic fine structure constant (α). The partial width of the W decaying into a muon may be expressed [39] as:

$$\Gamma(W \to \mu\nu) = \frac{G_\mu M_W^3}{6\pi\sqrt{2}} \cdot [1 + \delta(M_{Top}, M_{Higgs})]$$

Through its dependence on M_W and δ, the partial width is sensitive to higher order corrections in electroweak theory where heavy fermions and the higgs exist in virtual loops in the W propagator or the vertex points. The correction term δ depends on the top quark and higgs masses and represents so-called high order oblique corrections to the W width primarily due to vertex corrections (the propagator loop corrections are absorbed mostly by the M_W term). In the standard model, with a heavy top quark and a single higgs doublet, $\delta \sim 0.35\%$ [39]. This term is potentially sensitive to new physics through high order electroweak corrections to the W width; however, reference [39] indicates these contributions to be at least as small as the standard model δ value.

The W mass dependency is much stronger than the δ dependency: M_W contributes directly in the third power to the W partial (and total) width. The W mass value, when extrapolated from other precision electroweak measurements, is highly dependent on the high order corrections to the W propagator, particularly the top quark mass. The LEP experiments measure [16] an effective electroweak mixing angle, $sin^2\hat{\theta}_W^{eff}$ which, assuming the standard model, can be extrapolated to the tree level $sin^2\theta_W$ to extract an M_W value, with dependencies on the top and higgs masses.

In measuring the width, we test these dependencies; a measurement of the W width represents a test of the internal consistency of the electroweak theory in the charged current sector, in a unique kinematic range.

When comparing the total width of the W to theory, we must consider all decay modes of the W. Assuming a heavy top, the allowed decay modes are: (not including conjugate decays)

Leptonic:	$W \rightarrow \mu\nu$	$W \rightarrow e\nu$	$W \rightarrow \tau\nu$	
Hadronic:	$W \rightarrow u\bar{d}$	$W \rightarrow c\bar{s}$	$W \rightarrow u\bar{s}$	$W \rightarrow c\bar{d}$

where the last two channels are Cabibbo suppressed. CKM mixing allowed with the b-quark is neglected here. Combining all channels, we have the total width:

$$\Gamma(W) = \frac{G_\mu M_W^3}{6\pi\sqrt{2}} \cdot [1 + \delta(M_{Top}, M_{Higgs})] \cdot [3 + 6(1 + \frac{\alpha_s(M_W)}{\pi})]^{-1}$$

Comparing the cross sections and W width to standard model predictions therefore probes the consistency of the standard model in several respects, including electroweak and QCD physics.

1.3 Outline of Paper

This thesis describes in detail all necessary components for measuring the W and Z cross sections in the muon decay channel and the ratio of those cross sections. Chapter 2 gives an overview of the experimental apparatus, both the collider and the detector. The description emphasizes those systems relating to the present analysis, particularly the muon identification and trigger systems.

Chapter 3 describes the experimental procedure of measuring the cross sections, defining terms and parameters. This chapter explains how W and Z decays are identified in the detector, while motivating and detailing all identification selections. Resulting $W \rightarrow \mu\nu$ and $Z \rightarrow \mu\mu$ candidate event counts are given in this chapter.

Chapters 4 through 7 relate the corrections to the W and Z candidate event counts from chapter 3 which are necessary to extract the cross sections. In chapters 4 and 5 we compute the geometric/kinematic acceptance and selection efficiency corrections. Chapter

6 estimates the backgrounds in the final W and Z samples. The measurement of the integrated luminosity is reviewed in chapter 7.

The results from all the chapters are finally pulled together in chapter 8, yielding a measurement of the cross sections and their ratio. In chapter 8 we extract the branching ratio $BR(W \rightarrow \mu\nu)$ and the total W width, $\Gamma(W)$, from the ratio of cross sections. For each measurement and extracted value, we compare to the theoretical prediction and previous experimental values.

Chapter 2

Description of the Experimental Apparatus

The data acquisition for the analysis described herein took place from June 1992 to May 1993 at the Fermi National Accelerator Laboratory, located near Batavia, Illinois. The experimental apparatus consists of two major, separate portions: The Tevatron synchrotron provides the 1.8 TeV center of mass energy proton-antiproton colliding beams; The Collider Detector at Fermilab (CDF) detects the results of those $p\bar{p}$ collisions. In this chapter, we briefly describe the Tevatron and associated accelerators.

Separately we describe CDF with particular attention to the detector components pertinent to this analysis. Since we measure the W and Z cross sections in the muon decay channel, we emphasize the detector and trigger components relating to muon identification.

2.1 The Tevatron at Fermilab

Figure 2.1 shows a schematic view of the Tevatron and its associated accelerators. To reach the full energy of $\sqrt{s} = 1.8\ TeV$, the proton and antiproton beams are accelerated in several stages (see reference [17] for a description of the Tevatron and associated accelerator components). In the beginning, hydrogen atoms are ionized with one extra electron so that they can be accelerated to an energy of 750 keV in a Cockroft-Walton apparatus at the base of the Linac (see figure 2.1, Cockroft-Walton not indicated on diagram).

The charged hydrogen ions are then passed through the 150 *meter* long linear accelerator (Linac) to attain an energy of 400 MeV. After exiting the Linac, the ions are stripped of their electrons by a carbon foil, resulting in a proton beam that is passed to the Booster synchrotron ring (indicated in figure 2.1). The Booster boosts the protons to an energy of 8 GeV. Via pulsed operation, the Booster organizes the proton beam into discrete bunches for injection into the Main Ring.

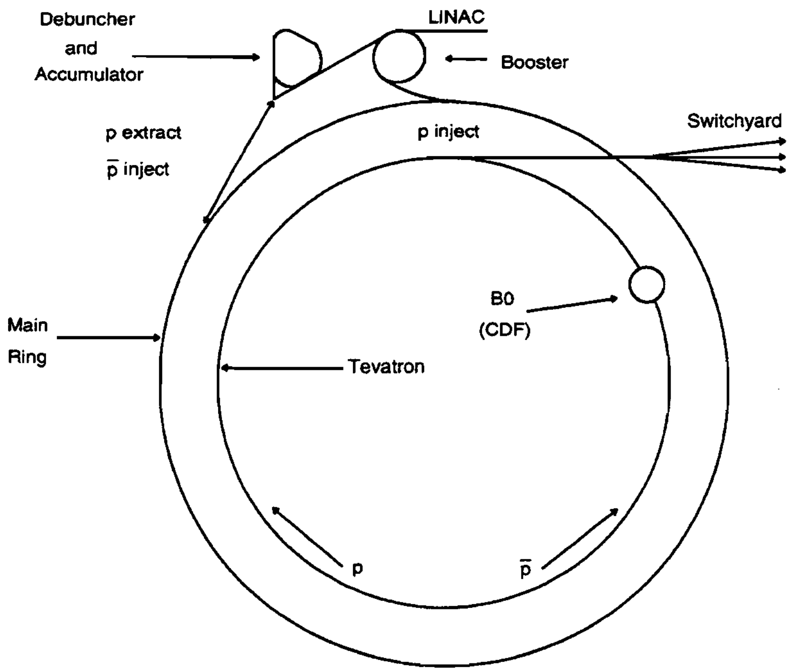

Figure 2.1: Diagram of the Tevatron and associated Accelerators

The Main Ring and Tevatron are located in the same 1 km radius circular tunnel (they are indicated separately in figure 2.1). The Main Ring synchrotron accelerates the bunches of protons up to 150 GeV. The Main Ring also provides a 120 GeV proton beam which can be extracted from the Main Ring and onto a target to produce antiprotons. The resulting antiprotons are debunched and stored in the Accumulator ring (figure 2.1) for later injection back into the Main Ring.

The final stage of acceleration is provided by the superconducting magnets of the Tevatron synchrotron. Protons and antiprotons are injected separately by bunch from the Main Ring into the Tevatron. Both occupy the same beam pipe, but circulate in opposite directions ($\bar{p}$ counter clockwise, p clockwise). The protons and antiprotons reach a laboratory frame energy of 900 GeV and collide at the B0 and D0 interaction regions at a center of mass energy of 1800 GeV. The CDF detector is located at the B0 interaction region, indicated on figure 2.1 (the D0 point is not shown). The extraction beams indicated by the Switchyard on the same figure refer to possible fixed target operation (not considered in this analysis).

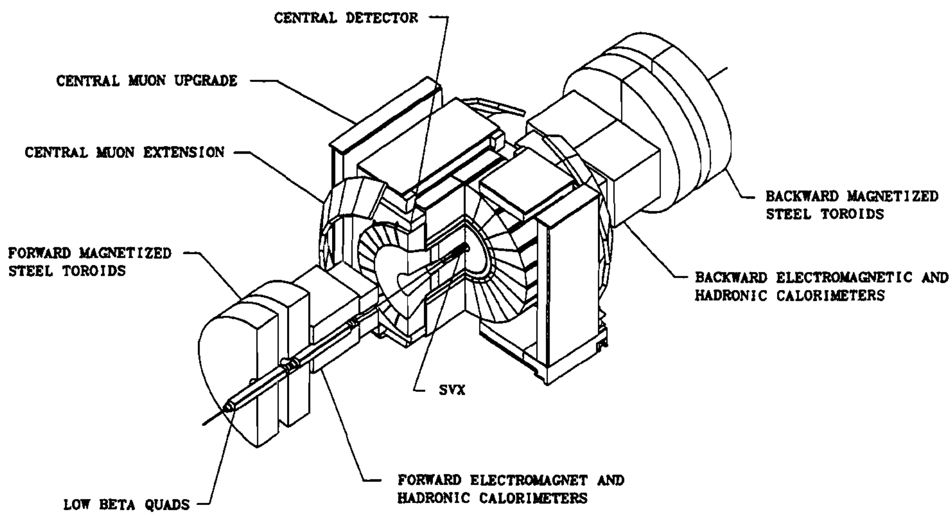

Figure 2.2: Isometric View the CDF Detector

2.2 Overview of the CDF Detector

The CDF detector is a general purpose detector designed to detect the results of 1.8 *TeV* $p\bar{p}$ collisions. CDF has been described extensively in many publications and is summarized in reference [18]. The detector envelopes the beam pipe as indicated in the isometric view in figure 2.2. The detector is cylindrically symmetric, taking advantage of the cylindrical symmetry of the colliding beams.

Figure 2.3 displays a longitudinal slice of the CDF detector [19]. Only the upper east quadrant of the detector is shown; schematically the other quadrants are very similar but not identical. Shown in this figure are the detector (x, y, z) axes and the detector (θ, ϕ) angles. The origin is defined to be the center of the detector which is very close to the $p\bar{p}$ interaction region indicated on this figure. We define the azimuthal angle (ϕ) as the angle around the beam line; the polar angle (θ) is defined as the angle relative to the proton direction. A convenient alternate coördinate is pseudorapidity, defined as:

$$\eta = -\ln(\tan\frac{\theta}{2})$$

Many detector components are segmented in projective towers in the (η, ϕ) plane, in particular the the calorimeter components.

The emphasis of CDF is to detect collision products that are preferentially in the transverse plane. Such products tend to be from hard scattering or highly inelastic processes (for example, heavy boson and heavy quark production). We wish to generally deselect the elastic and soft inelastic $p\bar{p}$ processes that tend to produce most of their collision products in the forward region. In this regard the central region of the detector is the best instrumented, with extensive tracking chambers and high resolution calorimeters.

From figure 2.3, nearest the interaction point is the Silicon Microvertex Detector (SVX) [36]. The SVX is designed to track particles very near the interaction point and distinguish sequential decay vertices on the tens of microns level. For example, the SVX can tag B meson decays where the B is produced from the primary interaction and then travels a distance before decaying. In the following analysis, this device is used to improve tracking resolution via precise determination of the beam interaction position.

Further out from the beam pipe is the Vertex Chamber (VTX). The VTX is designed measure tracks with high resolution in (z, r) coördinates. The reconstructed tracks can then be used to determine the z position of the original $p\bar{p}$ interaction point for an individual event. The Tevatron provides a spread in the interaction points of typically $\sigma_z \sim 30\ cm$.

Further out from the VTX is the Central Tracking Chamber (CTC). The CTC is a multi-wire drift chamber with a total of 6152 sense wires. The CTC is designed to produce excellent resolution for the transverse momentum measurement for charged tracks. (See figure 2.6 and the following sections.) On the outer edge of the CTC are a collection of single wire Drift Tubes (CDT) ; these are not used in this analysis.

Completely enclosing the central tracking chambers is a solenoidal magnet. The solenoid operates at a current providing a 14 kG axial magnetic field. This magnetic field is essential to the transverse momentum measurement by the CTC – the CTC hit patterns are used to measure a charged track's radius of curvature in the transverse plane.

Beyond the tracking chambers are the calorimeters. The calorimetry is instrumented out to $\eta \sim 4.2$ with several distinct components. In all cases, the calorimeters are divided into two compartments, electromagnetic (closer to the interaction point) and hadronic (further out from the interaction point). In the central region $\eta \leq 1.1$, we have the the Central Electromagnetic (CEM), Central Hadronic (CHA) and Central Wall Hadronic (WHA) calorimeters. The central calorimeters are scintillator based with either lead (CEM) or steel (CHA,WHA) as absorber.

The endcap region is covered by the End Plug Electromagnetic (PEM) and End

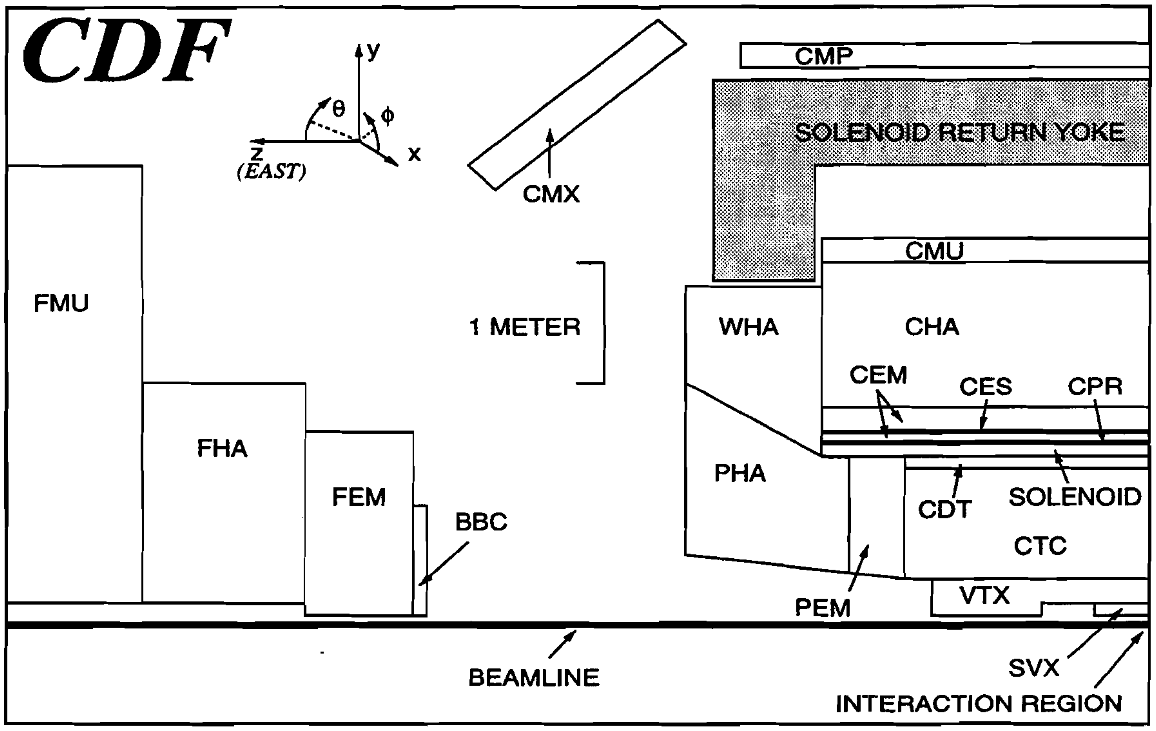

Figure 2.3: Longitudinal Profile of the CDF Detector

Plug Hadronic (PHA) calorimeters. The far forward and backward regions are covered by the Forward Electromagnetic (FEM) and Forward Hadron (FHA) calorimeters. Both the plug and forward components are gas (argon/ethane) based using staggered proportional tubes separated by lead or iron absorbers.

Beyond the central calorimeters are the muon chambers. The inner chambers, closest to the interaction point, are the Central Muon chambers (CMU). The outer layer of chambers are the Central Muon Upgrade chambers (CMP) (termed upgrade because they were newly installed for the 1992 data run). Also shown are the Central Muon Extension chambers (CMX) at higher η. At very high η behind the forward calorimeters are the Forward Muon chambers (FMU). (The CMX and FMU chambers were not used in this analysis due to operational problems.) The CMU and CMP components consist of four layers of single wire drift chambers operated in limited streamer mode.

The final component used in the following analysis is the low angle Beam-Beam Counters (BBC), which are several planes of scintillators arranged very close to the beam line. The BBC provides the luminosity measurement as well as a minimum bias trigger.

2.3 Muon Chambers

The muon chambers are divided into several components, each covering a different section of pseudorapidity. In figure 2.3 the muon chambers are indicated by mnemonics as: Central Muon (CMU), Central Muon Upgrade (CMP), Central Muon Extension (CMX), and Forward Muon (FMU). Table 2.1 lists the η range and radial position of the chambers relative to the beam line. The radial position of the CMP chambers varies significantly due to its rectangular geometry. Note that the CDF muon chamber coverage is not hermetic. There are gaps in the η coverage, and also in ϕ (not listed in table). Table 2.1 lists all the CDF tracking systems, with angular coverage, radial position and approximate single track resolution. For the muon chambers, the track resolution is measured in the transverse plane only.

The two sets of muon chambers located in the central barrel region are CMU and CMP; these are the chambers that are used in primary muon identification in the following analysis. Both CMU and CMP cover approximately the same range in (η, ϕ) space out to $\eta \sim 0.6$, as indicated in figure 4.1. The CMP chambers were added just before the 1992 data run. In general, the CMP chambers are used as confirmation for muon track stubs in the CMU chambers, both in the online trigger and the offline analysis. (See the section on triggering below and the event selection chapter for more details.) The addition of the CMP and its associated additional layer of steel was crucial in keeping the false trigger rate due to pion punch-through down to a manageable level at high beam luminosities.

The CMU chambers [22] are divided into 24 wedges ($\Delta\phi = 15°$ sections) forming an approximate cylinder around the beamline. The CMU chambers are divided at $\theta = 90°$ into east and west halves. Each CMU wedge contains a total of 48 drift chambers arranged axially along the z direction, 2.3 *meters* long. Figure 2.5 shows the positioning of a CMU wedge in ϕ (left) and the longitudinal extent of the west half (right). This figure indicates the layout of a single 15° CMU wedge; note there are significant cracks in acceptance between the wedges. The diagram in figure 2.4 shows a cross sectional view of a 5° section of the CMU [22], with a prototypical muon track passing through the four layers of drift cells.

The individual drift cells shown in figure 2.4 measure 63.5 mm $\times$ 26.8 mm in cross section, with a high voltage sense wire in the center and operating in an argon/ethane gas

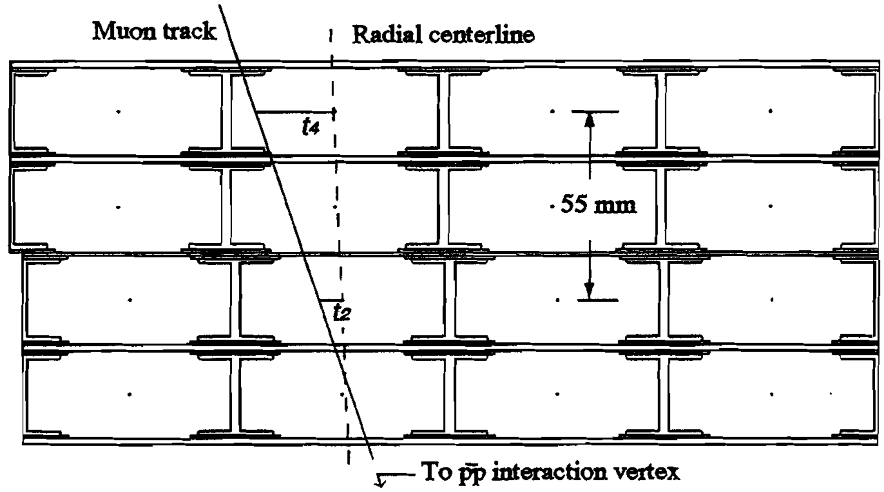

Figure 2.4: Central Muon Drift Chambers, Sectional View

mixture. A muon track stub is formed by measuring the drift time for each of the four wires along the muon path. The left-right ambiguity of the track is resolved by staggering the wires along the radial line. The chambers were operated in limited streamer mode, allowing a measurement of the z position by measuring the relative charge deposited at both ends of the sense wire (the method is called charge division, described in detail in reference [22], but not used in this analysis).

The CMP chambers are mounted on four flat planes around the central barrel detector, with about three extra absorption layers of steel beyond the CMU. On the north and south sides of the detector (see figure 2.2) the chambers planes are attached to specially built walls of steel. On the top and bottom of the detector, the chamber planes are attached to the steel of the solenoid field return yoke. The individual CMP chamber drift cells are the same cross sectional size as the CMU and are arranged along the z axis. The chambers are 320 cm long and are continuous across the CMU $\theta = 90°$ crack (no east-west division).

The CMP drift cells are half cell staggered and use the same argon/ethane gas mixture. Like the CMU, there are four layers of drift cells, and muon track stubs can be reconstructed in transverse plane by measuring the drift times in the four layers. However, the charge deposited on the wires is not measured, and so no z information on the muon track is available from the CMP.

The CMX chambers extend the coverage of the central muon system to about $\eta \sim 1.0$. The CMX drift chambers occupy the surface of a cone, as indicated in figure 2.2.

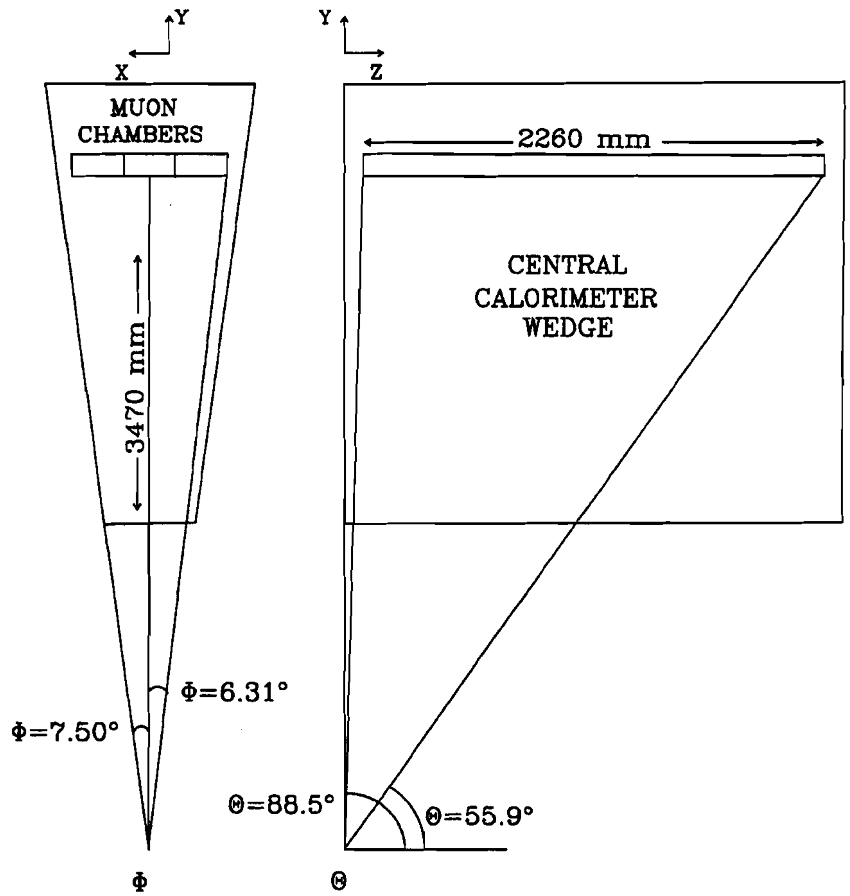

Figure 2.5: Central Muon Chambers, 15° Wedge (left) and Longitudinal Extent (right)

The chambers are free standing, just beyond the central barrel region. The CMX chambers are angled in order to point back at the interaction region. Due to the conical geometry, the CMX drift cells are tapered towards the higher η region. Muon track stubs can be reconstructed as in the CMU or CMP; the tapered chambers allow a measurement of the z position by using the stereo views of the chamber wires. (No charge measurements are made in the CMX.) Due to debris from secondary beam interactions, the inclusive single muon trigger rate from the CMX component was excessive for most of the run and so was not included in normal data acquisition. Therefore, the CMX chambers are not useful for the following analysis.

The FMU chambers occupy the far forward region of the detector, behind the forward calorimeter. The FMU chambers are designed for radial symmetry and are disk shaped, with individual cells pie shaped. At these low polar angles, the single muon trigger rate for the FMU is several orders of magnitude higher than the central muon trigger rate,

Tracker	Geometric Angular Range	Radial Position	Typical Resolution
SVX	$0.14 < \|\eta\| < 1.9$	$3\ cm < r < 8\ cm$	$26\ \mu m$
VTX	$8^\circ < \theta < 172^\circ$	$7\ cm < r < 50\ cm$	$350\ \mu m/ \sin\theta$
CTC	$40^\circ < \theta < 140^\circ$	$55\ cm < r < 276\ cm$	$220\ \mu m$
CMU	$0.03 < \|\eta\| < 0.63$	$347\ cm < r < 358\ cm$	$250\ \mu m$
CMP	$0.00 < \|\eta\| < 0.55$	$470\ cm < r < 550\ cm$	$300\ \mu m$
CMX	$0.65 < \|\eta\| < 1.00$	$440\ cm < r < 520\ cm$	$250\ \mu m$
FMU	$2.40 < \|\eta\| < 4.20$	$1.0\ m < r < 7.6\ m$	—

Table 2.1: Tracking and Muon Chambers, Coverage and Resolution

and so the FMU single muon trigger is real-time rate-limited. We expect muons from W and Z decays to be preferentially central, so we do not lose significant acceptance by not using the FMU in this analysis.

2.4 Tracking Systems

The thousands of sense and field shaping wires of the Central Tracking Chamber (CTC) [20] are arranged into wire supercells containing 12 or 6 sense wires, tilted at an angle to the detector radius. These cells are in turn arranged into 9 superlayers. The cell arrangement is shown in figure 2.6, where each thin box represents a wire supercell (short boxes have 6 sense wires, stereo superlayers; long boxes have 12 sense wires, axial superlayers). The superlayers alternate in stereo and axial configurations. The axial superlayers have their wires arranged parallel to the z axis. The stereo layers are tilted slightly with respect the z axis, in order to obtain z information about the track passing the chamber. No other information on the z position is available from the CTC.

The CTC is the only device in the central barrel region of the detector that is capable of measuring the transverse momentum of charged particles. Using the hit timing information from the CTC alone, a curvature resolution of up to $\delta P_T/P_T = 0.0011 \cdot \delta P_T$ can be achieved.

The vertexing chamber (VTX) [21] is designed primarily to determine the event vertex position in the longitudinal (z) direction. The VTX consists of many vertical planes of drift chambers along the z direction, with each individual z slice radially divided into

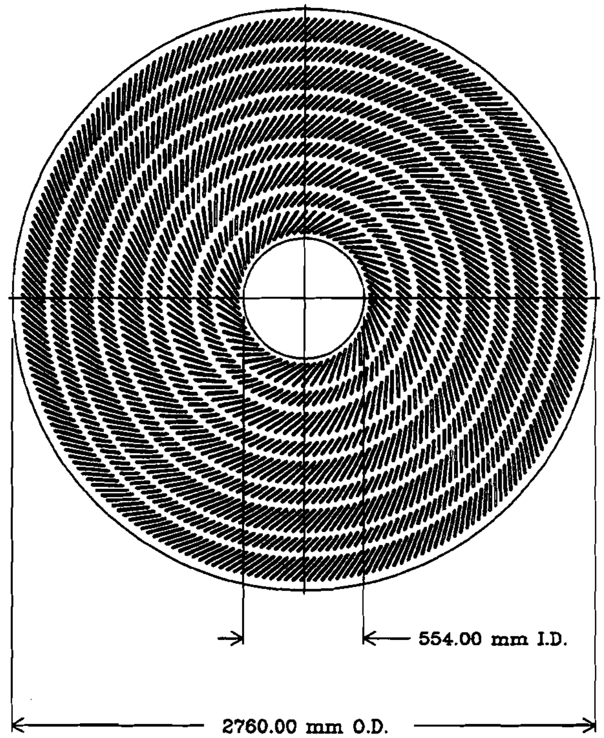

Figure 2.6: Central Tracking Chamber, Endplate View

octants. Individual chamber octants have sense wires arranged tangentially to the beam, providing track hit information mainly in (r, z) coördinates. The typical resolution for the VTX to find an event vertex is about $\delta \sim 1$ mm.

The SVX silicon microvertex detector [36] sits very close to the beam line and provides high resolution tracking near the interaction point. The SVX is a silicon based tracking chamber divided into two sections, east and west. Within each half, the longitudinal silicon strips provide tracking in the transverse plane, with four layers of strips in the radial direction, with many readout pads on each layer. The primary intended function of the SVX is to find displaced decay vertices in the transverse direction, where the displacement is on the order of hundreds of microns – for example, from B decays. The impact parameter resolution of the SVX can be as fine as ~ 11 μm. As previously mentioned, the SVX is used in this analysis to determine the average run beam position in the (x, y) direction.

Calorimeter Component	Geometric Coverage η Range	Energy Resolution	Absorption Thickness
CEM	$0.0 < \|\eta\| < 1.1$	$13.5\%/\sqrt{E} \oplus 2\%$	18 X_0
PEM	$1.2 < \|\eta\| < 2.4$	$28\%/\sqrt{E} \oplus 2\%$	18-21 X_0
FEM	$2.4 < \|\eta\| < 4.2$	$25\%/\sqrt{E} \oplus 2\%$	18 X_0
CHA	$0.0 < \|\eta\| < 0.8$	$33\%/\sqrt{E} \oplus 4\%$	4.7 Λ_{abs}
WHA	$0.8 < \|\eta\| < 1.3$	$75\%/\sqrt{E} \oplus 4\%$	4.5 Λ_{abs}
PHA	$1.3 < \|\eta\| < 2.4$	$90\%/\sqrt{E} \oplus 4\%$	5.7 Λ_{abs}
FHA	$2.4 < \|\eta\| < 4.2$	$130\%/\sqrt{E} \oplus 4\%$	7.7 Λ_{abs}

Table 2.2: Calorimeter Components, Coverage and Resolution

2.5 Calorimeters

An overview of the different calorimeter components is given in table 2.2. The mnemonics correspond to those defined in the overview section and indicated in figure 2.3. The eta ranges are approximate; there are some overlapping regions near the edges of the components which are removed by fiducial response requirements. The energy resolutions consist of the two terms listed in the table, added in quadrature. The first term is energy dependent and the second is a constant term. The absorption thickness column is in terms of radiation lengths for the electromagnetic sections (X_0) or pion absorption lengths for the hadronic sections (Λ_{abs}).

The central electromagnetic calorimeter (CEM) [25] consists of alternating layers of polystyrene scintillator and lead absorber. The CEM is segmented into towers by $\Delta\phi = 15°$ azimuthal wedges and $\Delta\eta = 0.11$ pseudorapidity slices. The scintillator from each tower is read out via two phototubes and the tower energy is scaled from the geometric sum of the signal from both tubes. Located approximately at the electron shower maximum position inside the CEM are arrays of gas strip chambers (CES). The CES tubes allow a precise measurement of the electromagnetic shower profile in the plane perpendicular to the electron's path; the CES information can be used to distinguish between electron and hadronic showers. The position resolution of the CES tubes is $\delta x \sim \pm 2\ mm$.

The central hadronic calorimeter (CHA) [26] is located behind the CEM and is identical in (η, ϕ) segmentation out to $\eta \sim 0.8$. The CHA scintillator is sandwiched between iron absorber layers; the CHA is substantially thicker than the CEM: about 4.7 pion absorption lengths. The CHA scintillators are again read out by a pair of phototubes. No drift tubes are present in the CHA.

The wall hadronic calorimeter (WHA) [26] is designed to complete the pseudorapidity coverage of the CEM where the CHA left off. The WHA is located outside the barrel endwall of the detector shown in figure 2.3. The WHA employs the same iron, scintillator sandwich at a similar thickness of 4.5 pion absorption lengths. The WHA pseudorapidity coverage extends from 0.8 to 1.3.

The plug electromagnetic calorimeter (PEM) [27] is an annular shaped detector covering the end of the central tracking chamber, covering polar angles from $\sim 32°$ down to $\sim 10°$. The PEM is a gas based calorimeter using conductive plastic proportional tube arrays arranged with lead absorber panels and read out by cathode pads. (All of the gas based calorimeters at CDF use a mixture of argon and ethane gases.) The 7×7 *mm* tubes are arranged in several depths layers, enabling shower profiles with resolution of 2 *mm*. The tower segmentation in the endplug region is $\Delta\eta \sim 0.9$ and $\Delta\phi \sim 5°$, finer than that in the central region.

The plug hadronic calorimeter (PHA) [28] is situated behind the PEM, forming a partial conical shape. The PHA uses steel plates as absorber, with similar conductive plastic proportional tubes. The PEM projective geometry and segmentation is preserved, but with an additional thickness of 5.7 pion absorption lengths.

The forward electromagnetic calorimeter (FEM) [29] is located behind the beam-beam counters (see figure 2.3) on both sides of the detector. The FEM employs a gas/lead based design very similar to the PEM, with conductive proportional tubes and tower segmentation $\Delta\phi \sim 5°$ and $\Delta\eta \sim 0.1$. The coverage extends from 2.2 to 4.2 in pseudorapidity. The FEM shower resolution ranges from 1 *mm* to 4 *mm*, depending on location.

The forward hadronic calorimeter (FHA) [30] completes the coverage in the far forward region with an additional 7.7 pion absorption lengths behind the FEM. Again, the FHA preserves the tower geometry of the FEM.

2.6 Hardware Trigger

One of the most difficult aspects of proton-antiproton collider physics is the enormous total cross section for $p\bar{p}$ interactions:

$$\sigma_{p\bar{p}}^{total} = 80.6 \pm 2.3\ mb\ [71]$$

Almost all of the $p\bar{p}$ collisions are elastic small angle scattering. The more interesting physical processes, such as the Z and W cross sections measured in this analysis are in the $\sim 0.2 - 2\ nb$ range. Other rare processes, such as top quark or diboson production are measured in picobarns. These rare processes are buried ten orders of magnitude under the total $p\bar{p}$ cross section.

With a beam crossing time of 3.5 μsec and an expected event rate of at least one inelastic interaction per crossing, digitizing and storing of every single interaction is physically impossible. Therefore, a sophisticated multi-level trigger system is needed in order to extract interesting physics measurements from the detector while minimizing dead time. The CDF trigger system is designed in three levels. Each level makes a successively more sophisticated decision, based on more and more information while taking more and more time to make the decision. The trigger system is highly flexible and programmable in several respects. Thresholds are tuned at each level to minimize dead time incurred by decision and digitization times. In the end, the trigger must reduce the event rate from 286 kHz down to a tape writing limited speed of about 6 Hz.

2.6.1 Level 1

The Level 1 trigger decision occurs entirely between successive 3.5 μsec beam crossing times, and as such causes no dead time to the system. The Level 1 trigger system consists of three main components:

1. Coincidence Hits in the East and West Beam-Beam Counters
2. Single Calorimeter Towers Over Transverse Energy Threshold
3. Muon Chamber Track Stubs Over Transverse Momentum Threshold

A coincidence in at least one of the BBC scintillators on both sides of the detector forms the so-called minimum bias trigger. This trigger also forms our primary luminosity monitor, as described further in the chapter on luminosity. The BBC scintillators are located at a small angle in front of the forward calorimeters. The spectator quarks from inelastic collisions will produce substantial debris in this low angle region and cause this trigger to fire. This trigger does not produce a Level 1 accept by itself, but for the first half of the data run, all of the calorimeter and muon type triggers were required to be in coincidence with the BBC hits. This requirement reduces the detector noise rate from level 1 (false phototube firings or cosmic rays, for example, are not usually in coincidence with $p\bar{p}$ collisions). However, the BBC coincidence becomes less useful as a trigger requirement as the instantaneous luminosity rises. For the second half of the run, when the instantaneous luminosity was consistently high and starting to saturate the BBC trigger, the BBC coincidence with the other triggers was removed. A real-time rate-limited set of events were allowed to pass through that required only the BBC trigger – these events forms the minimum bias data set (roughly one BBC trigger event was allowed every 4 seconds.)

The Level 1 calorimeter trigger is produced from the analog signals coming from either the central scintillator phototubes or the gas calorimeter cathode pads. The trigger is segmented in detector (η, ϕ) plane by $\Delta\phi = 15°$ and $\Delta\eta = 0.2$. The actual segmentation provided by the calorimeters is reduced by fast analog signal summing in order to reduce the large quantity of signals to a manageable level, resulting in a total of 2048 trigger towers, half electromagnetic and half hadronic. The EM and hadron towers are triggered separately. The analog calorimeter signals are corrected for pedestal offsets and gain variations.

The trigger tower segments are also weighted by $\sin\theta$, where θ is the detector polar angle, so we are able to set the trigger threshold based on the transverse energy in the tower: $E_T = E\sin\theta$. No correction is made for possible event variations in the z vertex position. Thresholds are applied separately by six sectors: (Central, Endplug, Forward) $\times$ (Electromagnetic , Hadronic). The central electromagnetic region has the lowest threshold $\sim 6\ GeV$, while the forward hadronic region has a very high threshold $\sim 25 - 51\ GeV$. In the central electromagnetic section, a simple two towers over a lower threshold can also be implemented. This analysis does not use the calorimeter trigger at Level 1.

The Level 1 muon trigger can best be explained by examining one of the 5° CMU chamber sections in figure 2.4 (see also reference [34]). If there were no solenoidal magnetic field, a muon would follow a radial path (projected in the transverse plane) from the interaction point out to the muon chambers (neglecting multiple scattering). The dotted line in the figure indicates this radial path at the point of the muon chambers. However, in the presence of an axial magnetic field, the muon's path bends as it traverses the interior of the solenoid. After exiting the solenoid, the muon resumes a straight track for the remainder of the path out to the CMU chambers. At the CMU chambers, the muon track has a dip angle with respect to the radial line, as indicated by the muon track in figure 2.4. The value of the dip angle is a function of the amount of curvature experienced by the muon inside the solenoid, which is a function of the transverse momentum P_T of the muon.

The muon trigger makes a fast analog measurement of the times t_4 and t_2 indicated in the figure. The difference in times, $\Delta t = t_4 - t_2$, can be used to approximate an inverse function of the muon P_T. The trigger cuts on some maximum Δt, which corresponds to a minimum cut on the P_T. Of course, the Δt measurement is smeared by multiple scattering and the resolution of the time measurement.

The trigger circuitry operates separately on each pair of wires separated by one layer in figure 2.4. The 5° CMU tower fires the trigger if any one of the wire pairs satisfies the Δt cut. The single muon trigger cuts on a drift time difference of $\Delta t \leq 40\ ns$. This requirement makes an effective cut of $P_T \geq 6\ GeV$, where 6 GeV is the 90% efficiency point for the trigger. A dimuon trigger can be implemented that requires at least two 5° CMU towers to have fired the trigger, generally at a lower single threshold of $P_T \geq 3\ GeV$.

The Level 1 trigger for the CMP chambers requires a simple hit coincidence between chambers in alternate layers. Triggers passing *only* the CMP Level 1 trigger are not accepted; instead, the CMP trigger is used as confirmation of the CMU trigger. In this way, we expect to reduce the background pion punch-through trigger rate, since the CMP chambers have 3 extra pion absorption lengths between them and the CMU. The CMP chambers cover a significant subset of the CMU (η, ϕ) plane. In those 5° CMU towers that are covered by CMP chambers, a CMP trigger confirmation is required; see figure 4.1 for a map of which CMU towers are covered by the CMP.

The raw trigger hits for each CMP trigger section are mapped back onto the projected CMU 5° towers. A matching window of at least 10° is allowed in the projection. For the 50 5° CMU towers that are covered by the CMP, a coincidence is required to the projected CMP trigger region before the single muon trigger will fire for that CMU tower. The combined Level 1 CMU and CMP inclusive muon trigger rates typically ranged from 300 to 500 Hz in real-time, or about 100 μb in cross section.

2.6.2 Level 2

After the receipt of a Level 1 accept, the beam crossing clock is inhibited from clearing the detector signals. All detector signal gates are held while the Level 2 trigger makes its decision in about $\sim 20\ \mu sec$, thus incurring some amount of dead time while processing. With the added processing time, a much more sophisticated decision can be reached at Level 2. The added information at Level 2 consists of five main items:

1. Fast CTC Track Pattern Recognition (CFT)
2. Hadronic and Electromagnetic Calorimeter Clustering
3. Matching CFT Tracks to Muon Hits
4. Matching CFT Tracks to Calorimeter Clusters
5. Global Energy Sums (Total, Transverse, Missing Transverse)

The Central Fast Tracker (CFT) is described in reference [35]. The CFT makes use of fast hit information from the five axial superlayers. As a charged track passes through the CTC it will deposit charge on nearby sense wires. The drift time can be measured relative to the beam crossing time for each individual CTC sense wire; this time is proportional to the distance of the track to the wire. For each wire, two separate gates are used to clock hits into the CFT latches: prompt and delayed. The prompt hit coincidence gate allows hits up to 80 ns after the beam crossing time, producing at least one hit per wire supercell. The delayed gate occurs about 600 ns following the beam crossing time (width of 80 ns), allowing at least two delayed hits per wire cell.

The resulting prompt and delayed hit patterns can then be used to identify tracks curving in the solenoidal field. By clocking the hit patterns through a pattern recognition look-up tables, the transverse momentum of individual tracks can be measured with a resolution of $\delta P_T/P_T^2 \sim 3.5\%$. The CFT look-up process generates a list of tracks in eight P_T bins with nominal central values of: $3.3, 4.0, 5.0, 6.5, 10.0, 15.0, 20.0, 30.0\ GeV$ The 90% efficiency points of the same P_T bins are $3.0, 3.7, 4.8, 6.0, 9.2, 13.0, 16.7, 25.0\ GeV$. This list of tracks is then past to the rest of the trigger system and can be used to match with muon hits and calorimeter clusters. Note that the CFT uses only hits from the axial superlayers, and so each track has only the measured P_T and azimuthal position, ϕ.

The raw Level 1 trigger rate of $\sim 400Hz$ coming from the CMU and CMP triggers vastly exceeds the capability of the data acquisition to digitize all detectors signals without incurring substantial deadtime. To reduce the inclusive muon trigger rate, a match between a CFT track and a Level 1 Muon trigger hit is required at Level 2. All matching is performed in the transverse plane; each individual CFT track is projected in a straight line out to the muon chambers using the nominal central P_T value of the track. A match is declared if that track matches within a certain $\Delta\phi$ window. For the first half of the data run, this window was $\Delta\phi \sim 15^\circ$, corresponding to the size of a single CMU wedge. During the second half of the run, the window was tightened to $\Delta\phi \sim 5^\circ - 10^\circ$ in order to further reduce the trigger rate due to spurious (non-muon) signals.

The raw Level 2 inclusive muon trigger cross section is then reduced to typical value of $\sim 0.5\ \mu b$. All trigger cross sections tend to be rising functions of instantaneous luminosity, and numbers quoted here are order of magnitude estimates. The Central Extension chambers (CMX) provide a separate set of Level 1 trigger hits and can also be matched separately to the list of CFT tracks (not used in the following analysis).

The second major aspect of the Level 2 trigger system is the ability to perform calorimeter clustering. The 2048 analog signals from the calorimeter, segmented in (η,ϕ), can now be used to identify clusters of transverse energy in the electromagnetic or hadronic compartments. A fast algorithm is used to locate clusters: Two sets of thresholds are applied to all calorimeter trigger towers, "seed" and "shoulder". This application of thresholds results in two maps (seed and shoulder) of towers over thresholds. The maps are then scanned sequentially in (η,ϕ) space. When a trigger tower is found passing the seed threshold, a cluster is flagged. The four towers adjacent in the (η,ϕ) plane are then checked to see if they pass either the seed or shoulder thresholds; if a tower does pass it is added to the cluster. All adjacent towers to this newly included tower are also checked and are included in the cluster if they pass threshold. The sequence is repeated for each subsequent tower over threshold until all adjacencies are exhausted.

When all towers in a cluster are identified, the cluster is digitized with associated values of $E_x, E_y, E_T, \eta, \phi$, *etc.*. Appropriate analog and digital weighting is performed for the $\sin\theta$,$\sin\phi$ and $\cos\phi$ factors, on a tower by tower basis. Note that a tower is never allowed to be a member of more than one cluster. More than one clustering pass can be applied at Level 2, allowing separate jet clustering (Hadronic and Electromagnetic combined) and electron/photon clustering (electromagnetic only). The clusters can also be matched to the CFT track list, in the $\Delta\phi \sim 15^\circ$ trigger tower segmentation. Cuts can then be applied to the list of clusters, in many permutations of cluster identification with myriad possible combinations across detectors and cluster types. The calorimeter clustering triggers are not used in the following analysis.

Global sums of calorimeter energies are also available at Level 2. The Level 2 trigger computes the total energy sum, total transverse energy, total missing transverse energy, and total clustered energy. All information produced at Level 2 can be triggered on alone or in conjunction with any combination of other Level 2 data.

2.6.3 Level 3

Upon the receipt of a Level 2 Trigger Accept by the trigger/data acquisition system, all channels in the detector are digitized and the entire event record is shipped off to the Level 3 trigger system. Digitization typically takes $\sim 2-3\ ms$. The detector is then free to examine subsequent beam crossings for Level 1 and Level 2 triggers while the Level 3 trigger operates independently and in parallel. The Level 3 trigger [37] consists of 48 Silicon Graphics computers, each containing two event buffers, plus an array of service hardware to push the data into and out of the 96 buffers. Each event is sent to a single buffer, and so Level 3 can be processing up to 48 separate events in parallel, with another 48 events meanwhile being loaded to the secondary buffers. Most of Level 3 processing and filtering is done by programs written in the Fortran language; the allowed processing time is about 1 or 2 seconds, thus allowing potentially elaborate identification.

A special variant of offline processing is performed when the event first arrives at the Level 3 node. Tracking, vertexing, muon reconstruction, calorimeter corrections, and global event analysis all take place in Level 3; offline processing is described in detail in the following chapter. Subsequently events can be filtered based on any of the physics objects identified by the offline processing. A multitude of trigger streams, each filtering on objects such as electrons, muons, taus, dimuons, multi-jets, etc., are available at Level 3.

We describe here only the inclusive high transverse momentum muon trigger. The cuts required on the identified muon object are:

1. Transverse Momentum: $P_T \geq 18\ GeV$
2. Hadronic Energy Deposition: $E \leq 6\ GeV$
3. CMU Chamber to CTC Track Matching: $|\delta x| \leq 3\ cm$
4. CMP Chamber Hit Matching from Level 1 Trigger Hits

In the Level 3 trigger no selection is made on any global event characteristics. The hadronic energy deposition and CMU chamber track matching are defined in the following chapter; both of these cuts are loose when compared to the expected values for real muons from W or Z decays, also discussed in the next chapter. A CMP hit match is required only for those 5° CMU towers which are nominally covered by the CMP. The specified hits are taken directly from the Level 1 CMP trigger, as described above; therefore this requirement is somewhat redundant for good muon candidates, but should eliminate spurious volunteers. No other quality cuts are required in the Level 3 trigger.

The Level 3 trigger reduces the event rate to a manageable rate of about $\sim 6-8\ Hz$, which can be written to a combination of four 8 mm tape drives and disk drives. The raw data event record typically consists of 200 *kilobytes* of information.

Chapter 3

Event Selection

The following chapter describes the experimental motivation for measuring the W and Z muonic decay cross sections. We describe the experimental signature of these decays as well as the experimentally measured quantities involved in the cross section and ratio measurements. All cuts made to identify candidate events are described and their motivation explained with respect to signal identification and background rejection. A brief coda identifies the sources of non W and Z muon events in our kinematic range.

3.1 W and Z Decay Characteristics

For the production of real W and Z bosons in proton-antiproton collisions, the standard model predicts isolated, high transverse momentum decay leptons [38]. The W and Z bosons are so heavy and their widths so large ($\Gamma(W) \sim 2$ GeV, $\Gamma(Z) \sim 2.5$ GeV) that their subsequent decays can easily be considered prompt from the hard scattering interaction point. Figure 3.1 indicates the dominant quark-antiquark W and Z production processes with muonic decay. The dominant higher order processes include associated gluon jet production off one of the incoming quark lines, giving the boson a subsequent boost (as in figure 4.2).

We study leptonic decays of W and Z bosons since generic QCD dijet production swamps the hadronic decays. For this reason, we do not measure the total W and Z production cross sections, but rather the cross sections times branching ratios: $\sigma \cdot B(W \to \mu\nu)$ and $\sigma \cdot B(Z^0 \to \mu^+\mu^-)$. The analyses for electron and tau decays are substantially different and are described elsewhere [41], [42]. We describe here the identification of muonic boson decays, and the various detector parameters used and the motivation for candidate cut values.

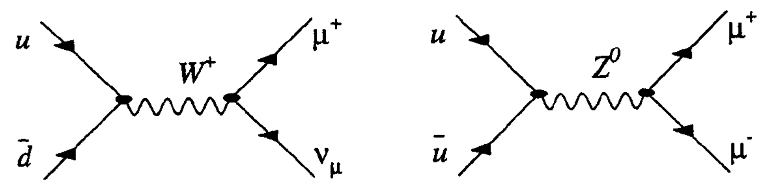

Figure 3.1: Dominant W and Z Production Processes with Muonic Decay

3.2 $W \rightarrow \mu\nu$ Identification

W muonic decays involve a high transverse momentum muon and muon-type neutrino. W candidate identification requires one high transverse momentum muon with:

$$P_T \geq 20\ GeV\ where\ P_T = \sqrt{P_x^2 + P_y^2}$$

The detector (x, y, z) coördinate axes are illustrated in figure 2.2. The plane transverse to the $p\bar{p}$ beamline is defined to contain the (x, y) components while the z direction is parallel to the beamline.

The CDF detector is capable of efficiently detecting high transverse momentum muons located in the central muon chamber region, $|\eta| < 0.6$. The signature of a muon in the detector is a track pointing first to a minimum ionizing cluster in the electromagnetic and hadronic calorimeters. Beyond the calorimeter's five absorption lengths, the muon will hit the Central Muon chambers (CMU) and leave a track stub. Beyond the CMU chambers are three additional pion absorption lengths of steel and the Central Muon Upgrade chambers (CMP) where the muon will leave an additional muon track stub, essentially as confirmation of the original CMU muon stub.

However, the CDF detector is incapable of directly detecting the neutrino. We infer the presence of a neutrino by the presence of large unbalanced transverse momentum, or missing E_T ($\not{E}_T$):

$$\not{E}_T \geq 20\ GeV\ where\ \not{\mathbf{E}}_\mathbf{T} = -\Sigma\mathbf{E}_\mathbf{T}$$

We reconstruct the event's total energy vector in the transverse plane: $\mathbf{E_T} = (E_x, E_y)$ and define ΣE_T as the magnitude of the vector sum of all energy projected in the transverse plane of the entire detector:

$$\Sigma E_T = |\mathbf{E_T}| = \sqrt{E_x^2 + E_y^2} \quad E_x = \Sigma_i E_T^i \cos\phi_i \quad E_y = \Sigma_i E_T^i \sin\phi_i$$

where the sum is over all detector towers. ΣE_T includes the muon $\mathbf{P_T}$ and the vector sum of the calorimeter energy (the operational detector definition of ΣE_T is given in the W selection section). The incoming quark system has zero initial momentum in the transverse plane, so we are able to use conservation of momentum to reconstruct the transverse momentum of the invisible neutrino. We ascribe the neutrino energy vector to oppose this sum:

$$\mathbf{E_T^\nu} = -\mathbf{E_T} \qquad E_T^\nu = \not{E}_T$$

We ascribe the missing transverse energy in the event to the neutrino. The longitudinal momentum of the incoming quark system is unknown, so we cannot reconstruct the P_z^ν of the neutrino. Therefore, we cannot reconstruct the dilepton invariant mass of the μ, ν system, which would have the value of the W mass. Instead, we construct a convenient quantity called the "transverse mass" which is the two dimensional analog of the dilepton invariant mass with the longitudinal momentum components set to zero:

$$M_T^2 = (E_T^\mu + E_T^\nu)^2 - (\mathbf{E_T^\mu} + \mathbf{E_T^\nu})^2$$

The transverse mass spectrum peaks near the actual mass of the W and quickly falls off above the W mass, but falls slowly to zero below the W mass. M_T^2 is not very sensitive to the momentum of the original W boson nor to the structure of the underlying parton event.

3.3 $Z \rightarrow \mu\mu$ Identification

Z muonic decays produce two oppositely charged muons, both of which can be completely reconstructed in our detector. Z candidate identification requires two high transverse momentum leptons with both leptons' $P_T \geq 20\ GeV$. Since the momenta of both muons is measured, we reconstruct the dimuon invariant mass and require it to be in a $\pm 25\ GeV$ window around the Z mass:

$$66 \leq M_{\mu^+\mu^-} \leq 116\ GeV$$

Relaxed identification cuts are made for the secondary Z candidate lepton, allowing secondary muons out to $|\eta| \leq 1.2$. For the secondary muon, only a minimum ionizing track is required with no requirement on muon chamber hits.

3.4 Experimental Cross Section Measurement

In terms of experimentally measured quantities, the individual cross sections can be expressed as:

$$\sigma_W = \frac{N_W - B_W}{\epsilon_W \cdot A_W \cdot \int \mathcal{L}} \qquad \sigma_Z = \frac{N_Z - B_Z}{\epsilon_Z \cdot A_Z \cdot \int \mathcal{L}}$$

Where we have:

$N_{W,Z}$	Number of W or Z Candidate Events
$B_{W,Z}$	Estimated Background to the observed W or Z Sample
$\epsilon_{W,Z}$	Selection and Trigger Efficiency, W or Z
$A_{W,Z}$	Geometric and Kinematic Acceptance
$\int \mathcal{L}$	Integrated Luminosity

Taking the ratio of cross sections, we have:

$$\frac{\sigma_W}{\sigma_Z} = \frac{N_W - B_W}{N_Z - B_Z} \cdot \frac{\epsilon_Z}{\epsilon_W} \cdot \frac{A_Z}{A_W}$$

In the ratio of cross sections, we see the common term $\int \mathcal{L}$, the integrated luminosity, completely cancels. Indeed, the luminosity represents the largest uncertainty factor in the individual cross sections. Experimentally we are motivated to measure the ratio because of this large luminosity uncertainty.

The efficiencies for individual cross sections are also poorly known. Our general plan for identification cuts is to put identical, stringent quality requirements on the primary muon in both the W and Z samples. The primary muon selection efficiencies will then cancel out in the ratio. The efficiency ratio terms will then only involve secondary muons in the Z sample, with corrections for double chances (described in detail in the chapter concerning efficiencies; note that the efficiency for neutrino identification is included in the kinematic acceptance described in a separate chapter). Also, the ratio of acceptances tends to be less sensitive to systematic effects, as will be described in the chapter on acceptances.

Real Muons	$W \rightarrow \mu + X$ $Z \rightarrow \mu + X$ $W \rightarrow \tau \rightarrow \mu + X$ $Z \rightarrow \tau \rightarrow \mu + X$ $\gamma \rightarrow \mu\mu + X$ $b \rightarrow \mu + X$ $c \rightarrow \mu + X$ $s \rightarrow \mu + X$ $t \rightarrow \mu + X$ $\pi \rightarrow \mu + X$: Decay in Flight
Fake Muons	π fakes μ : Punch Through
Non $p\bar{p}$ Real Muons	Cosmic Rays

Table 3.1: Processes Contributing to the High P_T Inclusive Muon Sample

3.5 Inclusive Muon Identification Variables

We begin the task of W and Z muon decay identification by first creating an inclusive, high P_T muon sample. The purpose of the inclusive sample is to identify events containing a high P_T muon and to distinguish real muons from objects that may cause a fake signal, for example a pion faking a muon. The inclusive sample makes no selection on any global event characteristics or on any associated signal near the muon, such as isolation. This sample represents the process $p\bar{p} \rightarrow \mu + X$ in the high P_T region, with no requirements on the intermediate production process. The inclusive sample will contain events from a variety of sources, listed in table 3.1, where all of these processes represent real muon production, except for pion punch through. Cosmic rays, of course, are produced independently of the $p\bar{p}$ collisions but are produced at times in coincidence with interaction times. The light quark decay processes are suppressed due to the high P_T cut; the top quark decays are suppressed by the low top quark production cross section [43]. We expect the dominant contribution to come from b quark decays and pion decays in flight.

The inclusive identification of a muon in the detector consists of three basic parts: (note that discussions pertain to high P_T muon selection only)

Track in the Central Tracking Chamber

\+ Track Points to Minimum Ionizing Energy Deposition in the Calorimeter

\+ CTC Track Matches to Track Stub in the Muon Chambers

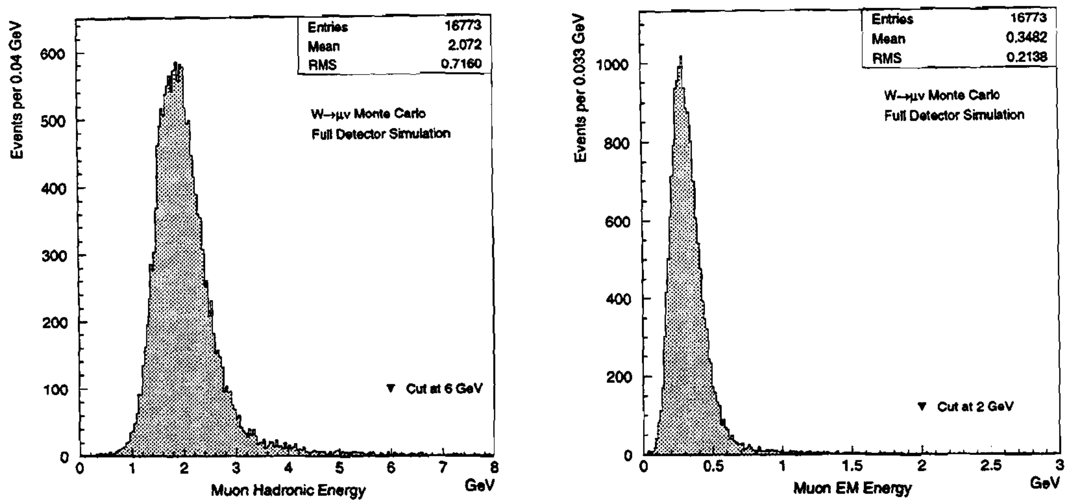

Figure 3.2: Predicted Muon Calorimeter Energy Deposition

Muons are charged particles and so necessarily leave a trail of ionization through the argon/ethane gas mixture and electric field of the central tracking drift chamber. Such ionization is detected by the chamber's sense wires. After exiting the central tracking chamber, the muons pass through the lead (EM) and iron (Hadronic) compartments of the calorimeter. Muons do not interact strongly and so deposit energy in the calorimeters based on electromagnetic interactions with the material in the calorimeter. Through test beam and cosmic ray studies described in reference [24], we expect a typical energy deposition in the EM calorimeter of $\sim 0.4\ GeV$ and $\sim 2\ GeV$ in the hadronic calorimeter. Figure 3.2 plots the expected energy deposition of a muon from IsaJet generated $W \rightarrow \mu + X$ Monte Carlo, with a full detector simulation; plotted separately are the EM (left) and hadronic (right) compartments. Note that the identification cuts are indicated on the histograms and are well within the signal regions.

The calorimeter signatures of pions and electrons are quite distinct from that of muons. The EM and hadronic calorimeters represent ~ 5 pion absorption lengths, and we expect $20\ GeV$ pions to typically deposit most of their energy spread over the two calorimeter compartments. Electrons generally deposit all of their energy in the EM calorimeter. Both electrons and pions (and other charged hadrons) induce charged tracks in the CTC but deposit a substantial fraction of their energy in the calorimeter; by making a minimum ionizing cut on the calorimeter cluster associated with the charged track, we preferentially select against electrons and pions and in favor of muons.

Since muons deposit only a small fraction of their energy in the calorimeter, they continue out beyond the calorimeter and form a track stub in the central muon (CMU) chambers. Beyond the CMU, in certain fiducial regions shown in figure 4.1, the muon continues out through ~ 3 additional pion absorption lengths of steel and forms another track stub in the central muon upgrade (CMP) chambers. For further pion rejection, the CTC track is required to geometrically project out and match to a CMU track stub (and also a CMP track stub where appropriate). With this requirement, there still exists a pion background where the pion deposits only a small fraction of its energy in the calorimeter and then exits the rear face of the calorimeter ("punches through") and forms a track stub in the muon chamber. For the fiducial CMP region the pions must traverse a total of ~ 8 absorption lengths, so punch through is extremely unlikely in this region.

The identification of high P_T muons begins by processing events that have passed the trigger. The raw event data from the tracking chambers, muon chambers and calorimeters is passed through "Production" processing, which performs several functions:

1. Reconstruct interaction vertices using the vertexing chamber information
   Producing a list of vertices, primarily from (r, z) information
2. Central Tracking Chamber pattern recognition, fitting to:
   Track transverse curvature, angles and displacement
3. Muon Chamber Track Stub Reconstruction
4. Calorimeter Corrections, Jet Clustering, Electromagnetic Clustering
   and Track Matching
5. Matching Central Tracks and Muon Chamber Stubs
   with matching to calorimeter towers and minimum ionizing energy deposition

The results of the production software make very tentative and loose identification of possible muon entities in the record of the event. The CTC track pattern recognition and reconstruction proceed independently of the muon chamber (CMU and CMP) track stub reconstruction. After the lists of all CTC tracks and all CMU/CMP stubs are made for a particular event, the two lists are matched together. This matching process yields a list

Cut, Inclusive High P_T Muon Sample	Events Remaining	Passing All But This Cut
Express High P_T Muon Data Stream	80351	—
$P_T \geq 18.0 GeV$, CMU or CMU+CMP	46653	14127
$P_T \geq 20.0 GeV$, Beam Constrained	35190	18368
Hadronic Energy $\leq 6.0\ GeV$	35190	14124
EM Energy $\leq 2.0\ GeV$	33995	18476
CMU $\lvert\delta x\rvert \leq 3.0\ cm$	21531	14884
CMP $\lvert\delta x\rvert \leq 10.0\ cm$	19671	14511
CMP Match Required	18366	16747
$\lvert z_\mu - z_{Vertex}\rvert \leq 5.0\ cm$ $\lvert z_{Vertex}\rvert \leq 60.0\ cm$	18366	16747
Passes Cosmic Ray Filter	16205	15781
Fiducial CMU Chamber Region	15644	14599
Fiducial CMP Chamber Region	15526	14228
Fiducial Run	14421	15178
Passes Level 1 Trigger	14333	14119
Passes Level 2 Trigger	14236	14215
Passes Level 3 Trigger	14119	14236
Inclusive High P_T Muons	**14119**	—

Table 3.2: Inclusive Muon Selection Cuts

of possible muon candidates, with a number of δx quantities describing how well the CTC and CMU/CMP tracks match geometrically. As well, the production process identifies the cluster of energy associated with the muon candidate in the calorimeter. We now have a list of muon candidates for each event, and an associated list of matching quality parameters and energy deposition measurements. From this list of quantities, we make cuts to reduce the previously described backgrounds. All of the inclusive muon identification quantities are listed in table 3.2, with corresponding event counts. The following section describes each parameter in detail.

3.5.1 Parameter Definitions

For each of the cut quantities listed in table 3.2, figures 3.5, 3.6, 3.7, and 3.8 display the histogram of the cut quantity, where all of the inclusive cuts have been applied except for the one being plotted.

The initial kinematic cut: $P_T \geq 18\ GeV$ is made on the fits to the central tracking chamber only. We can substantially improve the resolution by constraining the track to the beam interaction point; this cut is listed as $P_T \geq 20\ GeV$, *Beam Constrained* and forms the primary kinematic selection on the muon. The z position of the constraint is provided by the VTX chamber for each event; the x and y beam positions are provided on a run by run basis from fits to the SVX detector data.

The minimum ionizing cuts are performed on energy deposited in both the electromagnetic and hadronic sections: the electromagnetic energy must be $\leq 2\ GeV$; the hadronic energy $\leq\ 6\ GeV$. The cut is relaxed in the hadronic compartment due to its extra absorption lengths and larger expected energy deposition. The calorimeter energy cluster is identified by forming a cone of $\Delta R \leq 0.13$ around the projected position of the muon track in the calorimeter (η, ϕ) plane, where we define:

$$\Delta R = \sqrt{(\Delta\eta)^2 + (\Delta\phi)^2}$$

This cone size usually corresponds to a single calorimeter tower. See figure 3.2 for the Monte Carlo prediction of these quantities. In figure 3.2, IsaJet generates $W \rightarrow \mu\nu$ events, followed by a full detector simulation. The data cut is well within the predicted signal region. The muon traverses a total of ~ 5 pion absorption lengths in both calorimeter sections. The towers used to identify the minimum ionizing cluster are based on the extrapolation of the muon track to the (η, ϕ) calorimeter plane.

The central tracking chamber (CTC) muon track is extrapolated out to the muon chambers in order to match with the muon chamber track stub and form an inclusive muon object. We consider here only the Central Muon chambers (CMU) and the Central Muon Upgrade chambers (CMP). The distance between the extrapolated position based on the CTC track and the actual position of the muon chamber track stub is defined to be the quantity δx, where x is measured in the transverse plane along the base of the CMU chambers. This quantity deviates from zero due to several effects: CTC track smearing and momentum resolution; multiple scattering; dE/dx Energy loss between the CTC and the muon chambers; and the production of delta rays near the muon chambers. We have simulated this process in the same manner as the energy deposition and plot the result in figure 3.3; compare with the equivalent plots from the data in figure 3.7. The data distributions tend to be systematically narrower than those in the data: the effect of delta rays has only been included in the simulation in an approximate manner and pion punch through background has not been included in the simulation. (See discussion in following

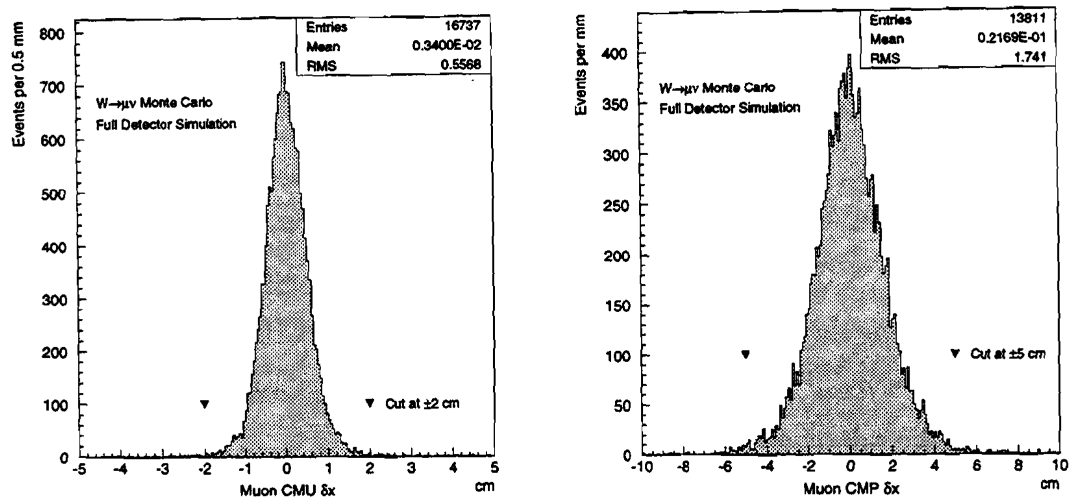

Figure 3.3: Predicted Muon Track Matching Parameter δx, CMU Chambers (left) and CMP Chambers (right)

section for comparison to pions.) (Delta rays are low energy electron-positron pairs created by very low Q^2 scattering of the muon off of metallic detector parts; if they enter the muon chambers, they will smear the digitized signal, causing the δx distribution to broaden.) We cut the data at CMU $|\delta x| \leq 3.0\ cm$ and CMP $|\delta x| \leq 10.0\ cm$. Note that the CMP δx cut is performed only when a CMP track stub is required (described under quality cuts).

The quantity z_{Vertex} is defined as the position of the event vertex as calculated from the vertex chamber tracks. The quantity z_μ is the extrapolated position of the muon track back to the beamline. We require that z_μ be within 5 cm of z_{Vertex} primarily in order to reject cosmic rays – W decays are prompt and should not create a displaced vertex. The value z_{Vertex} involves the best fit to several tracks involved in the interaction, and is better measured than z_μ and so is used in the beam constraint of the momentum described above. For the same reason, we choose to cut on z_{Vertex} to be within 60 cm of the center of the detector to restrict the interaction point to the central, fiducial region.

3.5.2 Hadronic Particle Rejection

As mentioned above, a variety of charged hadronic particles can mimic the signal of a muon in the detector by punching through the rear face of the hadronic calorimeter. We expect most of these particles to be pions. Pions are produced from a multitudinous number of different processes. Pions usually occur within jets, and so punch through probability is a function of jet composition. Jet fragmentation is notoriously difficult to model; instead we consider here single pions as fakes to muons in order to qualitatively explain the long tails in the energy deposition (figure 3.6) and track matching (figure 3.7) distributions.

We compare the expected energy deposition and track matching parameter δx in figure 3.4 between muons and pions. For this Monte Carlo study, pions and muons are generated uniformly in the kinematic range $20 < P_T < 30$ GeV and trajectory $0.0 < |\eta| < 0.8$. The resulting charged tracks are then passed through a full, very detailed detector simulation with all known effects. The muons are reconstructed as they would be in the data sample. The pions are simulated separately, but their offline quantities (energy deposition, track matching) are reconstructed as if they were muons. Effectively the pions are selected to punch through the calorimeter and form a muon track stub in the CMU muon chambers; the reconstructed pion energy cluster is the same predefined size as the muons (defined to be smaller than would be used in jet reconstruction). The relative scale is somewhat arbitrary, but reflects the approximate relative acceptance for real muons to pions faking muons (where the generated pions and muons are kinematically similar).

On the left of figure 3.4 we plot the expected electromagnetic plus hadronic energy deposition for muons and pions separately (pions here are punch through fakes only). Note that the expected energy deposition for muons is sharply peaked at about ~ 2.7 GeV. However, the pions have a slowly falling spectrum with no distinct peak. By selecting punch through pions, the pions have necessarily not deposited all of their energy in the calorimeter; as well, a significant fraction of pion energy is deposited outside the muon projected energy cluster, thus explaining the absence of a clear peak in this spectrum. The maximum allowed energy deposition for muon candidates in the data sample is shown on the plot (the actual cuts are made individually on the electromagnetic and hadronic portions – see parameter definitions above). By cutting just above the muon peak we reject a large fraction of pions.

Likewise, we plot the CMU track matching quantity δx on the right of figure 3.4 for both muons and pion fakes. Beyond the primary muon cuts of $|\delta x| < 2.0$ cm there are essentially no real muons. (primary muon cuts are described below.) The pion fakes, however, have a much longer tail in the distribution. In the real data we expect the

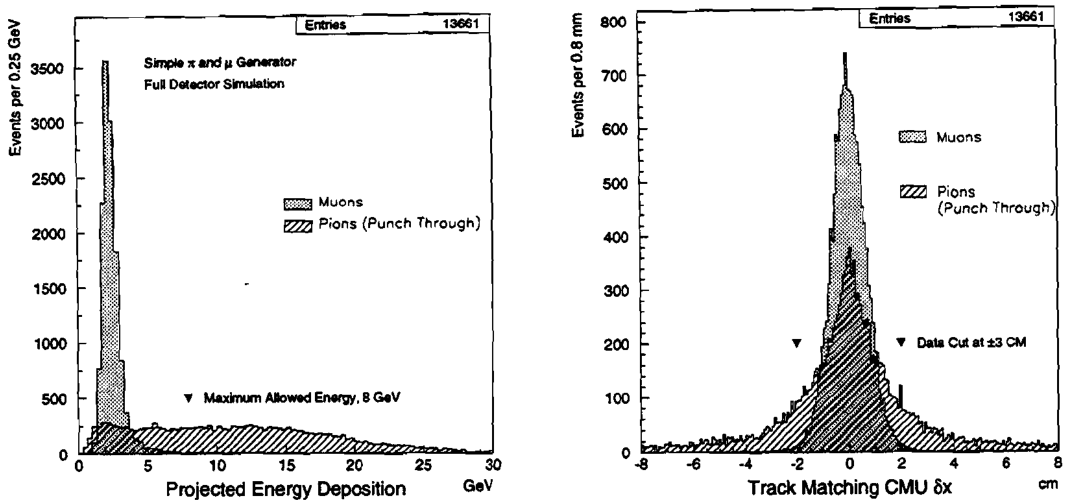

Figure 3.4: Comparison of Muon and Pion Energy Deposition (left) and Track Matching (right)

matching to be worse – the pions will be part of jets and tracking efficiency tends to be reduced in a track dense environment.

We conclude that pion fakes are likely candidates to populate the eccentric tails of the energy deposition and track matching distributions. However, we cannot identify the tail events beyond the cuts as being primarily pion punch through. A substantial fraction of the tails can be identified with non-isolated real muon backgrounds, where an associated jet is produced near the muon and a portion of the jet energy is identified with the muon. In the non-isolated environment we also expect the track matching to be poorer. The generic jet background with real muon production is discussed in the final section of this chapter.

3.5.3 Fiducial and Quality Cuts

The cosmic ray filter looks for low quality tracks opposing the muon track position in (η, ϕ). If such a track exists and is significantly shifted in time position from the original track, the original muon is rejected as a cosmic ray. We expect all muons coming from the interaction point to be in time with the beam crossing and move outward in the detector. Cosmic Rays generally come from the top of the detector and move downward, thus creating two tracks on either side of the detector, well separated in time.

The fiducial cuts require that the muon track project into the muon chambers away from the edges of the chambers. The eta phi mapping of the fiducial region is shown in figure 4.1. The chamber efficiency drops off towards the edge of the chamber and is difficult to model in this region; to reduce possibly eccentric edge effects, we cut 5 cm away from the end of the chamber in the z direction and 2 cm in the x direction (x along the base of the chamber). The region in figure 4.1 defines our good, triggerable space. For consistency, we use the same definition of fiducial as in the acceptance studies described in chapter 4.

In table 3.2 we require a CMP chamber stub match only for those chambers of the CMU that are in fact covered by some portion of the CMP chambers. Figure 4.1 displays graphically which CMU chambers are covered. In this figure, the dotted lines mark the original fiducial boundaries of the CMU chambers. The dark grey regions have little or no CMP chamber coverage, and a CMP track stub is not required in this region. The light grey regions show the projected CMP coverage onto the CMU region, and a CMP track stub is required if the muon projects to this region. Note that the geometries of the two sets of chambers are very different; the CMU chambers are approximately cylindrical, while the CMP chambers have a rectangular geometry, thus explaining the curved CMP projections in the (η, ϕ) plane. The general scheme here is to make very loose cuts on the CMP chamber stub. However, CMP hits are required by the trigger at all trigger levels in a scheme matching figure 4.1. In this offline selection, we use the same scheme to be consistent – the fiducial region must be a triggerable region.

The "Fiducial Run" requirement rules out runs that were independently deemed to have some sort of operational problem. For example, non-fiducial runs may have experienced detector high voltage malfunctions, data acquisition errors or trigger problems.

Finally, we require the events to pass the inclusive single muon triggers at Level 1, 2 and 3; these triggers are described in the previous chapter. This requirement eliminates a small number of volunteers that failed to pass the inclusive triggers due to trigger inefficiency. These volunteers passed jet or other calorimeter based triggers; for consistency with efficiency calculations we must remove them from the data sample.

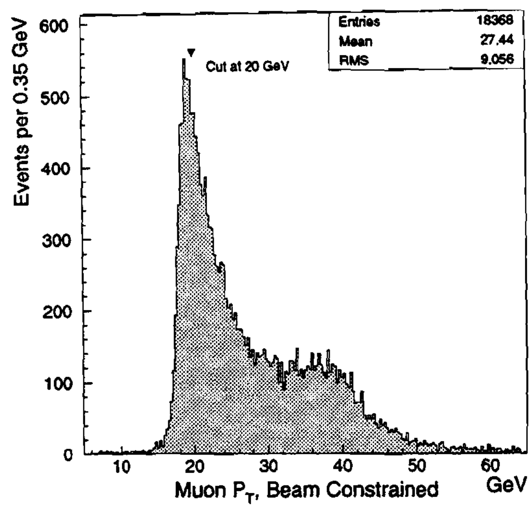

Figure 3.5: Inclusive Muon Transverse Momentum Spectrum

Cut, Primary High P_T Muon Sample	Events Remaining	Passing All But This Cut
Inclusive Muon Sample	15526	—
CMU $\|\delta x\| \leq 2.0\ cm$	14618	8646
CMP $\|\delta x\| \leq 5.0\ cm$	14154	8486
Isolation: $E_T(\Delta R \leq 0.4) \leq 2.0\ GeV$	9071	12899
Fiducial Run	8444	8966
Passes Level 1 Trigger	8417	8354
Passes Level 2 Trigger	8376	8394
Passes Level 3 Trigger	8354	8376
Primary High P_T Muons	**8354**	—

Table 3.3: Primary Muon Selection Cuts

3.6 Primary Muon Selection

From the starting point of the inclusive muon sample, we make stricter cuts to reduce background to create the primary muon sample, from which the W and Z samples are created. The additional cuts imposed are tighter track and muon stub matching, and more importantly an isolation cut. Table 3.3 lists the additional primary muon cuts and the corresponding candidate numbers. Note that we begin the event counts from the inclusive sample without fiducial run or trigger selections.

For the three cut quantities listed in table 3.3, figures 3.10 and 3.11 plot each

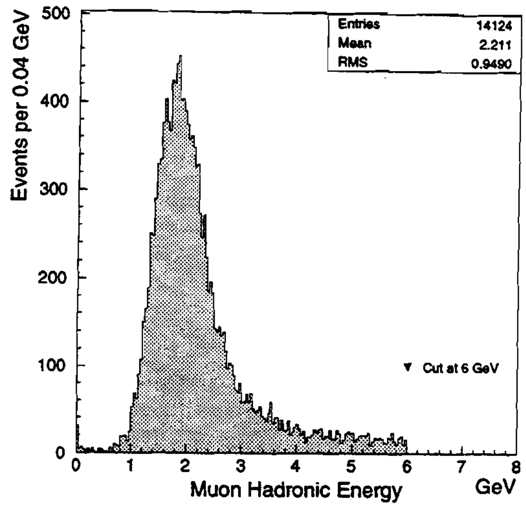

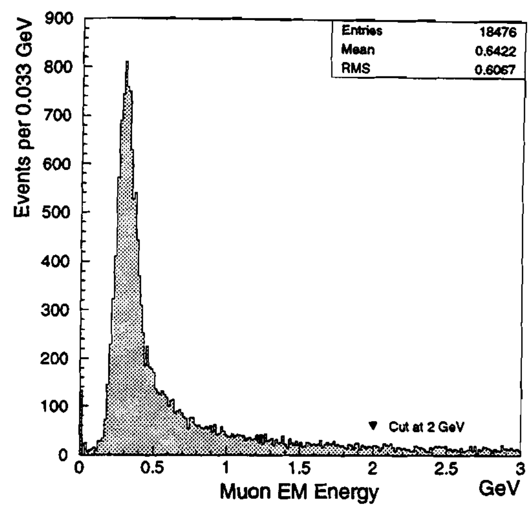

Figure 3.6: Inclusive Muon Energy Deposition

quantity from the primary sample with all cuts applied except the one plotted. The δx cuts for the CMU and CMP muon chambers are tightened to further reduce pion punch through background. We see from figures 3.3 and 3.4 that further tightening the δx cut will not significantly reduce the signal, but will eliminate a greater fraction of the pion background.

The quantity $E_T(0.4)$ is an isolation variable defined as:

$$E_T(0.4) = E_T(Cone\ \Delta R \leq 0.4) - E_T(Cone\ \Delta R \leq 0.13)$$

$E_T(0.4)$ is the transverse energy located in a ΔR cone of 0.4 around the muon track, subtracting out the minimum ionizing energy deposition due to the muon itself. As mentioned earlier, we expect muons from W and Z decay to be isolated. The plot on the right of figure 3.9 displays the IsaJet + Fast Detector Simulation prediction for $W \rightarrow \mu\nu$ events in the $\not{E}_T$ vs. $E_T(0.4)$ plane. The box indicates the W signal region, and clearly the W muons are preferentially isolated (similarly for the Z muons). Compare this with the IsaJet + Fast Detector Simulation prediction for generic two jet processes (b, c, s decays), figure 3.9 on the left, where the muons are not in general isolated. The primary purpose of the isolation cut is to remove such generic jet backgrounds, as is clear from the Monte Carlo predictions for the two processes. The equivalent plot for the data is in figure 6.1 in

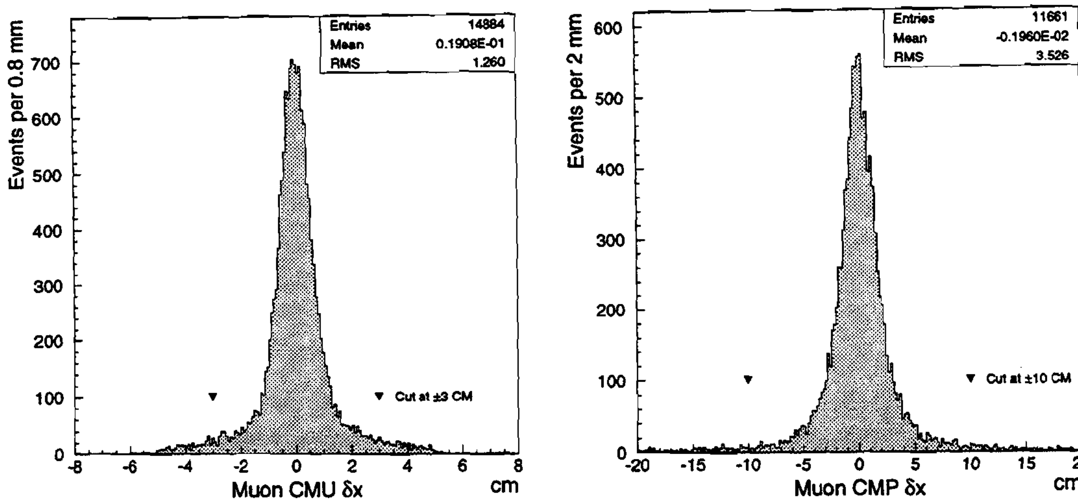

Figure 3.7: Inclusive Muon Track Matching

chapter 6, which distinctly indicates the presence of two separate physics populations as expected from the Monte Carlo predictions.

3.7 Z Candidate Events

To identify Z Candidates, we start with the primary muon sample and search events containing an additional minimum ionizing track. In order to increase the acceptance, the secondary muon is not required to hit any of the muon chambers. However, the track must fall within the fiducial tracking volume of the Central Tracking Chamber: $|\eta| \leq 1.2$. In table 3.4 we begin with the primary muon sample, without the Fiducial run and trigger selections applied. After all secondary muon identification cuts and the mass window cut are applied, we have 423 Z candidates.

Although no explicit muon chamber cuts are made on the second leg of the Z decay, we can tabulate how many of the secondary muons actually did hit the muon chambers and had a reconstructed muon stub. Table 3.5 lists the differing classifications of secondary muons.

In figure 3.12 (left) we plot the dimuon invariant mass spectrum of our sample, before having applied the mass cut. For comparison, a Monte Carlo prediction is overlayed, including both the resonant Z production and continuum Drell-Yan dimuon production

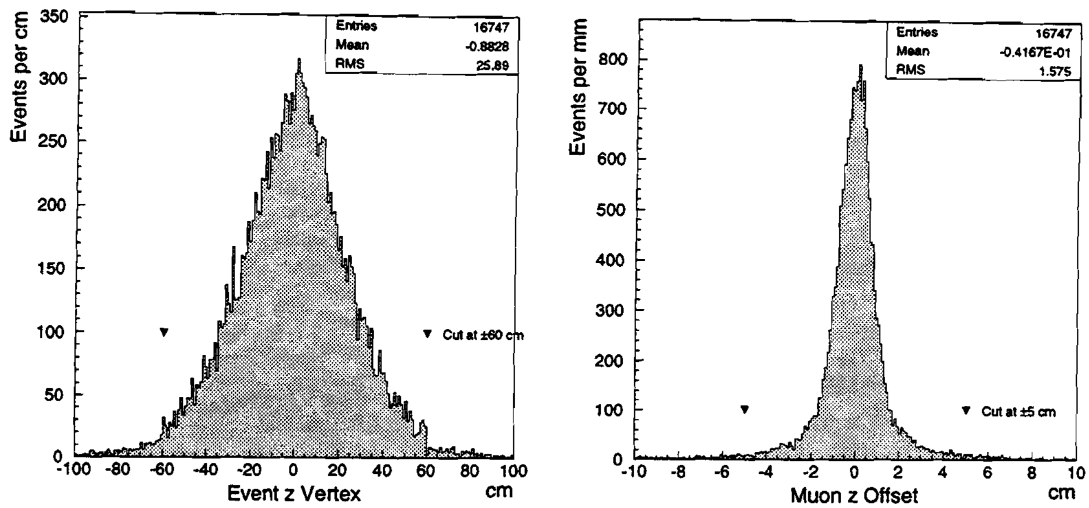

Figure 3.8: Inclusive Muon z Vertex Quantities

(see the acceptance and background chapters for further details regarding the Monte Carlo prediction). The prediction curve is normalized to the Z signal region. The Z resonance peak is clearly evident, with expected smearing due to tracking resolution. The location of the mass cuts for final Z identification are also indicated. The same figure 3.12 (right) is the mass distribution for the 423 Z candidates in the nominal Z mass region, with the same Monte Carlo prediction overlay on an expanded abscissa scale.

3.8 W Candidate Events

The W candidate selection begins with the primary muon sample, again without the fiducial run or trigger selections applied. First all Z candidates identified in the previous section are removed. The neutrino identification is then made with the missing transverse energy cut: $\not{E}_T \geq 20\ GeV$. Operationally, $\not{E}_T$ is computed initially from the the vector sum of all calorimeter towers, and is then corrected for the muons' track P_T and minimum ionizing energy:

$$\not{E}_x = -(E_x^{Calorimeter} + P_x^{\mu} - E_x^{m.i.})$$

$$\not{E}_y = -(E_y^{Calorimeter} + P_y^{\mu} - E_y^{m.i.})$$

$$\not{E}_T = \sqrt{\not{E}_x^2 + \not{E}_y^2}$$

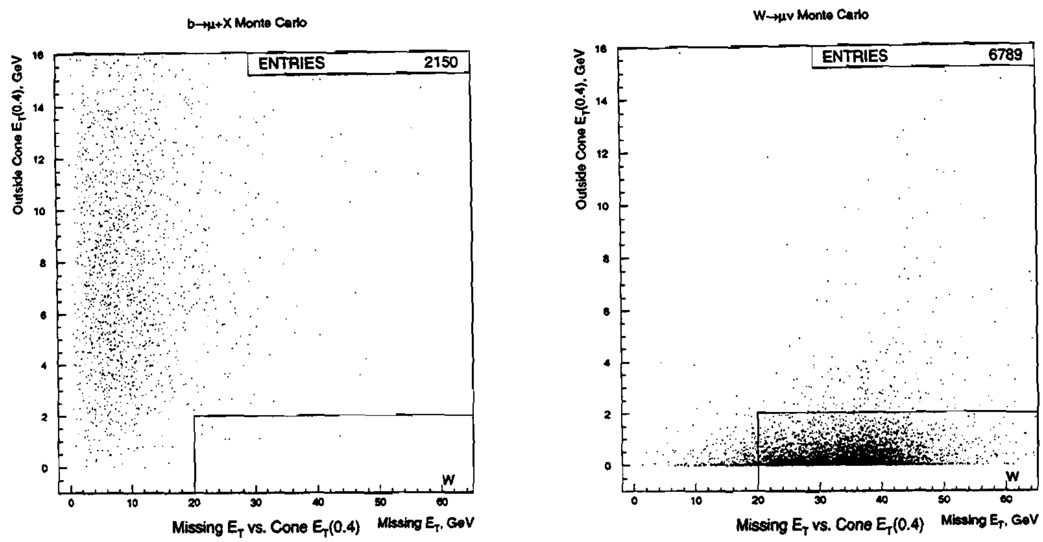

Figure 3.9: Monte Carlo Prediction, Isolation vs. $\not{E}_T$, Background (left) and Signal (right)

where the muon momentum value comes from CTC tracking data. Fiducial run and trigger requirements are applied, yielding 6222 W candidates, as listed in table 3.6.

From these 6222 W candidates, we plot the transverse mass in figure 3.13 (defined in section 3.2). Due to the kinematic nature of the transverse mass, the spectrum peaks below the W mass value and has a slowly falling tail towards zero. Due to muon momentum smearing and W transverse boost smearing of the W, we see a high mass tail. The Monte Carlo overlay in the histogram is described extensively in the acceptance section. The background contributes mainly in the lower mass area, as shown in the shaded portion of the histograms, further obscuring the shape of the spectrum in that region (described in the background chapter). The Monte Carlo plus background shapes are normalized to the total number of candidate events in the sample.

3.9 Inclusive Muons from non W and Z Processes

The inclusive muon P_T distribution in figure 3.5 displays a steeply falling spectrum with a distinct bump between about $P_T = 34\ GeV$ and $P_T = 40\ GeV$ due to W and Z production. To illustrate the background rejection power of the successive boson identification cuts, we plot overlays of the muon P_T spectra for the different classes of muons in

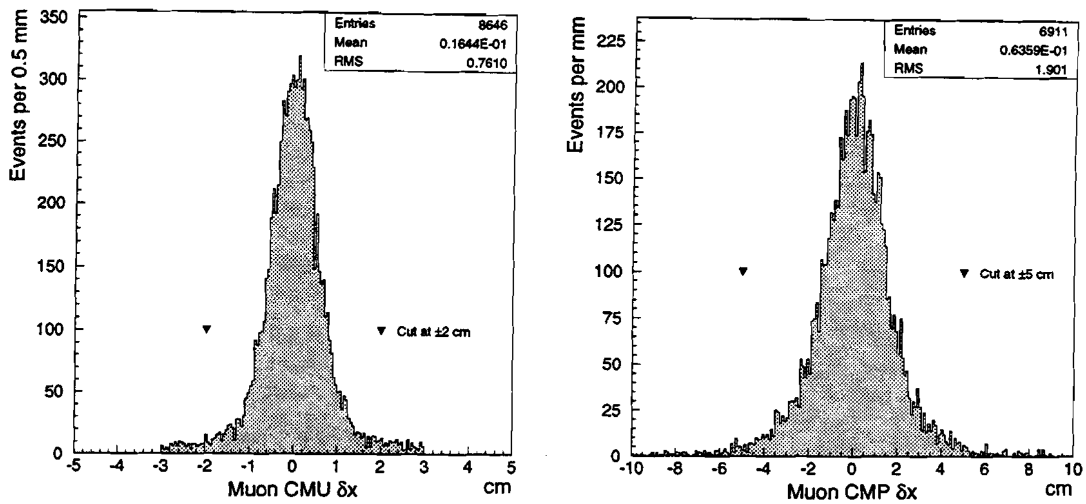

Figure 3.10: Primary Muon Matching Quantities

figure 3.14 (left). The final W selection eliminates a large fraction of the falling background spectrum, although a significant background fraction exists in the W sample, as discussed in the chapter 6.

To isolate background events in the inclusive muon spectrum we remove all W and Z candidates from the inclusive sample and plot the resulting P_T distribution in figure 3.14 (right). We expect some residual W and Z contamination to remain in this plot due to cut inefficiencies, but this effect should be small, especially since we see no bump evident in this distribution. Conversely, the W sample is not background free, so we do expect to remove some fraction of the background with the W removal.

In order to identify the source of these non W and Z inclusive muons, we divide the sources into three logical backgrounds:

1. Real muons from final state heavy quark decays, b *or* $c \rightarrow \mu + X$
2. Fake muons from punch through
3. Miscellaneous muons from jets, including pion decays: $\pi \rightarrow \mu + X$

The P_T spectra of all three processes are exceedingly difficult to model, and we describe here a qualitative way to account for the inclusive muon spectrum based on separating the spectrum into heavy quark and miscellaneous muon contributions.

For the heavy quark decays, we expect the decay process $b \rightarrow \mu + X$ to dominate, and for $c \rightarrow \mu + X$ to make a much smaller contribution. Note that we have neglected all lighter quark decays since they are highly kinematically suppressed. The muonic decay of

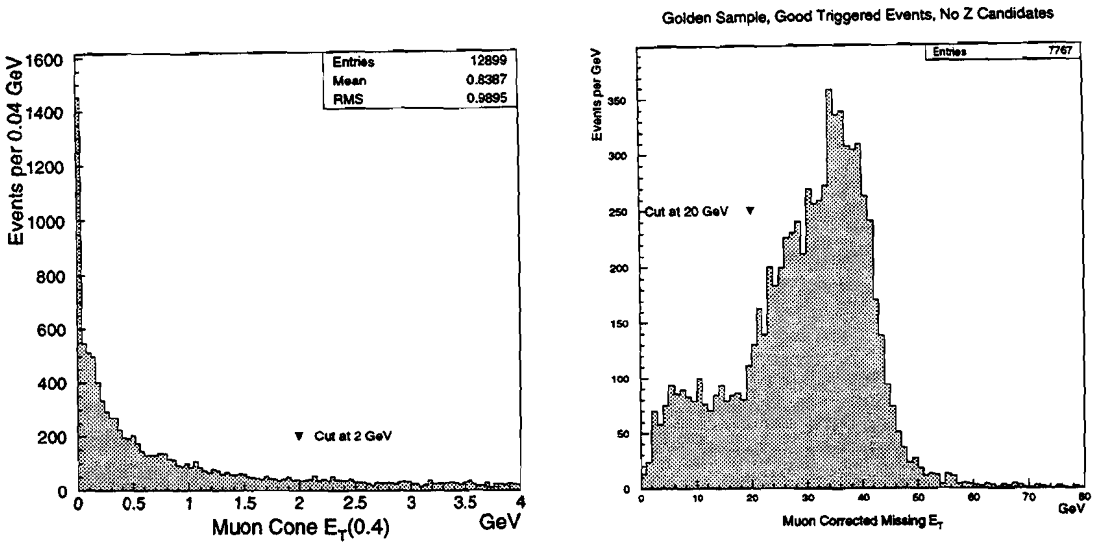

Figure 3.11: Primary Muon Isolation and Missing Transverse Energy

the b and c quarks is electroweak, but the behavior of the associated jets in the process (X) depend exquisitely on hadronization and fragmentation models and affect the detector signature. To model the b processes [44], we use a combination of the the IsaJet "TwoJet" b quark generator and a CLEO [46] B hadron fragmentation model. The events are then selected with muons in the final state. The detector simulation is common to that described in chapter 4. We also implement a simple model of the muon $P_T > 18$ GeV trigger to simulate the P_T efficiency turn on.

The resulting P_T spectrum is plotted in figure 3.15. Note that the P_T is not fully efficient until about 21 GeV. Therefore, we fit the distribution to an exponential convoluted with an arctangent efficiency parameterization in the $18 - 40$ GeV range. We exclude the high P_T region in the fit due to limited statistics and the difficulty in producing large Monte Carlo samples of this process at high P_T. The dashed line indicates our nominal signal region above 20 GeV.

The fake muons are far more difficult to model than the heavy quark processes with real muons. A Monte Carlo simulation of punch through muon fakes would be even more delicately sensitive to both jet fragmentation models as well as to fine details of the detector response to hadronic jets. As such, any Monte Carlo event simulator would be highly unreliable. Instead, we attempt to extract the punch through spectrum from the

Cut, Secondary Muon, Z Identification	Events Remaining
Primary Muon Sample	9071
$P_T \geq 18.0\ GeV$	870
$P_T \geq 20.0\ GeV$, Beam Constrained	818
Hadronic Energy $\leq 6.0\ GeV$	750
Electromagnetic Energy $\leq 2.0\ GeV$	716
$\lvert z_\mu - z_{Vertex}\rvert \leq 5.0\ cm$ $\lvert z_{Vertex}\rvert \leq 60.0\ cm$	664
Muon Track $\lvert\eta\rvert \leq 1.2$	567
Fiducial Run	518
Passes Level 1 Trigger	510
Passes Level 2 Trigger	502
Passes Level 3 Trigger	497
$66 \leq M_{\mu\mu} \leq 116\ GeV$	424
Opposite Charge	423
Z Candidates	**423**

Table 3.4: Z Candidate Cuts

Z Candidate Secondary Muon Class	Events
Central or Central+Upgrade, Fiducial	147
Central or Central+Upgrade, Non-Fiducial	15
Central Upgrade Only	32
Central Extension	98
No Chambers Hit (CMIO)	132
Z Candidates	**423**

Table 3.5: Z Candidate Secondary Muon Classifications

data itself by comparing the differences in P_T spectrum in the CMU and CMP regions of the detector.

We rely on the additional absorption lengths provided for the CMP chambers to provide additional punch through rejection. With three additional absorption lengths compared to the CMU chambers, we would expect roughly a factor of 20 reduction in the raw punch through probability in the CMP chambers. (The real relative rate reduction will be lower due to the minimum ionizing and track matching cuts applied to the sample.) We then compare the P_T spectrum in the so-called CMU Only region (no CMP chamber coverage) with the spectrum in the combined CMU+CMP coverage region in figure 3.16

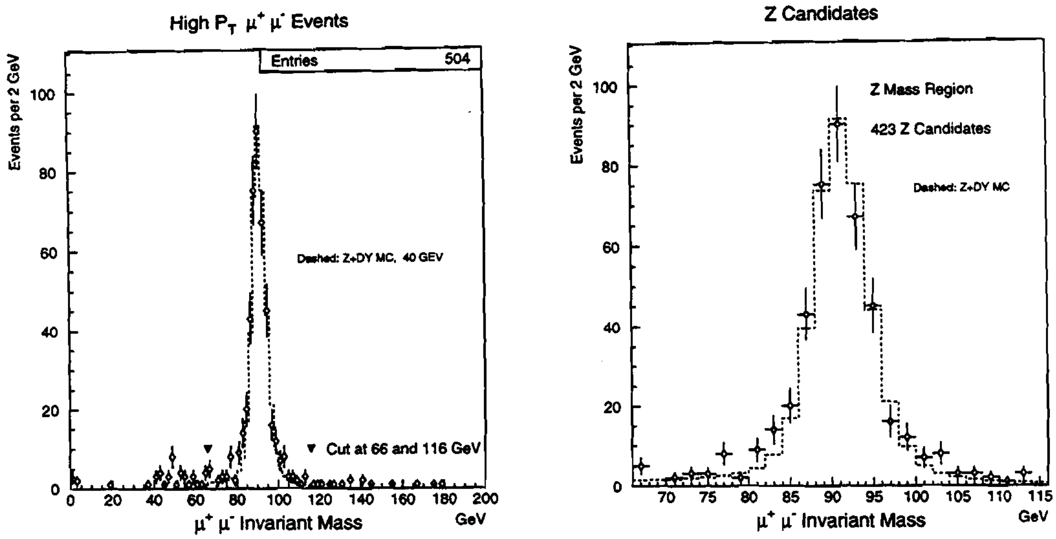

Figure 3.12: Dimuon Mass Spectrum with Z Candidates

Cut, W Identification	Events Remaining
Primary Muon Sample	9071
Exclude Z Candidates	8648
$\not{E}_T \geq 20\ GeV$, Muon Corrected, Beam Constrained	6739
Fiducial Run	6276
Passes Level 1 Trigger	6258
Passes Level 2 Trigger	6232
Passes Level 3 Trigger	6222
W Candidates	**6222**

Table 3.6: W Candidate Secondary Muon Classifications

(left). We have normalized the CMU+CMP spectrum to the CMU Only spectrum in the range $P_T = 34 - 40\ GeV$ in the inclusive sample, since we expect the events in this region to be less contaminated with punch through. (The distributions in figure 3.16 have the W and Z candidates removed.)

Note at lower P_T the difference between the two rates is substantial. The difference in shape of the two P_T spectra we attribute primarily to punch through and plot this difference in figure 3.16 on the right. We have fit the differential spectrum to an exponential in the same figure and note that it is steeply falling.

Finally, in comparing to the inclusive non W,Z muon P_T spectrum, we take the

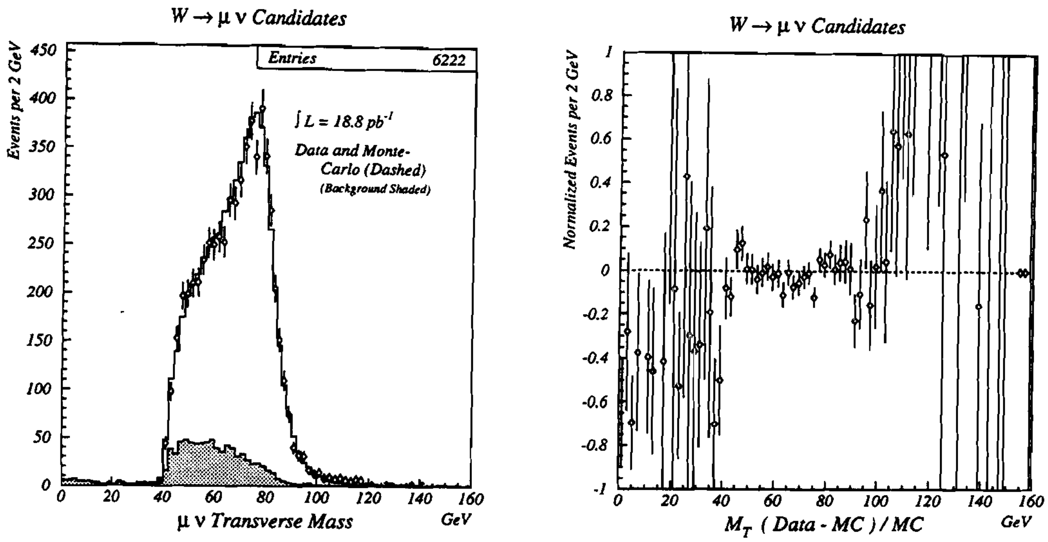

Figure 3.13: W Candidates Transverse Mass Spectrum

$b \rightarrow \mu + X$ spectrum as representative of the shape of heavy quark muon decay processes. The shape of the b and c spectra are not very different, and the c is kinematically suppressed by a factor of 5 [44]. We also take the punch through shape as representative of the remainder of miscellaneous processes, including both punch through, decays in flight and other fragmentation processes, abbreviated hereafter as the π spectrum.

However, neither of the two exponentially falling spectra can explain the long tails seen in the distribution. The exponential slope of the b and π spectra are nearly the same, so we attempt to fit the data to a sum of two exponentials, letting the slopes and relative normalization float. The result is plotted in figure 3.18 (linear scale left, logarithmic scale right). The dashed lines represent the individual exponentials and the solid line is the sum. The χ^2 to this fit is excellent and yields two exponential curves of very different slopes. We attribute the slowly falling exponential to residual W and Z events which were not removed from the sample. Note that this latter component of the distribution is essentially linear over the P_T range plotted, and could have been fit to a line equally as well.

Plot 3.17 shows a simple Monte Carlo simulation of $W \rightarrow \mu\nu$ events which fail to pass either the $\not{E}_T$ cut or the isolation cut. The distribution indicates a very slowly falling distribution. The slope extracted from the two exponential fit is plotted as the solid curve and is somewhat consistent with the simple Monte Carlo prediction. The Monte Carlo prefers a more steeply falling distribution, but the Monte Carlo does not include all

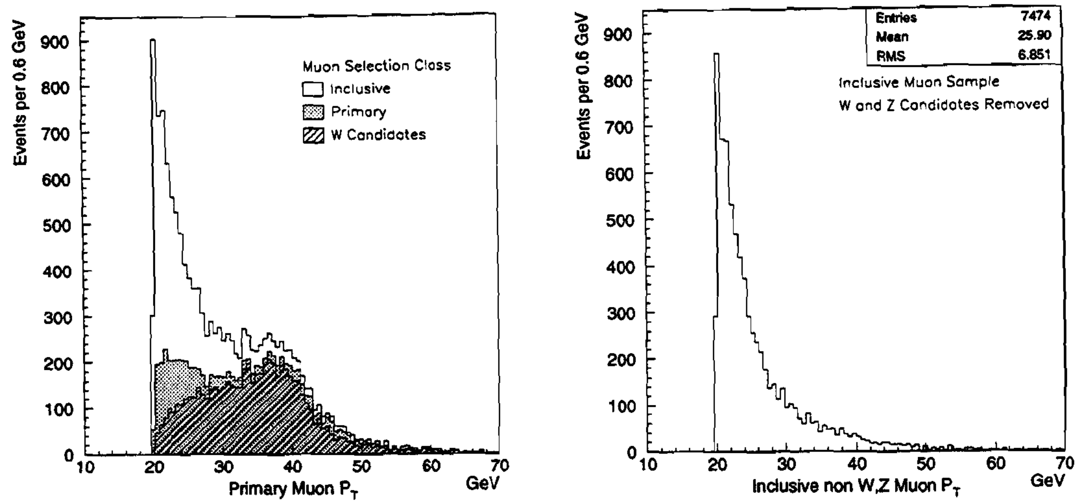

Figure 3.14: Muon Transverse Momentum Spectra by Class

QCD corrections, detector effects, or Z effects, so we choose the data fit parameters as the preferred values.

The relative fraction of the b to π spectrum cannot be trivially determined. The shapes of the two models are virtually identical above the P_T turn-on threshold and therefore we cannot fit the shape of the data spectrum to the relative fractions of b and π. Instead, we take a previously measured b-fraction of 31% [45] in the region above $P_T > 20\ GeV$ as the relative fraction of b to π in the exponential section of the curves. This fraction was determined by a study of decay length distributions in an inclusive muon sample with W and Z candidates removed and created with somewhat different muon selection criteria, but should be a valid enough approximation for our sample.

Taking the residual W (and Z) distribution with normalization from the two exponential fit and the 31% b to π fraction, we normalize the b plus π plus W distributions to the data and plot the result in figure 3.19 (linear scale left, logarithmic scale right). The three individual π, b and W contributions are plotted with dashed lines in the figure. The solid line is the sum of the three, and it yields a reasonable χ^2 value.

Figure 3.19 yields primarily a qualitative indication of the sources of the non W and Z high P_T muon sample. Many assumptions have gone into the input distribution models used here. The b fraction assumption may not be exactly correct. The miscellaneous muon model (π) may be quite different from the prediction of the underlying physics processes.

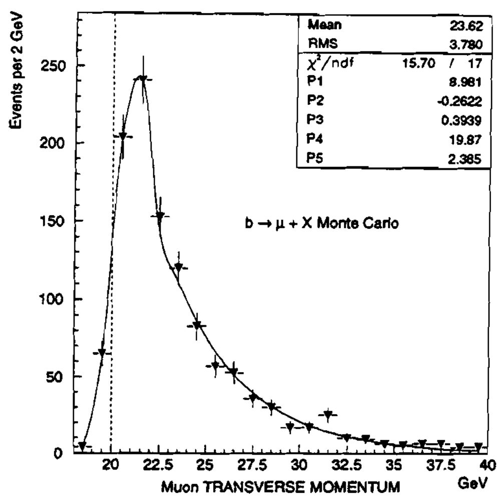

Figure 3.15: Predicted $b \to \mu + X$ Muon P_T Spectrum

The attributed models are at least qualitatively consistent with the non W, Z muon P_T spectrum using these naïve assumptions.

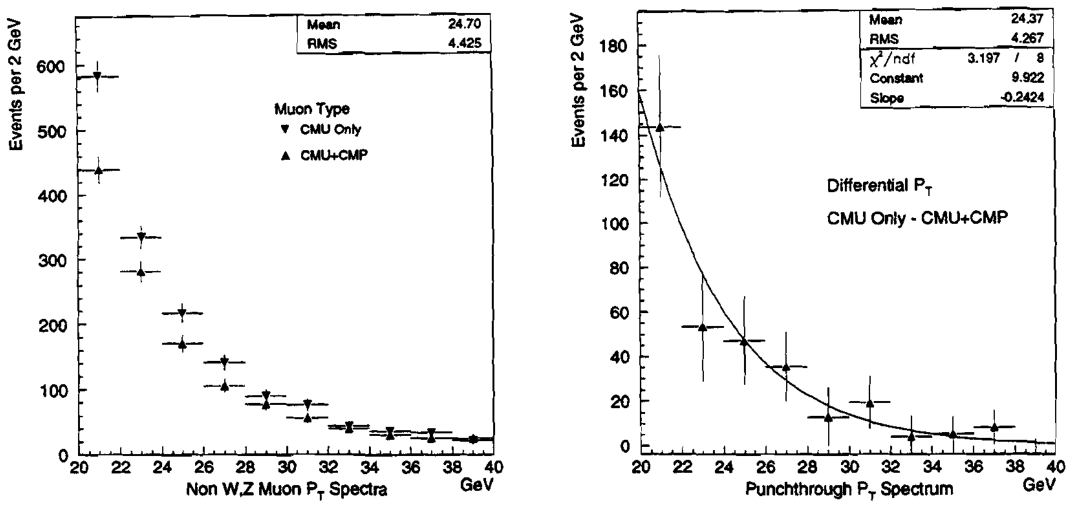

Figure 3.16: Extraction of Punch through Transverse Momentum Spectrum

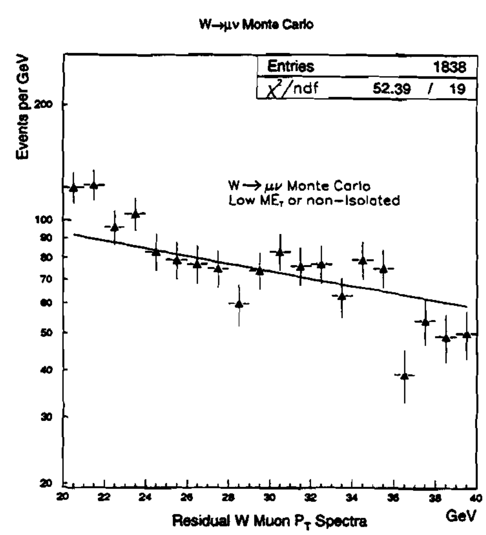

Figure 3.17: Predicted Non-Isolated or Low $\not{E}_T$ W Muon P_T Spectrum

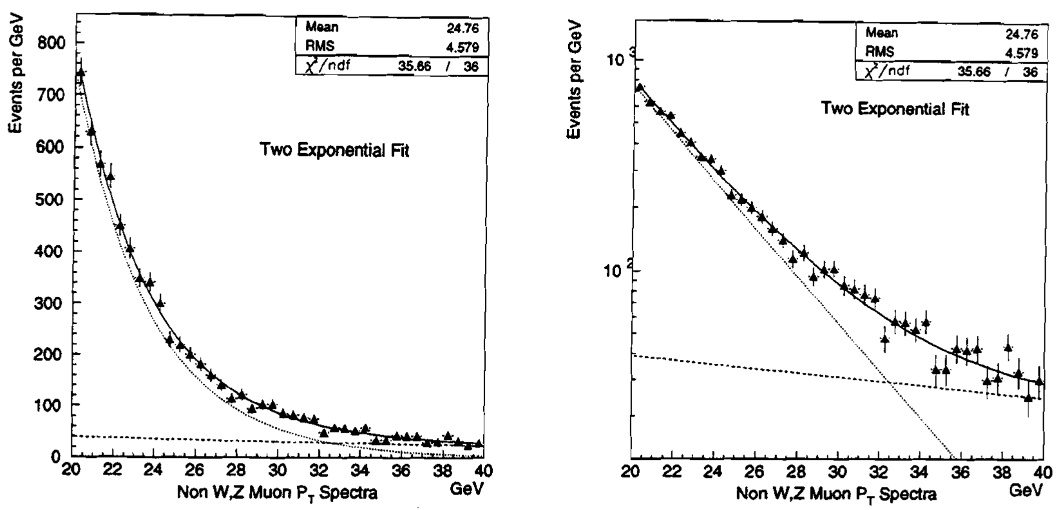

Figure 3.18: Fit of Non W and Z Muon P_T Spectrum to Two Exponentials

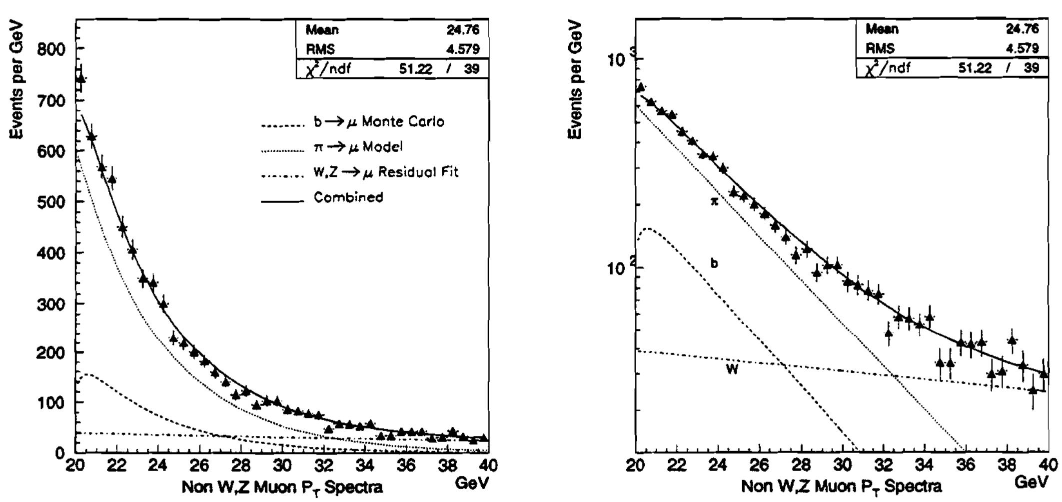

Figure 3.19: Fit of Non W and Z Muon P_T Spectrum to Models

Chapter 4

Geometric and Kinematic Acceptance

The overall net efficiency in detecting W and Z decay candidates factors into two terms: $\epsilon_{total} = A \cdot \epsilon$. We define A as the geometric and kinematic acceptance and ϵ as the data selection and trigger efficiencies. We leave computation of ϵ to the following chapter, and consider only A here.

The geometric acceptance indicates the fraction of W and Z decay leptons which fall within the fiducial detector region in detector (η, ϕ) coordinates. Figure 4.1 depicts the fiducial response regions of the central muon detectors in terms of η and ϕ. This map indicates the region allowed for primary muons – the fiducial region is identical in the Monte Carlo and in the data selection. Note that the differently shaded regions indicate where the outer layer (CMP) chamber hits are required. In the case of the primary lepton, the fiducial region must also have fiducial trigger response. The secondary lepton for Z candidates must simply fall in the range $|\eta| \leq 1.2$.

The kinematic acceptance is defined by the transverse momentum cuts on the primary and secondary leptons and the dimuon mass requirement for the Z sample. Through detector smearing effects and the effects of the underlying event, the geometric and kinematic effects are not easily factorable.

For the final cross section and ratio computations, we need several acceptance factors:

A_W	Acceptance for the process $W \rightarrow \mu\nu$
A_Z	Acceptance for the process $Z \rightarrow \mu\mu$
$\frac{A_Z}{A_W}$	Ratio of above W and Z Acceptances for R_μ Computation
$A_{Z,W}$	Acceptance for $Z \rightarrow \mu\mu$, one muon lost, for Background Calculation
$\frac{A_{Z,W}}{A_W}$	Ratio for Background Normalization to W Sample
$f_{\mu\mu}$	Fraction of A_Z where both muons land in primary fiducial volume

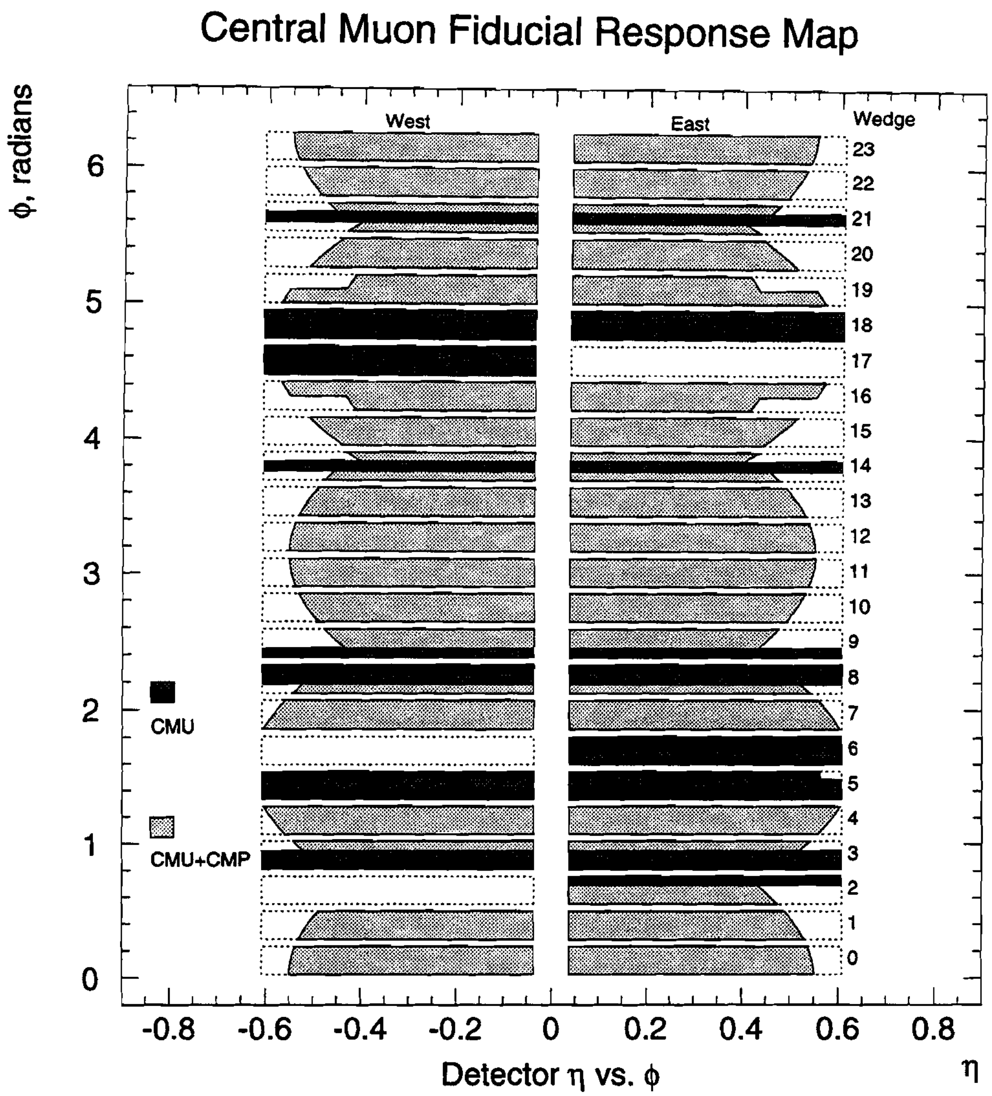

Figure 4.1: Fiducial Response Regions of the Central Muon Chambers

We calculate both the absolute acceptances and the fractional acceptances listed above, since systematic effects may affect ratios differently (see section on systematics, below). The factors involving $A_{Z,W}$ are needed to estimate the Z contamination in the W sample, and are further described in the chapter concerning backgrounds.

4.1 Monte Carlo Generator and Detector Model

Detector acceptance varies with lepton momentum and initial position, and so we must model the shape of these distributions using a Monte Carlo generator. We generate decay leptons using a tree level Monte Carlo [47] for both W and Z decays according to the leading order diagrams (figure 3.1). As a function of Q and y, the Monte Carlo generates Z events using:

$$\frac{d^2\sigma}{dydQ} = K(y)\cdot\frac{\pi G_F}{3\sqrt{2}}\cdot\frac{Q}{(Q^2-M_Z^2)^2+Q^4\Gamma(Z)^2/M_Z^2}\times$$
$$x_1x_2\cdot[(1-\frac{8}{3}\sin^2\theta_W+\frac{32}{9}\sin^4\theta_W)\cdot(u(x_1)u(x_2)+\bar{u}(x_1)\bar{u}(x_2)+2c(x_1)\bar{c}(x_2))+$$
$$(1-\frac{4}{3}\sin^2\theta_W+\frac{8}{9}\sin^4\theta_W)\cdot(d(x_1)d(x_2)+\bar{d}(x_1)\bar{d}(x_2)+2s(x_1)\bar{s}(x_2))]$$

Likewise, for W event generation, we have:

$$\frac{d^2\sigma}{dydQ} = K(y)\cdot\frac{2\pi G_F}{3\sqrt{2}}\cdot\frac{Q}{(Q^2-M_W^2)^2+Q^4\Gamma(W)^2/M_W^2}\times$$
$$x_1x_2\cdot[\cos^2\theta_C\cdot(u(x_1)d(x_2)+\bar{d}(x_1)\bar{u}(x_2)+2c(x_1)s(x_2))+$$
$$\sin^2\theta_C\cdot(u(x_1)s(x_2)+s(x_1)\bar{u}(x_2)+c(x_1)d(x_2)+\bar{d}(x_2)c(x_2))]$$

where x_1 and x_2 are the momentum fractions and we neglect the higher order corrections to the K factor:

$$x_1=\frac{Q}{\sqrt{s}}e^y \qquad x_2=\frac{Q}{\sqrt{s}}e^{-y} \qquad K(y)\to 1$$

The parton distribution functions above are defined as:

$$u=u_p^v+u_p^s \quad \bar{u}=u_p^s \quad d=d_p^v+d_p^s \quad \bar{d}=d_p^s \quad s=\bar{s}=s_p^s \quad c=\bar{c}=c_p^s$$

where p indicates that these are the distributions of the proton; v indicates valence quark; s indicates sea quark. Up, down, charm and strange (u,d,c,s) contributions are included as well as an asymmetric u and d sea; bottom and top are neglected. The $MRS\ D'_-$ next-to-leading order parton distribution functions [48] model the incoming quark momenta; throughout the acceptance studies we use the $MRS\ D'_-$ functions as nominal since they best fit our measured W charge asymmetry [55] out of all the recent parameterizations.

The decay leptons are then given a boost according to the previously measured boson transverse momentum spectrum [64]. The resulting muon momenta are then smeared according to the measured transverse momentum resolution:

$$\frac{\delta P_T}{P_T^2} = 0.0009 \pm 0.0002$$

where P_T is measured in GeV.

The boosted muons are then propagated through the solenoidal magnetic field out to the calorimeters, traversing a circular path in the transverse plane. Outside the magnetic field, the muons follow a straight line trajectory through the calorimeter to the inner layer of the Central Muon chambers (CMU), correcting for multiple scattering and dE/dx energy loss while passing through the material. The muon track is then propagated out to the Central Muon Upgrade chambers (CMP). If the track hits either one of the sets of muon chambers, the same fiducial cuts are applied based on position in the chamber that are applied to the data. CMP chamber confirmation is required only for the CMU chambers that are nominally covered by the CMP chambers, in the identical manner to the offline cuts and the online trigger scheme.

In the case of the W Monte Carlos (including Z faking W) an underlying event vector is added to smear the simulated missing transverse momentum. The underlying event vector is determined by a combination of simulation and data, described below. The simulated missing transverse energy is then cut at $\not{E}_T \geq 20\ GeV$ to accept the simulated W candidates.

For the Z Monte Carlos, both muons are propagated through the detector. At least one muon is required to land in the central fiducial chamber region, either CMU or $CMU + CMP$ regions. If both muons land in the central fiducial region, then the event is classified as "fiducial, fiducial". Otherwise the secondary muon is required to fall within a central tracking chamber detector eta of $|\eta| \leq 1.2$. The fraction of the total Z acceptance where both muons fall into the "fiducial, fiducial" region is given by $f_{\mu\mu}$. This number is needed since the efficiencies for the $f_{\mu\mu}$ events differ from the complementary set where one muon leg falls beyond the central region, where the efficiencies are very different; the complementary "fiducial, non-fiducial" region forms a $(1 - f_{\mu\mu})$ fraction of Z acceptance. Note that "fiducial" muons fall into the primary muon selection region: they must hit the CMU or $CMU + CMP$ detectors. "Non-fiducial" muons do not hit the muon chambers, but must fall within the good CTC tracking region. "Non-fiducial" muons can only be secondary muons, but secondary muons can be either "fiducial" or "non-fiducial".

In the Z case where one of the muons falls into the central fiducial region, but the secondary muon falls beyond the eta cut, $|\eta| > 1.2$, then the event has a chance to fake a W. The acceptance for this situation ($A_{Z,W}$) must be well understood in order to estimate the "$Z \rightarrow \mu\mu$, one muon lost" background to the W sample. In the Z Monte Carlo, if the secondary muon falls beyond the η cut, we ignore this muon and treat the remaining primary muon as a W event. The single primary muon must fall within the central CMU or CMU+CMP fiducial region, and we add an underlying event as in the W acceptance Monte Carlo. W identification cuts are then applied on the single muon P_T and the $\not{E}_T$; in every way, the one legged Z is simulated as if it were a W. The resulting "Z fakes W" acceptance is given by $A_{Z,W}$ and is used in the background calculation.

4.2 Systematic Uncertainties

With a fast event generator and detector simulator, we can make high statistics studies of various systematic effects that can shift the value of the acceptance. For each source of systematic uncertainty, we vary the effect in question while holding all else constant and compute the resulting acceptance. We then use the spread in resulting acceptance values as the systematic uncertainty due to the particular effect. This section enumerates the several effects.

4.2.1 Parton Distribution Functions

In recent years our knowledge of the parton distribution functions (PDFs) of the proton sea and valence quarks and gluons has increased substantially. Some older parameterizations have been excluded, and new ones have been published that more closely match the data. We have chosen the $MRS\ D'_-$ parameterization for the Monte Carlo event generator since it best fits our W charge asymmetry measurement [55] – this measurement is our most sensitive probe of the parton structure.

However, a number of other parameterizations are not excluded. The PDFs govern the initial state kinematics of the incoming quark, and so affect the outgoing W and Z decay muons, thus potentially altering the acceptances. We measure our sensitivity to PDFs by repeating the acceptance calculations using several different sets of PDF parameterizations. In addition to the nominal $MRS\ D'_-$, we use the $MRS\ D'_0$, $MRS\ S'_0$

PDF	A_W, %	A_Z, %	A_Z/A_W	$A_{Z,W}$, %	$A_{Z,W}/A_Z$	$f_{\mu\mu}$
$MRS\ D'_-$	16.192	16.489	1.0183	14.637	0.8877	0.20314
$MRS\ D'_0$	16.546	16.818	1.0164	14.717	0.8751	0.20272
$MRS\ S'_0$	16.585	16.854	1.0162	14.777	0.8768	0.20414
$CTEQ2\ M$	16.187	16.501	1.0194	14.661	0.8885	0.20300
$CTEQ2\ MS$	16.241	16.705	1.0286	14.657	0.8774	0.20370
$CTEQ2\ MF$	16.507	16.744	1.0143	14.731	0.8798	0.20465
$CTEQ2\ ML$	16.232	16.535	1.0187	14.714	0.8899	0.20261
PDF δ	0.199	0.183	0.0071	0.070	0.0074	0.00102

Table 4.1: Effect of Parton Distribution Functions on Acceptances

$M_W, sin^2\theta_W$	A_W, %	A_Z, %	A_Z/A_W	$A_{Z,W}$, %	$A_{Z,W}/A_Z$	$f_{\mu\mu}$
80.03, 0.2228	16.187	16.345	1.0098	14.667	0.8973	0.20405
80.21, 0.2263	16.192	16.489	1.0183	14.637	0.8877	0.20314
80.39, 0.2297	16.294	16.643	1.0214	14.526	0.8728	0.20320
$M_W, sin^2\theta_W$ δ	0.053	0.149	0.0058	0.070	0.0122	0.00045

Table 4.2: Effect of W Mass on Acceptances

parameterizations from the same collaboration [48]. The CTEQ Collaboration has also produced fits consistent with our data [54] ; we use their parameterizations: $CTEQ2\ M$, $CTEQ2\ MS$, $CTEQ2\ MF$, and $CTEQ2\ ML$.

Table 4.1 lists the acceptances for each of these PDF parameterizations. We take the uncertainty in the acceptance due to the PDFs as the spread in the acceptance values.

4.2.2 M_W *and* $sin^2\theta_W$

The kinematic structure of the events is also influenced by the mass of the intermediate vector bosons. Uncertainty in the mass values influences the acceptance. The LEP collaborations have measured the mass of the Z to remarkable accuracy; we use:

$$M_Z = 91.187 \pm 0.007\ GeV \quad [16]$$

The 7 MeV uncertainty in the Z mass does not affect our acceptance calculations. LEP also predicts a W mass, assuming the standard model extrapolation of $sin^2\hat{\theta}_W^{effective}$. Our aim is to test the consistency of the electroweak standard model, so we do not use this value. Instead, we use the best W mass value from direct production collider experiments:

P_T Distribution	A_W, %	A_Z, %	A_Z/A_W	$A_{Z,W}$, %	$A_{Z,W}/A_Z$	$f_{\mu\mu}$
Soft (-1 σ)	16.309	16.406	1.0059	14.848	0.9050	0.20438
Nominal	16.192	16.489	1.0183	14.637	0.8877	0.20314
Hard (+1 σ)	16.092	16.649	1.0346	14.287	0.8581	0.20341
P_T Distribution δ	0.109	0.121	0.0143	0.280	0.0234	0.00062

Table 4.3: Effect of Boson P_T on Acceptance

$$M_W = 80.21 \pm 0.18 \; GeV \quad [56]$$

The relatively large uncertainty on the W Mass does affect the acceptance calculations. We run the calculations three times, using the central value and the $\pm 1\sigma$ values of the W mass, tabulated in table 4.2.

The Monte Carlo generator involves only tree level production. Therefore, we use the tree level value for the electroweak mixing angle:

$$sin^2\theta_W = 1 - \frac{M_W^2}{M_Z^2} = 0.2263 \pm 0.0034$$

Here we use the directly measured W and Z masses. Again, we run the calculations three times while varying the W mass $\pm 1\sigma$. The LEP predicted value is not used; we can consider the uncertainty here as due to the lack of electroweak higher order corrections in the event generator. The uncertainty due to the M_W and $sin^2\theta_W$ errors is taken as the spread in the resulting $\pm 1\sigma$ acceptance values in table 4.2 .

4.2.3 Boson P_T Distribution

The tree level generator does not include the effect of final state QCD jet production. Typically these jets come from associated gluon radiation off of an incoming quark line or via quark-gluon fusion; both processes are indicated schematically in figure 4.2 (left two diagrams). The boson recoils off of this jet, giving it a transverse boost. To minimize model dependence, we use the previously measured boson P_T spectrum [64] to model the effect of the recoil jet. We use a parameterization of the boson P_T spectrum from the data, consistent with both the individual W and Z spectra.

To measure the effect of the uncertainty in the input spectrum, we vary the P_T

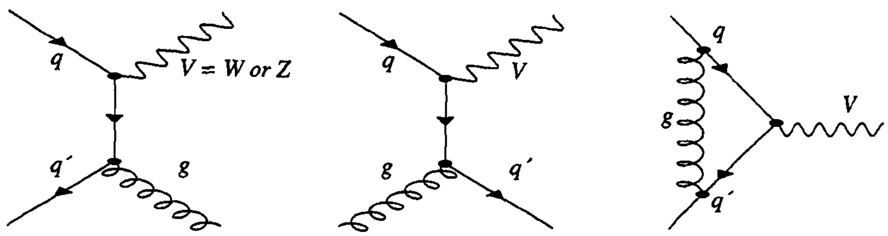

Figure 4.2: Associated Gluon Jet Production Processes and Gluon Vertex Correction

Model	A_W, %	A_Z, %	A_Z/A_W	$A_{Z,W}$, %	$A_{Z,W}/A_Z$	$f_{\mu\mu}$
W'	16.314	16.463	1.0091	14.748	0.8959	0.20212
Nominal	16.192	16.489	1.0183	14.637	0.8877	0.20314
W' + Min Bias	16.160	16.446	1.0177	14.642	0.8903	0.20339
UE Model δ	0.077	0.000	0.0046	0.056	0.0041	0.00000

Table 4.4: Effect of Underlying Event Model on Acceptance

parameterization $+1\sigma$ (harder) and -1σ (softer) and recompute the acceptances. Table 4.3 lists the results with the error due to the spread in values.

4.2.4 Underlying Event Model

The underlying event smears the overall missing transverse energy, and pertains only to the W acceptance and the "Z fakes W" acceptance. The underlying event can be divided into two components: Jet Recoil and Minimum Bias. The model used here was developed previously in reference [60], and is described extensively there.

The minimum bias component comes from debris associated with the spectator partons or with a multiple, simultaneous interaction between two separate $p\bar{p}$ pairs. Overall, spectator and multiple interaction contributions should be symmetric in ϕ, uncorrelated with the boson P_T . We model this contribution by examining events coming from our minimum bias trigger, and using the measured (E_x, E_y) components, which contains both resolution and the input spectrum.

Jet recoil refers to the jets off of which the boson is recoiling, as described in the previous section. Jet recoil should balance the the boson P_T, but does not exactly due to the particular contents of the jets and the variable detector response. On average, the detector response will degrade the jet energy by a factor of ~ 1.4. Jet response is modeled by a fast detector simulation, and varies with jet P_T.

Since these models may not completely cover all effects in the underlying event, we repeat the acceptance calculations using a parameterization from the IsaJet Monte Carlo [62] and a full, detailed detector simulation. This parameterization was originally developed in reference [61] for a W' boson search. The results are listed in table 4.4 in the W' row. In addition, we worry that the minimum bias contribution from multiple interactions is luminosity dependent. At instantaneous luminosities of $\mathcal{L} \sim 5 \times 10^{30}\ cm^{-2}sec^{-1}$ we expect typically one minimum bias interaction per crossing. To study a worst-case scenario, we run the Monte Carlo adding two minimum bias events (on average, poisson fluctuated). The results from this study are listed in table 4.4 in the W' + Min Bias row.

4.2.5 Track Curvature and Polar Angle Smearing

The kinematic cut $P_T \geq 20\ GeV$ may be sensitive to the smearing applied to the muon tracks. The actual curvature smearing of $\delta P_T = (0.0009 \pm 0.0002) \cdot P_T^2$ is measured in reference [56] by fitting to the Z candidate dimuon and dielectron mass spectra. To account for possible (small) differences in data selection and track fit constraints in the data sample, we vary the curvature smearing by 2σ in $\pm 1\sigma$ steps around the nominal value. As we see from table 4.5, the variation is barely distinguishable from the Monte Carlo statistical error.

The track fit parameter $\cot\theta$ is another potential source of track smearing uncertainty in the acceptance, and would most closely affect the P_z and η of the track. The nominal uncertainty in this parameter is $\delta \cot\theta \sim 0.004$. Varying this parameter over a wide range of values from 0.000 to 0.008 results in no measurable change in the W or Z acceptances; therefore we do not include this parameter as a source of uncertainty.

4.2.6 Event z Vertex Distribution

The position of the event vertex in the longitudinal direction varies approximately as a Gaussian centered near the center of the detector in the z direction. The typical Gaussian mean and width are:

$$z_0 = -1.48 \pm 0.11\ cm \qquad \sigma_z = 26.65 \pm 0.18\ cm$$

$\delta P_T/P_T^2$	A_W, %	A_Z, %	A_Z/A_W	$A_{Z,W}$, %	$A_{Z,W}/A_Z$	$f_{\mu\mu}$
0.0005	16.201	16.436	1.0145	14.683	0.8933	0.20352
0.0007	16.196	16.453	1.0159	14.665	0.8914	0.20460
0.0009 (Nominal)	16.192	16.489	1.0183	14.637	0.8877	0.20314
0.0011	16.186	16.461	1.0170	14.624	0.8884	0.20484
0.0013	16.184	16.458	1.0169	14.605	0.8874	0.20378
$\delta P_T/P_T^2$ δ	0.008	0.026	0.0019	0.039	0.0029	0.00085

Table 4.5: Effect of Track Smearing on Acceptance

Variation	A_W, %	A_Z, %	A_Z/A_W	$A_{Z,W}$, %	$A_{Z,W}/A_Z$	$f_{\mu\mu}$
$z_{min} \rightarrow 0.0\ cm$	16.208	16.467	1.0160	14.632	0.8885	0.20349
$z_{min} \rightarrow \times 2$	16.271	16.489	1.0133	14.656	0.8888	0.20358
$\beta^*_{eff} = 30.5\ cm$	16.212	16.533	1.0198	14.590	0.8825	0.20212
$\beta^*_{eff} = 35.5\ cm$	16.222	16.428	1.0127	14.615	0.8897	0.20399
$\sigma_z \rightarrow -6.5\%$	16.229	16.474	1.0151	14.639	0.8886	0.20310
$\sigma_z \rightarrow +6.5\%$	16.225	16.454	1.0141	14.639	0.8897	0.20290
Nominal	16.192	16.489	1.0183	14.637	0.8877	0.20314
z_{vertex} δ	0.046	0.057	0.0048	0.026	0.0038	0.00096

Table 4.6: Effect of Event z Vertex Distribution on Acceptance

Where z_0 is measured from the center of the detector. The actual shape of the distribution changes with the Tevatron beam parameters from run to run. In fact, the distribution is not truly Gaussian, but follows a form according to the Tevatron luminosity function:

$$\frac{d\mathcal{L}(z)}{dz} \propto \frac{e^{\frac{z^2}{2\sigma_z^2}}}{[1+(\frac{z-z_{min}}{\beta^*})^2]}$$

This proportionality is described in detail in the Luminosity chapter (chapter 7). To model the acceptance, we use the run averaged form derived in chapter 7 in the region $|z| \leq 60\ cm$.

The event z vertex cut effectively reduces the luminosity acceptance by an efficiency factor of ϵ_{vertex}. However, note that we do not include the effect of the z vertex cut in the value of the geometric acceptances quoted in this chapter. This cut is primarily a correction to the luminosity; the efficiency of the cut completely cancels in the ratio of the W and Z cross sections and so we defer discussion of the efficiency ϵ_{vertex} until chapter 7.

The uncertainty due to the z distribution comes from the variations of the shape of the distribution in the $|z| \leq 60\ cm$ region. To estimate the uncertainty, we vary the beam parameters in the $d\mathcal{L}(z)$ function and see the effect on the acceptance. We separately vary

Uncertainty	A_W, %	A_Z, %	A_Z/A_W	$A_{Z,W}$, %	$A_{Z,W}/A_Z$	$f_{\mu\mu}$
PDFs	0.199	0.183	0.0071	0.070	0.0074	0.00102
$M_W, sin^2\theta_W$	0.053	0.149	0.0058	0.070	0.0122	0.00045
Boson P_T	0.109	0.121	0.0143	0.280	0.0234	0.00062
UE Model	0.077	0.000	0.0046	0.056	0.0041	0.00000
Track Smearing	0.008	0.026	0.0019	0.039	0.0029	0.00085
z Vertex	0.046	0.057	0.0048	0.026	0.0038	0.00096
Statistical	0.037	0.037	0.0033	0.035	0.0029	0.00046
Total Error	0.253	0.275	0.0187	0.308	0.0283	0.00187
Value	16.192	16.489	1.0183	14.637	0.8877	0.20314

Table 4.7: Summary of Acceptance Uncertainties

β^*_{eff}, z_{min}, and σ_z by their estimated amount of variation as determined in chapter 7. The results are listed in table 4.6. We see that the acceptances are quite insensitive to changes in the shape of the luminosity function.

4.3 Summary of Acceptances and Uncertainties

Table 4.7 lists all sources of systematic error in the acceptance that we have considered here. We note that the dominant source of systematic error in the individual W and Z acceptances is the variation due to differing parton distribution functions.

4.4 Comparison to Data

As a consistency check, we compare the Monte Carlo generated η and ϕ distributions with our data samples. In each comparison, the dashed line represents the Monte Carlo prediction, normalized to the number of candidate events; the data points are overlayed, with statistical errors only. Figure 4.3 displays the results for the W candidates. The phi plot on the left is in terms of the 24 detector wedges, divided into east and west halves; note the three wedges excluded from the fiducial region. On the right of figure 4.3 is the η plot for the same sample in terms of CMU detector η; the Monte Carlo is corrected for the shape of the differential CFT efficiency described in the efficiency chapter.

Figure 4.4 plots the central tracking chamber exit $|\eta|$ for both legs of the Z decay. The excess in the central region is due to the requirement that at least one of the muons

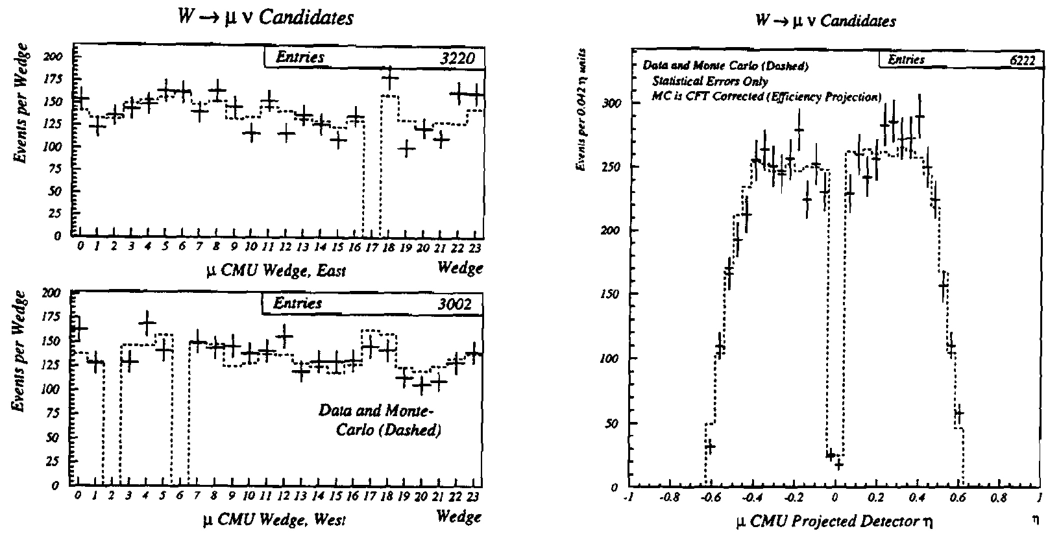

Figure 4.3: W Candidates ϕ and η Distributions

must land in the central detector. The deficit near $|\eta| = 0$ is due to the detector crack at $\theta = 90^\circ$. The errors are statistical only.

In figure 3.12 (chapter 3) we plot the dimuon invariant mass distribution using the same Monte Carlo, comparing the results to the Z candidates on the right. We note that the actual visible cross section represents a combination of Z and γ intermediate states, and as such the Monte Carlo was modified to include the continuum Drell-Yan production for this comparison. See chapter 6 for further discussion of the Drell-Yan background to the Z sample. The Monte Carlo histogram is normalized to the Z mass signal region in both plots of figure 3.12.

Figure 3.13 compares the W transverse mass distributions for the data to the identical W Monte Carlo used in the acceptance. This plot includes a model of the W backgrounds as outlined in detail in chapter 6. The total Monte Carlo, including backgrounds, is normalized to the area under the data curve.

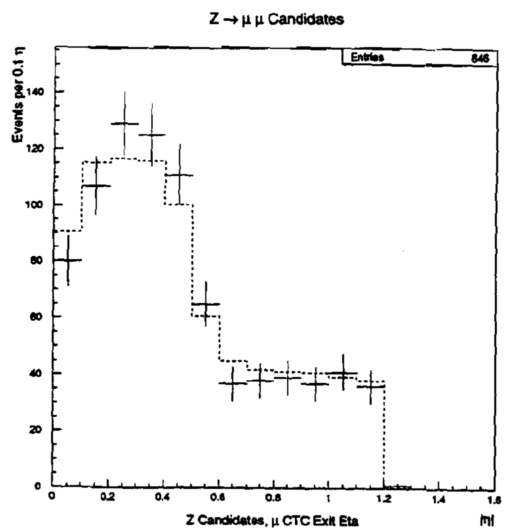

Figure 4.4: Z Candidates η Distribution

Chapter 5

Detector and Identification Efficiencies

In computing cross sections, efficiencies must be carefully calculated for every single cut that is made. All cuts must be understood: offline cuts used in creating the data samples as well as the effective online cuts used in detector triggering. Taking the ratio of cross sections substantially reduces the dependence on the efficiencies, but does not completely remove it.

Unlike the geometric and kinematic acceptances, we compute selection efficiencies directly from the data samples so as not to be reliant on Monte Carlo simulations of the details of the detector.

5.1 Muon Selection Efficiencies

Unfortunately, no high statistics control sample exists to study inclusive muon efficiencies. Only a tiny handful of events in the $W \to \mu\nu$ candidate sample were triggered by an independent trigger path; these independent triggers involve jet requirements, and may bias the efficiencies. The $Z \to \mu\mu$ candidate sample provides the best way to compute both offline selection and trigger efficiencies. We take advantage of the fact that dimuon events have two chances to pass either a cut or the trigger. By using the Z sample, we gain in believability: W and Z decays will both produce isolated muons with similar momentum spectra.

The primary disadvantage of using the Z sample is the low statistics. We could gain statistics by using the $J/\psi \to \mu\mu$ dimuon sample. However, the kinematics and isolation of these events is very different from Z decays. J/ψ decay muons are often not as well separated in (η, ϕ) and are often not isolated from associated jets. The systematic penalty involved in using the lower momentum muons in the efficiency calculations would be almost impossible to understand.

For most muon efficiency calculations, we will use various fiducial subsets of the Z candidates and rely on a simple probability argument: when $Z \rightarrow \mu_1\mu_2$, then each muon has a chance to pass the cut. For a single muon cut efficiency of ϵ, then there are four cases:

ϵ^2	Probability both muons pass the cut
$\epsilon \cdot (1-\epsilon)$	Probability μ_1 passes cut, μ_2 fails
$(1-\epsilon) \cdot \epsilon$	Probability μ_1 fails cut, μ_2 passes
$(1-\epsilon)^2$	Probability both muons fail cut (Not observed)

We observe the first three cases. By counting the number of events where both muons pass the cut to the events where only a single muon passes the cut, we can extract the efficiency ϵ. The general scheme is:

1. Only require one muon to pass the cut of interest, then:

   N_T = Total Events with one or two muons passing cut
2. Make the usual opposite charge and dimuon mass cuts: $66 \leq M_{\mu\mu} \leq 116\ GeV$
3. Count number of events with both legs passing the cut:

   N_B = Number of Events with both muons passing cut
4. Efficiency ϵ is then:

   $\epsilon = \frac{2R}{(1+R)}$ Where $R = \frac{N_B}{N_T}$

The error in the efficiency is then taken as the Poisson statistical error (in general it will be asymmetric). The statistical error is always large, so we neglect any small systematic effects due to differences in kinematics between W and Z decay events.

5.2 Muon Identification Cut Efficiencies

For the general offline muon identification variables: Track Matching δx, Isolation $E_T(0.4)$, Minimum Ionizing (EM and Hadronic), and the Cosmic Ray Filter, we use the general scheme described above. The Z sample is essentially re-made starting from the primary muon sample, without requiring the second leg to pass the cut of interest. In the case of the track matching δx cuts, we require the second leg to fall into the fiducial region for the particular detector (either CMU or CMP). For the cosmic ray filter, we require the secondary leg to hit one of the muon chambers, as this filter is not defined for other muon candidates.

Table 5.1 lists the results of this study, with corresponding event counts (parameters defined above) and resulting efficiencies for each cut. Note that due to the differing nature of each cut, the event counts vary widely.

Cut	N_B , N_T	Efficiency, %
CMU $\lvert\delta x\rvert \leq 2.0\ cm$	138,150	$95.83^{+1.21}_{-1.56}$
CMP $\lvert\delta x\rvert \leq 5.0\ cm$	98,99	$99.49^{+0.42}_{-1.15}$
Hadronic Energy $\leq 6.0\ GeV$	412,424	$98.56^{+0.41}_{-0.54}$
EM Energy $\leq 2.0\ GeV$	403,424	$97.46^{+0.56}_{-0.68}$
$E_T(0.4) \leq 2.0\ GeV$	390,423	$95.94^{+0.71}_{-0.83}$
Cosmic Ray Filter	290,291	$99.83^{+0.14}_{-0.39}$

Table 5.1: Basic Muon Identification Efficiencies

5.3 Trigger Efficiencies

The Level 1, 2, and 3 trigger efficiencies can be computed in a like manner with the same $Z \rightarrow \mu\mu$ sample, using the same probability argument. One caveat is that we reconstruct the trigger decision for the two legs of the Z decay, whereas the overall trigger decision could have come from either leg or a trigger from anything else in the event. Explicitly requiring the inclusive muon triggers to pass at all levels eliminates most volunteer (non-inclusive muon) triggers. From the raw trigger data banks, we reconstruct the decision of the trigger individually for both legs of the Z decay, as well as the single leg of the W decay. We require the online trigger to have originated from at least one of the identified muon candidates in both the W and Z data samples. This additional requirement removes 10 events due to Level 2 and 3 events due to Level 1 from the W sample. No further Z candidates are removed.

5.3.1 Level 1 Efficiency

For the Level 1 efficiency calculation, we require both muons from the $Z \to \mu\mu$ decay to fall in the central, fiducial, triggerable region. Following the double probability correction, we obtain an efficiency of:

$$\epsilon_{L1} = 95.47^{+1.27}_{-1.61}$$

We note that the CMP trigger was responsible for only two of the second leg failures listed in table 5.3 . Therefore, we do not factor out the relative CMP acceptance and efficiencies here, instead we simply compute the net Level 1 efficiency.

5.3.2 Level 2 Efficiency

The Level 2 trigger efficiency is completely determined by the hardware track processor, the CFT. As described previously, the CFT receives two sets of hit information from the central tracking chamber, prompt and delayed. Only axial wire layers are used. The prompt and delayed hits are applied to look-up tables to recognize tracks. The CFT recognizes tracks in eight bins by P_T, numbered 0 to 7. The inclusive muon trigger requires the CFT track to be of at least bin 4, corresponding to a nominal $P_T \sim 10.0\ GeV$ used in the pattern recognition look up tables. Monte Carlo analysis yields a ninety percent efficiency point of $\epsilon_{90\%} \sim 9.2\ GeV$ for this P_T bin.

After the CFT identifies a list of tracks, the level 2 trigger matches them to the muon chamber trigger hits from the level 1 trigger. The matching requirement is very loose, and has been determined not to incur any additional inefficiency. The CFT track must project from the tracking chamber to the appropriate muon chamber, within a range of 5 to 15 degrees in phi (depending on run, position and momentum of track).

We can use the $Z \to \mu\mu$ sample to compute the CFT efficiency. The triggering scheme is reconstructed from the list of tracks found originally by the CFT while in operation (recorded in the data stream). Counting double passes and using the same probability argument, we obtain:

$$\epsilon_{L2} = 92.10^{+1.68}_{-1.97}\%$$

The loss in efficiency due to the CFT can be traced back to the high voltage settings on the central tracking chamber. For the entire data run the voltages were lowered below the nominal CFT design specifications. (The chamber voltages were lowered for reasons relating to dE/dx measurements, which are not used here.) With lower voltages, prompt hits are sometimes lost, causing the track not to be identified.

With the low efficiency, the Poisson error on the Level 2 efficiency would dominate the trigger efficiency uncertainty. Instead, we search for an independent method of determining the CFT efficiency to improve accuracy. The $W \rightarrow e\nu$ sample does not necessarily require any tracking triggers or tracking information, and provides a statistically larger data sample. This sample can be created purely by identifying electrons in the calorimeter, creating a W "no track" sample. The triggers involved in this special sample only require electromagnetic energy deposition and missing transverse energy (calorimeter only).

Fortunately, in addition to the $W \rightarrow e\nu$ missing transverse energy trigger, we also have an inclusive Level 2 trigger requiring a CFT track match to an EM cluster (similar to the CFT / muon chamber matching) with a CFT trigger threshold of bin 4, identical to the inclusive muon trigger. We compute the CFT efficiency from the W "no track" sample, looking in the sample to determine whether the CFT hardware found a track where it should have. We factor out any effects due to the calorimeter trigger efficiency, and use identical kinematic cuts in both samples.

The caveats in using the electron sample to measure a muon efficiency are obvious: Electrons are far more likely to bremsstrahlung in the tracking volume; the muon coverage in η is more restrictive than the electron. Figure 5.1 (left) plots CFT efficiency vs. detector η, which is clearly not constant. We restrict our nominal range to $0.03 \leq |\eta| \leq 0.6$ when computing the efficiency to match the muon coverage.

To measure the effect of bremsstrahlung, we plot the CFT efficiency as a function of E/p in figure 5.1 (right), where E is the energy measured in the calorimeter and p is the momentum measured in the tracking chamber. Considering only resolution, the E/p distribution for electrons should be Gaussian; adding bremsstrahlung will create a tail at high E/p. To isolate the effect of bremsstrahlung, we restrict the nominal region to $0.9 \leq E/p \leq 1.1$. To estimate the systematic effect of differences between electrons and muons, we compute the efficiency for the control regions $E/p \geq 1$ and $E/p \leq 1$. The spread in these measurements is taken as the systematic error. Table 5.2 summarizes the results of the CFT study. The N_G values are defined as the number of events where a CFT

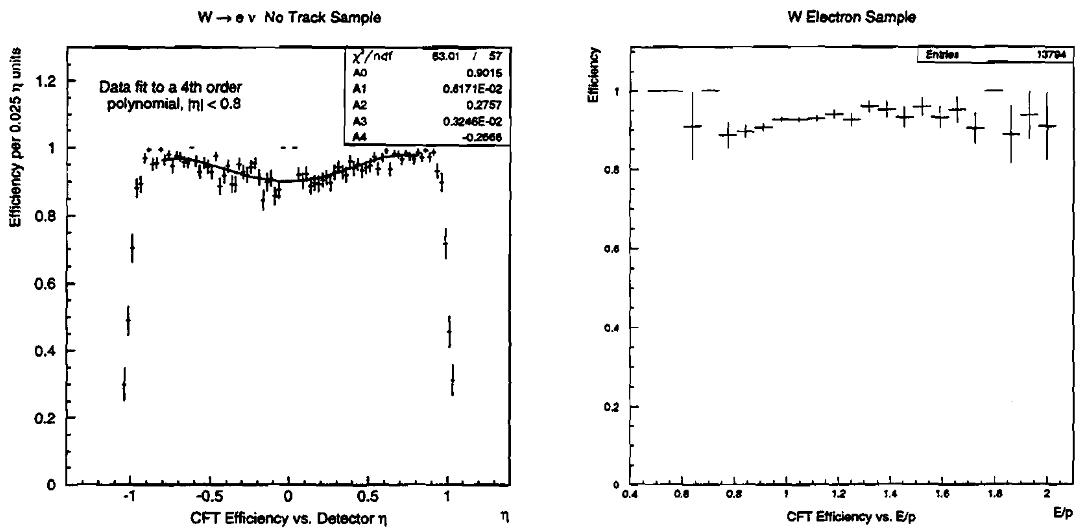

Figure 5.1: $W \rightarrow e\nu$ CFT Efficiencies

track was found, taken from N_T, the total number of events in the control sample. Note that the two results are consistent; we take the $W \rightarrow e\nu$ measurement as nominal.

Region	N_G , N_T	Efficiency, %
$E/p \leq 1.0$	2605,2843	$91.63^{+0.52}_{-0.55}$
$0.9 \leq E/p \leq 1.1$	4172,4518	$92.34^{+0.40}_{-0.42}$
$E/p \geq 1.0$	4025,4321	$93.15^{+0.39}_{-0.41}$
CFT Efficiency, $W \rightarrow e\nu$	$92.34 \pm 0.42(stat) \pm 0.76(syst)$	
CFT Efficiency, $Z \rightarrow \mu\nu$	$92.10^{+1.68}_{-1.97}$	

Table 5.2: Level 2 Trigger Studies

5.3.3 Level 3 Efficiency

Level 3 tracking and muon reconstruction efficiency determines the Level 3 efficiency. Level 3 software mimics offline reconstruction, although the constraints on the muon objects are substantially looser at Level 3. All results of the Level 3 reconstruction are kept in the event record, and we can reconstruct the Level 3 decision based on this information for both legs of the Z sample.

We again restrict both legs of the Z decay to fall within the fiducial, triggerable region of the detector. Table 5.3 lists the results of this study. All of the Level 3 failures were found to be due to the failure of Level 3 tracking to find the muon track in the central tracking chamber.

5.3.4 *Combined Trigger Efficiency*

Using the individual level efficiencies described in the previous subsections, we combined them to form the net trigger efficiency T :

$$T = \epsilon_{L1} \cdot \epsilon_{L2} \cdot \epsilon_{L3}$$

Table 5.3 tabulates the results.

Trigger	N_B , N_T	Efficiency, %
Level 1	137,150	$95.47^{+1.27}_{-1.61}$
Level 2	4172,4518	$92.34^{+0.86}_{-0.87}$
Level 3	106,109	$98.60^{+0.77}_{-1.34}$
Combined Trigger Efficiency, T	$86.92^{+1.56}_{-2.05}$	

Table 5.3: Trigger Efficiencies

5.4 Detector Efficiencies

Detector efficiencies describe the net efficiency of a chamber to register the hits emanating from the muon as it passes near the drift wires, as well as the offline software to recognize those hits and form them into tracks. We factor the total detector efficiency into two independent terms: one for the muon chambers and the second for the the central tracking and vertexing chambers.

5.4.1 *Tracking Efficiencies*

Tracking efficiency combines several effects into one efficiency: Tracking pattern recognition; central tracking chamber efficiency; event vertex recognition algorithm; and vertex chamber efficiency. The chamber efficiencies we expect to be very high due to the high degree of redundancy of wire channels in each detector per single track and due to the high degree of isolation of muon tracks in W and Z decay events.

However, for W and Z muonic decays, we rely on the pattern recognition software to indicate the presence of a muon and therefore cannot use the Z candidates to measure this efficiency. I.e., events with failures in tracking efficiency on one leg of the Z decay will not be seen in the Z sample. Instead, we use the special $W \rightarrow e\nu$ candidate sample with no tracking requirements placed on it to measure the tracking and vertexing efficiencies [67]. Out of a sample of 6871 events, 6848 events successfully found a track and vertex. Of these, 17 were vertexing failures and 8 were tracking failures. The resulting efficiency is very high: $\epsilon = 99.67^{+0.06}_{-0.07}(stat)\%$. None of the failures were obviously due to bremsstrahlung, a potential source of systematic deviation between electrons and muons. The effect of bremsstrahlung in the electron sample would only make the tracking efficiency worse: If the electron emits a photon en route through the tracking chamber, a kink in the electron path will occur, thus degrading tracking efficiency. Therefore, the muon sample would only be *more* efficient.

Considering this effect and the high value of the tracking efficiency, we take the systematic error to be the range up to full efficiency: $\epsilon = 99.67 \pm 0.33\%$. The result is listed in table 5.4. Note that the definition of N_B and N_T are different for this efficiency – we simply have $\epsilon = N_B/N_T$ for the efficiency, as in the Level 2 efficiency.

5.4.2 Muon Chamber Efficiencies

Similarly, the muon chambers incur some loss of efficiency. We expect the muon chamber to be less efficient, since typically only four wires in the four muon chamber layers are available to reconstruct a track stub. We define the muon chamber efficiency ($\epsilon_{chamber}$ or ϵ_c) as the probability that the muon will produce enough hits of sufficient quality in the chambers in order to reconstruct a muon track stub offline. This value includes muon chamber combined hit efficiency as well as offline pattern recognition efficiency.

For the calculations we again use the Z sample. We require both muon legs to be in the fiducial chamber volume, either CMU or CMP (separately, where required), with no muon chamber restrictions or requirements on the secondary muon. Only the central tracking information is used here to determine if the muon points to the fiducial muon chamber volumes; if the muon points to the fiducial region, it should produce a muon chamber track stub there. With this specially selected data set, we then look and see if a muon stub was actually reconstructed. The efficiency can then be computed in the usual dimuon manner. The results are listed in table 5.4. We are hurt in statistics by the reduced acceptance of the CMP chambers; fortunately the CMP chamber efficiency is very high and so does not cause a large uncertainty.

Chamber	N_B , N_T	Efficiency, %
Central Muon Chamber	150,156	$98.04^{+0.79}_{-1.16}$
Central Muon Upgrade Chamber	68,69	$99.27^{+0.61}_{-1.65}$
Central Tracking/Vertexing	6848,6871	$99.67^{+0.33}_{-0.33}$

Table 5.4: Chamber Efficiencies

5.5 Combined Results

The individual cut efficiencies must be combined to produce net efficiencies of the W and Z samples. Table 5.5 lists various convenient combined efficiencies, as well as the final W and Z efficiencies and the ratio of efficiencies.

Combined Efficiency	Efficiency, %
Muon Matching, $\|\delta x\|$, $\epsilon_{\delta x}$	$95.48^{+1.24}_{-1.75}$
Minimum Ionizing, $\epsilon_{m.i.}$	$96.06^{+0.68}_{-0.85}$
Isolation: $E_T(0.4)$	$95.94^{+0.71}_{-0.83}$
Cosmic Ray Filter	$99.83^{+0.14}_{-0.39}$
Muon Chamber Efficiency, ϵ_c	$97.52^{+0.90}_{-1.64}$
Tracking and Vertexing	$99.67^{+0.33}_{-0.33}$
Combined Primary Muon: ϵ_p	$85.38^{+1.62}_{-2.39}$
Combined Secondary Muon: ϵ_s	$95.74^{+0.68}_{-0.85}$
Combined Trigger, T	$86.92^{+1.57}_{-2.05}$
Fiducial,Fiducial Z Efficiency: ϵ_1	$88.58^{+1.27}_{-1.63}$
Fiducial,Non-Fiducial Z Efficiency: ϵ_2	$70.91^{+1.93}_{-2.68}$
Combined Z Efficiency, ϵ_Z	$74.50^{+2.15}_{-2.97}$
Combined W Efficiency, ϵ_W	$74.21^{+1.94}_{-2.72}$
Efficiency Ratio: ϵ_Z/ϵ_W	$1.0038^{+0.0120}_{-0.0156}$

Table 5.5: Combined Efficiencies

5.5.1 *Combined Muon Identification Efficiencies*

There are two CMP related efficiencies: Chamber efficiency and track matching (CMP $|\delta x|$) . As stated earlier, the goal of the soft CMP requirements is to minimize the additional inefficiency incurred by the CMP cuts, and indeed the above calculations have shown that the cuts are almost 100 % efficient. The CMP chambers do not cover all of the CMU chamber acceptance, so we must fold in the CMP efficiencies according to the relative geometric coverage in order to obtain the net muon chamber efficiency.

The two parameters α and β represent the relative coverage of the CMP. We define α to be the acceptance of the CMU chambers covered by the CMP divided by the total acceptance. We define β to be the complement: the acceptance of the CMU chambers not covered by the CMP divided by the total acceptance. The chamber and $|\delta x|$ efficiencies combine as:

$$\epsilon_{net} = \epsilon_{CMU} \cdot (\alpha \cdot \epsilon_{CMP} + \beta)$$

To obtain these geometric factors we run the W acceptance Monte Carlo (described in the previous chapter) without a $\not{E}_T$ requirement. Without this cut, we remove underlying event biases and obtain obtain a purely geometric factor. The α and β factors are ratios of acceptances and so we neglect systematic errors. The Z sample double counting corrections (described below) should not be affected in light of the high efficiency of the CMP cuts. The values obtained are $\alpha = 0.7216$ and $\beta = (1 - \alpha) = 0.2784$. Note that the CMU chambers that are partially covered by CMP are treated in the same manner as in the acceptance Monte Carlos and as pictured in figure 4.1.

5.5.2 *Combining W,Z and R_μ Efficiencies*

We have used two separate sets of muon cuts in this analysis: Primary and Secondary. Each W or Z candidate must have at least one primary muon. The primary muon efficiency is determined by the product of all the constituent cut efficiencies:

$$\epsilon_p = \epsilon_{\delta x} \cdot \epsilon_{isolation} \cdot \epsilon_{CRF} \cdot \epsilon_{m.i.} \cdot \epsilon_{chamber} \cdot \epsilon_{tracking}$$

For W candidates, we require that the trigger be satisfied and the muon pass all the primary cuts. The W efficiency is simply:

$$\epsilon_W = T \cdot \epsilon_p$$

We have taken the simple product as the net efficiency. There are small correlations between the different efficiencies; for example, the isolation and minimum ionizing cuts are correlated. We have attempted to minimize the effect of the correlation by requiring the secondary muon in the Z candidates to pass all of the remaining cuts. The cut efficiencies computed in this manner are all very efficient – individually they are all at least 95%. Therefore we take any possible correlation effects as negligible and simply take the product of all efficiencies as the net efficiency. The tracking efficiency is potentially the most correlated to all of the cut efficiencies and to the trigger efficiencies as well. However, since we have found the tracking efficiency to be nearly 100%, we can safely neglect tracking efficiency correlations.

The secondary muon cuts are much less restrictive. Only a track and a minimum ionization signal in the calorimeter are required for a secondary muon:

$$\epsilon_s = \epsilon_{m.i.} \cdot \epsilon_{tracking}$$

The secondary muon classes listed in table 3.5 indicate a significant number of Z candidates had corresponding hits in the muon chambers. However, we make no cuts on the quantities involving muon chamber hits, and therefore do not incur inefficiencies on the second leg of the Z decay due to the muon chambers.

In the chapter on acceptances, $f_{\mu\mu}$ is defined as the fraction of the total Z acceptance in which both muons land in the primary fiducial muon region. When both muons point to the primary fiducial region, there is a double chance for the event to pass the primary cuts and the trigger, but only if the muon chambers are efficient for both muons. If a muon encounters a chamber inefficiency, then it will not have an opportunity to pass either the trigger or the gold muon cuts. Therefore, within the $f_{\mu\mu}$ acceptance region, we the have two cases: (1) Muon chambers efficient for both muons and (2) muon chambers inefficient for one of the muons.

In the $f_{\mu\mu}$ region, when both muons are chamber efficient (denoting ϵ_c as the muon chamber efficiency), there are four cases:

ϵ_p^2	Probability that both muons pass the primary cuts

$\epsilon_p \cdot (\epsilon_s \cdot \epsilon_c - \epsilon_p)$	Probability μ_1 passes primary, μ_2 only passes secondary cuts
$(\epsilon_s \cdot \epsilon_c - \epsilon_p) \cdot \epsilon_p$	Probability μ_1 passes only secondary cuts, μ_2 only passes primary
$(\epsilon_s \cdot \epsilon_c)^2$	Probability both muons pass only secondary cuts (Not Observed)

For this case grouping, we take the muon chambers to be efficient for both the first and second muons. However, the secondary muon must pass at least the secondary muon cuts or the event will not be observed. For the case that the second muon fails one of the δx, *isolation*, or *CRF* cuts, the efficiency is: $\epsilon_s \epsilon_c \cdot (1 - \epsilon_{\delta x} \epsilon_{iso} \epsilon_{CRF}) = (\epsilon_s \cdot \epsilon_c - \epsilon_p)$, as noted above. Since both muons have muon chamber track stubs in this case grouping, both muons have a chance to pass the trigger:

T^2	Probability that both muons pass trigger
$T \cdot (1 - T)$	Probability μ_1 passes trigger, μ_2 fails trigger
$(1 - T) \cdot T$	Probability μ_1 fails trigger, μ_2 passes trigger
$(1 - T)^2$	Probability both muons fail trigger (Not Observed)

Multiplying out the two sets of probabilities and summing all the cases, we have, for muons in the $f_{\mu\mu}$ region, with no chamber inefficiency, a net efficiency of:

$$\epsilon_p \cdot T \cdot (2\epsilon_s \epsilon_c - \epsilon_p) \cdot (2 - T)$$

For the complementary case grouping with chamber inefficiency in the secondary muon, we then only have the following three probability cases:

$\epsilon_p \cdot \epsilon_s \cdot (1 - \epsilon_c)$	Probability μ_1 passes primary, μ_2 only passes secondary
$\epsilon_s \cdot (1 - \epsilon_c) \cdot \epsilon_p$	Probability μ_2 passes primary, μ_1 only passes secondary
$(\epsilon_s \cdot (1 - \epsilon_c))^2$	Probability both muons pass only secondary cuts (Not Observed)

Since one of the muons is chamber-inefficient, there is only one chance for the event to pass the trigger, so the net efficiency in this case is:

$$2\epsilon_p \cdot (1 - \epsilon_c) \cdot \epsilon_s \cdot T$$

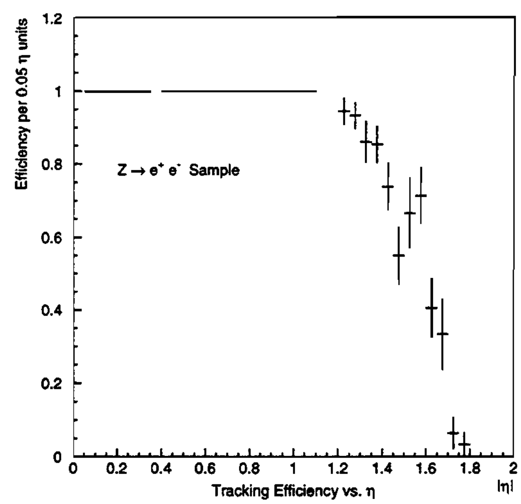

Figure 5.2: Tracking Efficiency vs. Pseudorapidity

The chamber efficiency ϵ_c is poorly know; fortunately it partially cancels in the sum of the two case groupings. Combining the two terms, the total efficiency in the $f_{\mu\mu}$ region is:

$$\epsilon_1 = \epsilon_p \cdot T \cdot (2\epsilon_s \cdot (1 + \epsilon_c - T \cdot \epsilon_c) - (2 - T) \cdot \epsilon_p)$$

In the case where one muon falls into the central, primary fiducial region and the other muon falls outside that region, the efficiency is much simpler. We denote this efficiency by ϵ_2. However, we must apply a small correction factor due to the drop off in tracking efficiency near the edge of the acceptance at $\eta = 1.2$. Figure 5.2 plots the tracking efficiency as a function of detector η from the $Z \to ee$ sample. This sample is initially created by making no tracking requirements on the secondary leg – only calorimeter information is used for the second leg. The efficiency is then calculated by looking to see whether the second leg had an associated track.

We see that the efficiency is flat out to $\eta = 1.1$ and then begins to drop off. The efficiency is not directly available in the $1.1 \leq \eta \leq 1.2$ bin, so we interpolate to obtain: $\epsilon_\eta = 96.98 \pm 3.02\%$ (implicitly we normalize to the centrally measured tracking efficiency). The fraction of ϵ_2 regional acceptance represented by the $1.1 \leq \eta \leq 1.2$ bin is $f_\eta = 6.92\%$, so the efficiency reduction term is $\Delta\epsilon_\eta = (1 - \epsilon_\eta) \cdot f_\eta = 0.209 \pm 0.202\%$. Adding this correction we obtain:

$$\epsilon_2 = \epsilon_p \cdot \epsilon_s \cdot T \cdot (1 - \Delta\epsilon_\eta)$$

We weight ϵ_1 by the fraction $f_{\mu\mu}$ and the complementary region by $(1 - f_{\mu\mu})$. The total Z efficiency is then:

$$\epsilon_Z = f_{\mu\mu} \cdot \epsilon_1 + (1 - f_{\mu\mu}) \cdot \epsilon_2$$

$$\epsilon_Z = \epsilon_p \cdot T \cdot [f_{\mu\mu} \cdot (2\epsilon_s \cdot (1 + \epsilon_c - \epsilon_c \cdot T) - (2 - T) \cdot \epsilon_p) + (1 - f) \cdot \epsilon_s \cdot (1 - \Delta\epsilon_\eta)]$$

Note that when we take the ratio ϵ_Z/ϵ_W, then primary and trigger terms cancel:

$$\frac{\epsilon_Z}{\epsilon_W} = f_{\mu\mu} \cdot (2\epsilon_s \cdot (1 + \epsilon_c - \epsilon_c \cdot T) - (2 - T) \cdot \epsilon_p)) + (1 - f_{\mu\mu}) \cdot \epsilon_s \cdot (1 - \Delta\epsilon_\eta)$$

This ratio is used when calculating the final value for the cross section ratio, R_μ. All results are listed in table 5.5.

Chapter 6

Backgrounds to W and Z Production

The dominant source of High P_T, isolated muons is the muonic decay of W and Z bosons. However, a number of processes fake the production of W and Z bosons and all contributions must be estimated and subtracted from the number of candidate events in order to accurately measure the cross sections. This chapter separately considers the backgrounds to the W and Z candidate samples.

6.1 W Backgrounds

The contributions to W background divide up into several classes: General QCD processes; $Z \rightarrow \mu\mu$ production where one muon is lost; Cosmic Rays; and W or Z decays into τ leptons, where the τ decays into a muon. The total of all backgrounds will be listed in table 6.3 following discussion of both W and Z backgrounds.

6.1.1 General QCD Backgrounds to $W \rightarrow \mu\nu$

The leading sources of general QCD backgrounds we ascribe to the following processes:

$b \rightarrow \mu + X$

$\pi \rightarrow \mu + X$: Decay in Flight

π fakes μ : Punch Through

$c \rightarrow \mu + X$

The heavy quark decays can fake $W \rightarrow \mu\nu$ if the opposing jet(s) fall completely or partially into cracks or are simply mismeasured in the calorimeter, thus producing spuriously large $\not{E}_T$ in addition to "real" $\not{E}_T$ from neutrinos. Other processes involving lower mass quarks should be negligible with our $P_T \geq 20\ GeV$ cut.

The method for estimating the background for this class of processes relies on assuming the fluctuations involved in producing the fake $\not{E}_T$ are not correlated with the isolation of the identified muon. We re-create the W sample without applying isolation or $\not{E}_T$ cuts, while removing events from our Z candidate list. We then divide the ($\not{E}_T$, $E_T(0.4)$) plane into four sections, defined in table 6.1. Table 6.1 also indicates the event counts in each of the four regions for this sample.

$E_T(0.4) \geq 6\ GeV$ $\not{E}_T \leq 10\ GeV$ **B** *1178 Events*		$E_T(0.4) \geq 6\ GeV$ $\not{E}_T \geq 20 GeV$ **C** *222 Events*
$E_T(0.4) \leq 2\ GeV$ $\not{E}_T \leq 10\ GeV$ **A** *669 Events*		$E_T(0.4) \leq 2\ GeV$ $\not{E}_T \geq 20 GeV$ **W** *6222 Events*

Table 6.1: Regions in the $\not{E}_T$ vs. $E_T(0.4)$ Plane

The signal region in this plane is marked as W at high $\not{E}_T$ and low $E_T(0.4)$. Assuming the control regions A, B, and C have negligible contamination and the $\not{E}_T$ and $E_T(0.4)$ are uncorrelated for the background processes, we can use the event counts in regions A and B to measure the relative fraction of low $E_T(0.4)$ to high $E_T(0.4)$ of background processes. With this fraction, we can use the event count in C as background normalization to the high $\not{E}_T$ region. Background in the W signal region can then be computed as:

$$N_{QCD\ Background} = \frac{A}{B} \cdot C$$

See figure 6.1 for a scatter plot of $\not{E}_T$ vs. $E_T(0.4)$ used in the background calculation. The assumptions listed above are not quite accurate, since we do expect some W contamination in the control areas, since the W $\not{E}_T$ spectrum does not fall to zero below $\not{E}_T$ of 10 GeV and the $E_T(0.4)$ is not completely efficient above $E_T(0.4)$ of 6 GeV. To study systematic effects related to these effects, we repeat the background calculation on the same sample with additional requirements:

1. Nominal sample has no jet requirements
2. Jet with $E_T \geq 10\ GeV$
3. Jet with $E_T \geq 20\ GeV$

where the jet clustering algorithm uses an identification cone of $\Delta R \leq 0.7$. We repeat the background computation in these special jet samples in both the primary and inclusive muon data sets (see chapter 3 for the definition of primary and inclusive muon candidates). We expect the W contamination in the control areas to be smaller when requiring a jet. Figure 6.2 indicates the average isolation parameter as a function of missing transverse energy for the three different samples. Note the turn-on of the W signal at and below $\not{E}_T \sim 20\ GeV$. Below the point $\not{E}_T \sim 10\ GeV$ we expect the contamination of W events in the background control region to be minimal, and the average isolation should be nearly constant. For the sample without jet requirements, below 10 GeV we see a small dependence of $\not{E}_T$ with $E_T(0.4)$. Requiring jets reduces this dependence; in the sample requiring a jet of at least 20 GeV, we see this region is quite flat.

However, computations requiring jets will systematically underestimate the background in the W signal region: we expect real background to have associated jets, but the background in the W signal region will in general have these jets mismeasured. We take the the spread in the several background calculations as the systematic error to this measurement; we take the sample without jet requirements as the nominal background computation and obtain:

$$N_{QCD\ Background} = 126.1 \pm 58.2 \quad (spread)$$

Table 6.2 lists all the calculations and the resulting errors. The error on the individual measurements is statistical only. In that our model here may not be accurate for the above mentioned reasons, we consider an alternate method in the following subsection to obtain the total error on this background estimate, Δ.

Sample	Primary $\|\delta x\|$	Inclusive $\|\delta x\|$
No Jet Requirement	126.1 ± 10.4	166.9 ± 12.5
1 Jet, $E_T \geq 10\ GeV$	111.2 ± 9.4	148.1 ± 11.3
1 Jet, $E_T \geq 20\ GeV$	50.4 ± 5.1	64.9 ± 6.1
Sample Spread (δ), Total Error (Δ)	$\delta = 58.2$	$\Delta = 63.3$

Table 6.2: $W \rightarrow \mu\nu$ General QCD Backgrounds

6.1.2 Modelling QCD Backgrounds

To gain confidence in our value for the background from generic QCD processes, we consider an alternate method for determining this background from the shape of the missing E_T distribution. Throughout the following subsection, we use the $W \rightarrow \mu\nu$ candidate data sample, before the missing transverse energy cut has been applied but including the isolation requirement. The points in figure 6.3 (right) indicate the missing transverse energy distribution for this sample, with the cut position indicated.

We model the missing transverse energy distribution for the QCD background by employing the $b \rightarrow \mu + X$ Monte Carlo described at the end of chapter 3. The resulting simulated missing transverse energy distribution is plotted in figure 6.3 (left). Overlayed is a functional fit to the distribution of somewhat arbitrary form. We take this distribution as being representative of other QCD background processes. As mentioned in chapter 3, we expect $b \rightarrow \mu + X$ to be a significant fraction of the inclusive non-W, Z high P_T muon events; in the same chapter we have seen very similar muon P_T distributions between $b \rightarrow \mu + X$ and a pion/punchthrough model. We therefore expect b decays to reasonably reflect the missing E_T distribution of the overall generic QCD background.

The data points in figure 6.3 (right) exhibit a distinct double peaked distribution, strongly indicating two very different physics processes. In the dot-dashed line we overlay the Monte Carlo distribution for the $b \rightarrow \mu + X$ as our QCD model; this distribution peaks near 5 GeV. The dashed line indicates the Monte Carlo prediction for the $W \rightarrow \mu\nu$ process as predicted by the generator and detector simulation described in chapter 4; this distribution peaks far above at around 38 GeV. Alone, these two very different predictions can qualitatively explain the structure of the distribution.

To determine the QCD fraction in the W signal region, we must find the relative normalization between the QCD and non-QCD distributions. For the overall non-QCD contribution to the distribution, we include distributions from the two other dominant background sources: $Z \rightarrow \mu\mu$ (one μ lost) and $W \rightarrow \tau \rightarrow \mu + X$. Both $\not{E}_T$ distributions are shown by dotted lines in figure 6.3; other small contributions are neglected here. We fix the fractions for these two processes according to the numbers determined in the following subsections, relative to the normalization of the $W \rightarrow \mu\nu$ distribution. The non-QCD distribution is thus a combination of three processes, all of which peak at high $\not{E}_T$.

The relative normalization between the non-QCD and QCD distributions is then allowed to float; the overall normalization is given by the area under the data points. In figure 6.3, we display the resulting fit as a solid line. The fit gives $\chi^2/n = 1.65$, which is reasonable but not optimal and almost certainly due to the imperfect modelling of the background; note especially that pion decays-in-flight have not been considered here, and may yield a different $\not{E}_T$ spectrum.

With the relative normalization in hand, we can extract the QCD background in the W signal region (above $\not{E}_T \geq 20\ GeV$) by integrating the functional form of the QCD background from $20 \leq \not{E}_T < \infty$. This method yields a background of:

$$N_{QCD\ Background} = 101.1 \pm 31.3 \quad (fit\ method)$$

where the error quoted here is from the fit only. We note that this answer agrees with the nominal result above, but perhaps may underestimate the total background. We take the difference between this result and the previous result as an additional systematic error and add it in quadrature with the spread error, δ from table 6.2 to yield a nominal value with total error:

$$N_{QCD\ Background} = 126.1 \pm 63.3 \quad (total\ error)$$

where the total error is given as Δ in the same table.

6.1.3 $Z \rightarrow \mu\mu$ Lost Muon W Backgrounds

The $Z \rightarrow \mu\mu$ process, where one of the muons is lost and the event then passes the W candidate $\not{E}_T$ cut forms the dominant source of background in the W sample. We consider here two cases: (1) the secondary muon is lost due to geometric factors – the muon falls beyond the acceptance of the detector; (2) the secondary muon is lost due to in inefficiency in either the identification cuts or the chambers.

For the geometric case, in the previous chapter we have carefully computed the acceptance for the muons lost due to geometry in a manner consistent with the overall W and Z acceptances. The factor we use is the "Z fake W" acceptance, $A_{Z,W}$, normalized to the Z acceptance, A_Z. The number of background events in this category is then computed by taking the observed number of Z candidate and correcting for both the relative acceptance and the relative efficiencies of W and Z.

$$N_{Z\ Lost\ \mu} = \frac{N_Z}{A_Z \cdot \epsilon_Z} \cdot A_{Z,W} \cdot \epsilon_W = N_Z \cdot \frac{A_{Z,W}}{A_Z} \cdot \frac{\epsilon_W}{\epsilon_Z}$$

The term $N_Z/(A_Z \cdot \epsilon_Z)$ is the total expected number of Z bosons produced during the run. The total Z events are subsequently corrected by multiplying the acceptance and efficiency for these types of events, $A_{Z,W} \cdot \epsilon_W$. Using the measured, normalized Z total reduces any theoretical bias that may come from using a predicted Z cross section. We can re-arrange terms above such that systematic uncertainty comes from the acceptance ratio $A_{Z,W}/A_Z$ documented in the previous chapter, and the efficiency ratio. The statistical error is taken from the Z count, yielding:

$$N_{Z\ Lost\ \mu} = 372.4 \pm 18.1(stat) \pm 11.9(syst)$$

The second leg of the Z may also be lost due to inefficiencies in passing the secondary cuts. This background can be expressed as:

$$N_{Z\ Lost\ \mu,\ Ineff} = (1 - \epsilon_s \cdot \epsilon_c) \cdot N_{Z1} + (1 - \epsilon_s) \cdot N_{Z2}$$

Where N_{Z1} is the number of "fiducial, fiducial" Z candidates; N_{Z2} is the number of "fiducial, non-fiducial" Z candidates. Using event counts and efficiencies defined in previous chapters, we obtain:

$$N_{Z\ Lost\ \mu,Ineff} = 21.5 \pm 3.7$$

6.1.4 Cosmic Ray Background

The cosmic ray filter, when applied to the data sample does not remove all cosmic rays. To estimate the fraction of W candidates which remain cosmic rays, we apply the cosmic ray removal algorithm to a subset of isolated muons; the events that are not flagged as cosmic rays are scanned by hand. Residual cosmic rays were identified by quality cuts on the vertex and muon chamber data as well as a search for muon chamber hits in the opposite phi region. The study yields a failure contamination rate of $(0.4 \pm 0.2)\%$. The error is primarily due to the inability to definitively identify some marginal failures. (See chapter 3 for a description of the cosmic ray filter.)

6.1.5 $W \rightarrow \tau\nu$ and $Z \rightarrow \tau\tau$ Backgrounds

To estimate the tau backgrounds in the W sample, we use IsaJet [62] to generate $W \rightarrow \tau\nu \rightarrow \mu + X$ and $Z \rightarrow \tau\tau \rightarrow \mu + X$ sequential decays. The acceptance for these type of events is substantially smaller than for direct $W \rightarrow \mu\nu$ decays due to the presence of the extra event neutrinos carrying away a larger fraction of the transverse momentum. The $Z \rightarrow \tau\tau$ decays are additionally complicated by the other tau, which can decay either hadronically or leptonically, and thus balance out the $\not{E}_T$ of the muonic decay. Due to these complications, we use the IsaJet rather than our own simple generator.

The IsaJet generator is used in a consistent manner with the previous acceptance calculations, with the $MRS\ D'_-$ parton distribution function and the nominal W and Z masses. The muon fiducial requirements are also identical to those previously described. For the $Z \rightarrow \tau\tau$ case, we take the resulting acceptance and use the measured number of Z candidates to obtain this background. We must also correct for relative W and Z efficiencies:

$$N_{Z\tau} = \frac{N_Z}{A_Z \cdot \epsilon_Z} \cdot A_{Z\tau} \cdot \epsilon_W = \frac{A_{Z\tau}}{A_Z} \cdot \frac{\epsilon_W}{\epsilon_Z} \cdot N_Z$$

The acceptance for $Z \rightarrow \tau\tau \rightarrow \mu + X$ is $A_{Z\tau} = 0.521 \pm 0.261\%$, and taking the efficiencies and event counts from previous chapters, we obtain a yield of:

$$N_{Z\tau} = 13.7 \pm 6.9$$

For $W \rightarrow \tau\nu \rightarrow \mu + X$, we use the measured number of W signal events to normalize the background. All other backgrounds to this point have been independent of the number of W signal events, so we subtract out all other backgrounds from the number of W candidate events. Where N_W is the number of signal W events, this background is:

$$N_{W_\tau} = \frac{A_{W_\tau}}{A_W} \cdot N_W$$

With the acceptance for this background, $A_{W_\tau} = 0.648 \pm 0.052\%$, and with all other sources of background removed, we have:

$$N_W + N_{W_\tau} = N_W + \frac{A_{W_\tau}}{A_W} \cdot N_W$$

Which yields a $W \to \tau\nu \to \mu + X$ background of:

$$N_{W_\tau} = 216.3 \pm 17.5$$

Both tau decay backgrounds are listed separately in table 6.3 .

6.1.6 *Top Quark Production as potential W Background*

A heavy top quark, with $M_t > M_W + M_b$, decays into a real W which can subsequently decay into a muon and neutrino; we consider top quark production to be a potential background to the W cross section, but do not include it in the W background calculation. Instead, we consider top production as an uncertainty to the background by computing the expected number of events based on the most recent 95% confidence level top limit:

$$M_{top} > 131\ GeV \quad 95\%\ C.L. \quad [69]$$

We compute the acceptance of top faking direct W production using the IsaJet [62] Monte Carlo generator with $M_{top} = 131\ GeV$, plus a fast detector simulation. The event yield is then estimated from the predicted top cross section at the same mass from reference [70], and comes to 18.9 events. We then have:

$$B_{top} = 0.0^{+18.9}_{-0.0}$$

In using the 95% confidence level limit, we have a conservative limit on this uncertainty.

6.2 Z Backgrounds

In contrast to the W sample, the Z sample is virtually background free. The fact that both leptons are detected in the Z decay and the dimuon invariant mass can be reconstructed help a great deal to reduce the Z background. The background contributions to the Z sample are: cosmic rays, $Z \to \tau\tau \to \mu\mu$, and (potentially) general QCD processes. The process $\gamma \to \mu\mu$ can also be considered a background to Z production. These backgrounds are summarized in table 6.4.

6.2.1 Cosmic Ray Background to Z

For the cosmic ray background in the Z sample, note that we have used the identical cosmic ray filter, applied to the primary leg of the Z candidate. Therefore the filter has a chance to remove a cosmic ray based solely on a single muon, as in the W selection, so we estimate the same fraction of cosmic ray contamination in the Z sample, $(0.4 \pm 0.2)\%$. We are supported in this estimate by the observation that there is a single like-sign dimuon event in our Z invariant mass window, which is clearly a cosmic ray. Cosmic rays will tend to have a random distribution of sign; they will tend to be out of time with the $p\bar{p}$ crossing time and thus produce anomalous hit timing information in the central tracking chamber, making the track reconstruction unpredictable.

6.2.2 General QCD Background to Z

The potential generic QCD background to the Z sample can be identified as coming from the same sources as in the W sample. In the Z case there must be two muons or muon fakes in the event, so combinatorics will strongly suppress such events. Real dimuon events from J/ψ or Υ production will be suppressed by the invariant mass cut.

In order to estimate the generic QCD process background in the Z sample, we attempt a similar method to the W QCD estimate. We re-create the Z sample without any isolation cut on either leg. We plot the isolation of the first leg (I_1) vs. the isolation of the second leg (I_2). The isolation plane (I_1,I_2) is then divided into four sections:

A. $I_1 \leq 2\ GeV$ and $I_2 \leq 2\ GeV$
B. $I_1 \leq 2\ GeV$ and $I_2 \geq 6\ GeV$
C. $I_1 \geq 6\ GeV$ and $I_2 \leq 2\ GeV$
D. $I_1 \geq 6\ GeV$ and $I_2 \geq 6\ GeV$

See figure 6.4 (left) for a scatterplot of the muon isolation variable $E_T(0.4)$ for the special Z sample without an isolation requirement on either leg. Shown on this plot are the isolation control regions as listed above. We can then count events in each region and extrapolate background fractions from high to low isolation:

$$\frac{D}{C} = \frac{B}{A}$$

However, there are no events in which both muon legs have isolation above 6 GeV, and the method breaks down. We take the lack of dimuon events with both legs not isolated as evidence for the absence of generic QCD background in the Z sample. In figure 6.4 (right) we also plot the dimuon invariant mass vs. the isolation variable for the second muon leg, from the standard dimuon sample (with the isolation requirement on the primary muon leg). Note that the population of non-isolated second muon legs is very sparse – we attribute these to the incomplete efficiency of the isolation cut.

As supporting evidence for zero QCD Z background, we note that there is only one like-charge dimuon event in the Z invariant mass window. We have attributed this event to being a cosmic ray with high confidence (see previous subsection). Eliminating the cosmic ray event, we have no remaining like-sign dimuon events in the Z signal region. We do not expect events with two pion decays or pion punchthroughs to be correlated in charge. Therefore, we take the QCD background in the Z sample as zero, with an upper error of 1 event.

6.2.3 $Z \to \tau\tau$ Background to Z

The process $Z \to \tau\tau \to \mu\mu$ is doubly suppressed by the $\tau \to \mu$ branching ratios. The presence of four neutrinos in the tau decays also substantially smears the invariant mass distribution, and our mass window cut removes most of these double muon decays. To estimate this background, we use the standard Z acceptance Monte Carlos, replacing the muons with taus decaying into muons and neutrinos and applying the usual mass cut. The acceptance is then normalized to the measured number of Z candidates with the measured tau branching ratios, yielding a tiny background of:

$$N_{Z\tau\tau} = 0.2^{+1.0}_{-0.2}$$

6.3 Drell Yan Correction to Z Cross Section

We wish to measure the Z production cross sections as indicated in figure 3.1, where the propagator is only the Z boson. However, the intermediate state can also be a photon; the total observed cross section is then given by the combination of the Z and γ intermediate states, plus the interference term between the two:

$$\sigma(q\bar{q} \to \mu\mu) \sim Z^2 + \gamma \cdot Z + \gamma^2$$

We compare our measured value to theory calculations that neglect the photon terms, so we consider the photon and interference contributions to be background. To correct for this background, we define the Drell-Yan correction as:

$$DY = \frac{\int_{66}^{116} Z^2 \; dM_{\mu\mu}}{\int_{66}^{116} (Z^2 + \gamma \cdot Z + \gamma^2) \; dM_{\mu\mu}} \quad (GeV)$$

The integrals are calculated over the nominal signal mass range, 66-116 GeV. The two processes have differing acceptances and mass spectra, and we must correct for that by examining the relative mass distributions of the two processes after they have been passed through the acceptance Monte Carlo. Figure 6.5 plots the predicted mass distributions after the detector Monte Carlo separately for $Z + \gamma$ (solid line) and Z *only* (dashed line). We have normalized the $Z + \gamma$ spectrum to the peak of the Z distribution, where the difference in cross sections should be negligible. This yields a correction factor of:

$$DY = 0.994 \pm 0.006$$

Note that the difference in the distributions is easily visible only in the log scale plot. The main contribution comes from the low mass region where the γ contribution begins to noticeably rise above the Z contribution with decreasing mass – although still a small effect.

6.4 Summary of W and Z Backgrounds

Table 6.3 summarizes the background contributions to the $W \to \mu\nu$ candidate sample and totals all the effects and uncertainties. The $Z \to \mu\mu$ backgrounds summary in table 6.4 indicates that the sample is virtually background free.

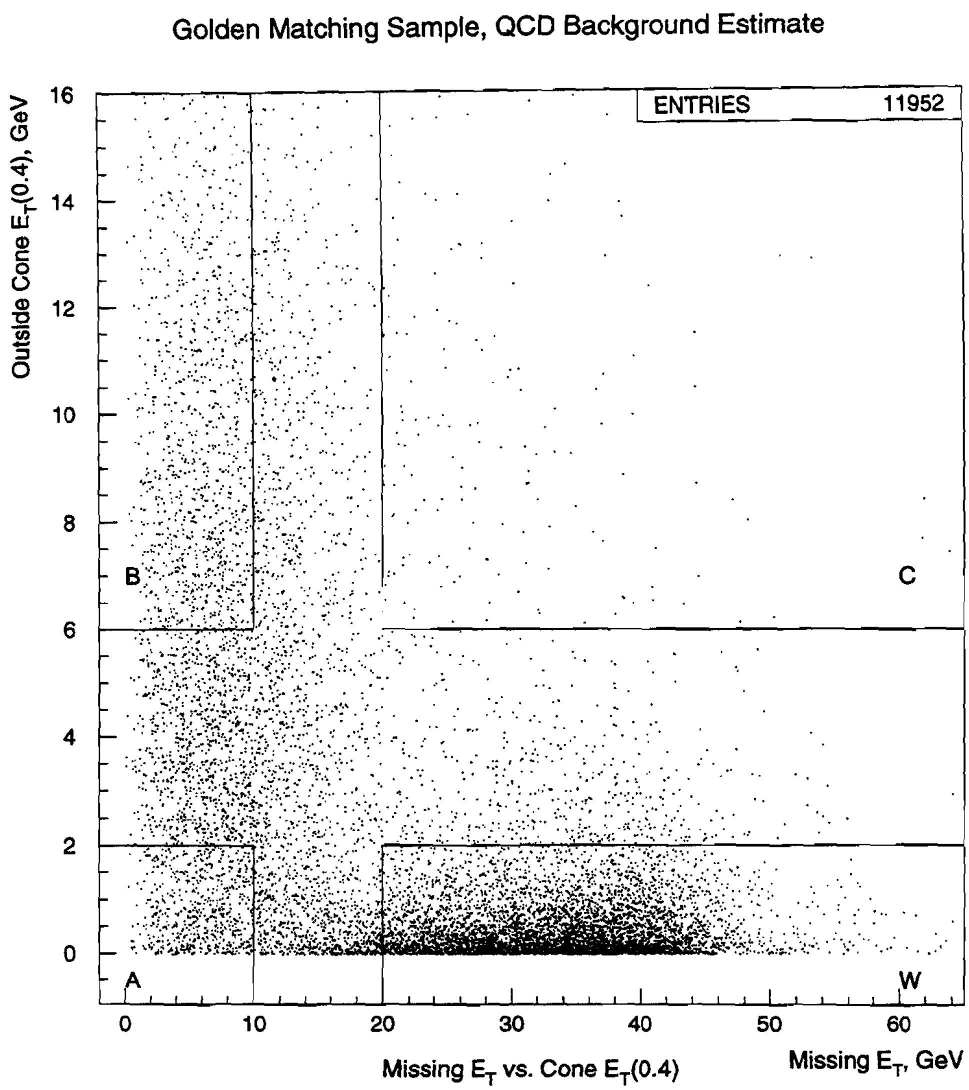

Figure 6.1: Isolation vs. Missing Transverse Energy

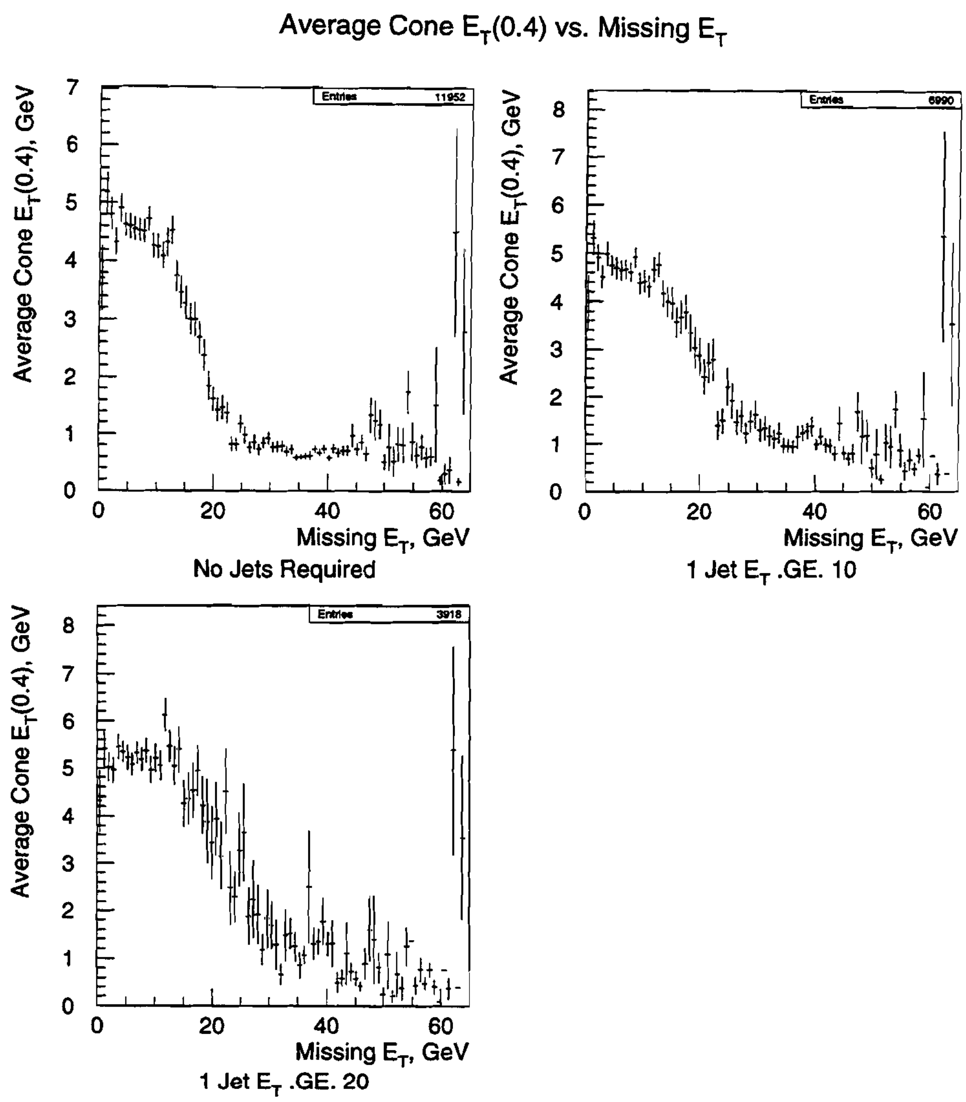

Figure 6.2: Average Isolation vs. Missing Transverse Energy, Various Jet Requirements

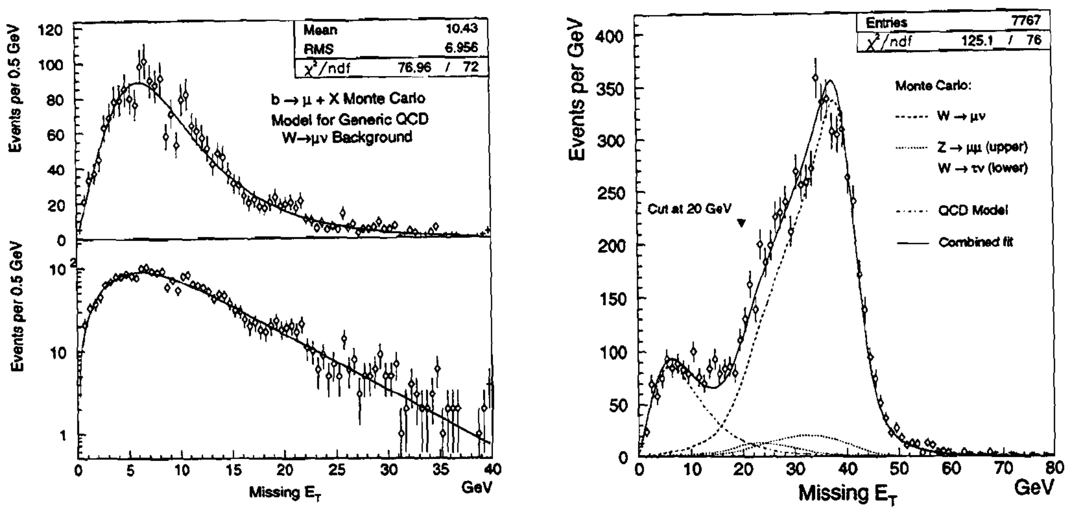

Figure 6.3: Missing Transverse Energy: from $b \to \mu + X$ Monte Carlo (left); data with fit to signal and background (right)

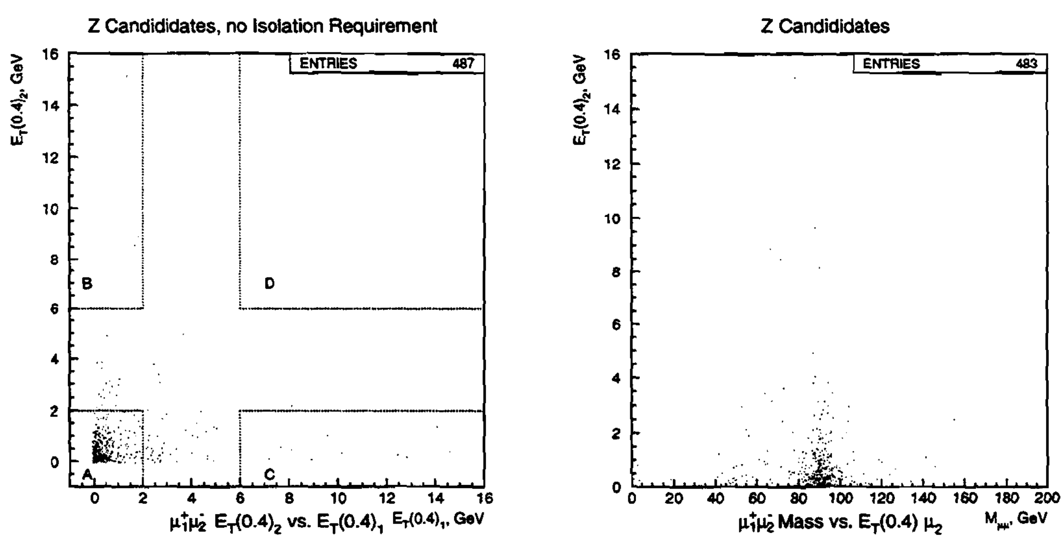

Figure 6.4: Z Candidates Muon Isolation

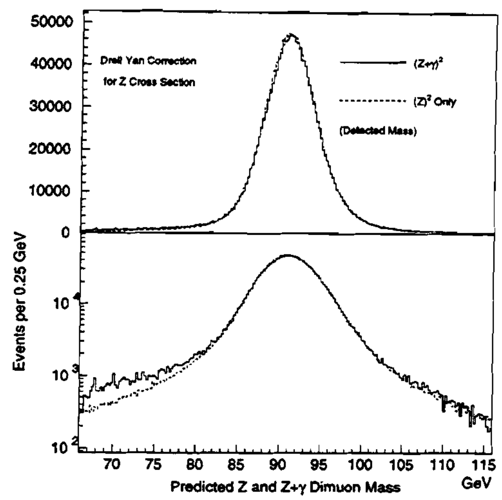

Figure 6.5: Comparison of Z and $Z + \gamma$ Dimuon Mass Spectra for Drell Yan Correction

W Background Classification	Background Estimate
General QCD Backgrounds	126.1 ± 63.3
$Z \rightarrow \mu\mu$, 1 μ Lost, Geometry	372.4 ± 21.7
$Z \rightarrow \mu\mu$, 1 μ Lost, Detector Inefficiency	21.5 ± 4.4
Top ($M_{Top} \geq 131\ GeV$) (Uncertainty only)	$0.0\ \pm^{18.9}_{0.0}$
Cosmic Rays	24.9 ± 12.5
$Z \rightarrow \tau\tau \rightarrow \mu\ +\ X$	13.7 ± 6.9
$W \rightarrow \tau\nu_\tau \rightarrow \mu\nu_\mu\nu_\tau\nu_\tau$	216.3 ± 17.5
Total W Background, B_W	$\mathbf{774.8 \pm 73.2}$

Table 6.3: $W \rightarrow \mu\nu$ Backgrounds

Z Background Classification	Background Estimate
General QCD Backgrounds	$0.0\ ^{+1.0}_{-0.0}$
$Z \rightarrow \tau\tau \rightarrow \mu\nu_\mu\mu\nu_\mu\nu_\tau\nu_\tau$	$0.2\ \pm^{1.0}_{0.2}$
Cosmic Rays	1.7 ± 0.8
Total Z Background, B_Z	$\mathbf{1.9 \pm 1.6}$
Drell-Yan Background Correction Factor	0.994 ± 0.006

Table 6.4: $Z \rightarrow \mu\mu$ Backgrounds

Chapter 7

Luminosity

The final number needed in measuring a cross section is the time integrated luminosity, $\int \mathcal{L}\ dt$. The instantaneous luminosity represents the rate of particles incident on a given area, measured here in units of $cm^{-2}sec^{-1}$. The average instantaneous luminosity during the data taking run was:

$$\mathcal{L}_{Ave} \sim 3.5 \times 10^{30}\ cm^{-2}\ sec^{-1}$$

The instantaneous luminosity varied widely from 0.1 to nearly $10.0 \times 10^{30}\ cm^{-2}\ sec^{-1}$. Figure 7.1 shows the instantaneous luminosity profile over the course of the run. To produce this histogram, instantaneous luminosity measurements for each individual run were taken at a fixed rate in real time. Each individual run distribution was then normalized to the run integrated luminosity in order to allow for changes in the real time rate from run to run.

To obtain the integrated luminosity the rates are time integrated over the course of the data run. In this chapter we describe how the luminosity is measured and normalized. We also describe a correction to the luminosity based on our data sample event vertex cut of $|z| \leq 60\ cm$, which reduces the effective observed luminosity. The luminosity and associated correction does not enter the ratio in any way, and only effects the individual cross sections.

7.1 Luminosity Measurement and Normalization

To measure the luminosity, we use the beam-beam counter (BBC) scintillator planes which cover the angular range $0.32^\circ \leq \theta \leq 4.47^\circ$. There are two sets of planes near the

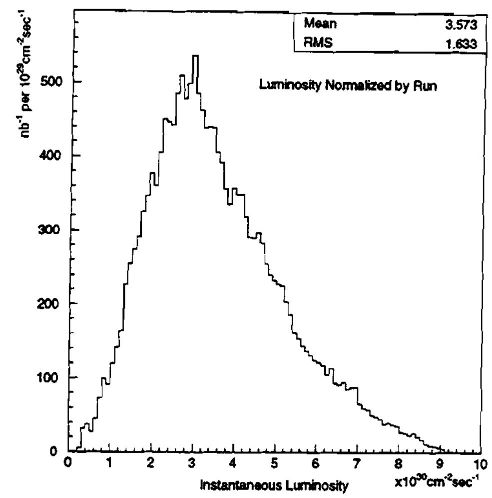

Figure 7.1: Instantaneous Luminosity Profile

beampipe in the far forward region, on both the east and west sides of the detector. The rate of coincidence hits between the east and west sets of scintillators serves as the luminosity monitor. As such, the beam-beam counters represent a measurement independent of the central detector systems.

The raw rate originates from a complicated mélange of processes. The uncorrected rate can be considered a "visible" cross section, σ_{BBC}. The measured σ_{BBC} is dominated by the combined elastic, inelastic, and diffractive $p\bar{p}$ interactions. However σ_{BBC} is also dependent on the amount and type of material between the interaction point and the BBC scintillators. The σ_{BBC} rate must be corrected for the effects of secondary scattering of particles back into the BBC and other accidental, coincidence processes.

The overall normalization of the visible BBC cross section can be taken from the independently measured total $p\bar{p}$ cross section documented in references [71, 72, 73]. These measurements were performed using several small drift chambers very close to the beamline, positioned at various points near the CDF detector and further down the beamline. The elastic ($p\bar{p} \rightarrow p\bar{p}$), inelastic ($p\bar{p} \rightarrow X$) single diffractive ($p\bar{p} \rightarrow \bar{p} + X$) cross sections are measured separately; the actual apparatus and procedure is quite involved and will not be described here (see references [71, 72, 73] for more details).

The total cross sections were measured in special runs during 1989. The BBC cross section can be normalized by looking at the BBC visible rates during the same special run. The following normalization procedure was developed by reference [74]. The BBC normalization can be expressed as:

$$\sigma_{BBC} = \sigma_{total} \cdot \frac{N_{BBC}^{vis}}{N_{total}}$$

where σ_{total} is the total $p\bar{p}$ cross section; N_{total} is the total event count from the σ_{total} measurement; N_{BBC}^{vis} is the event count in the same run as seen by the BBC scintillators. The total event count can be broken down into the three components:

$$N_{total} = N_e + N_d + N_i$$

where N_e is the number of elastic scattering events; N_d is the number of single diffractive scattering events; and N_i is the number of double inelastic events. The BBC cross section can be re-written according to reference [72]:

$$\sigma_{BBC} = \frac{16\pi(\hbar c)^2}{1+\rho^2} \cdot \frac{dN_e/dt|_{t=0}}{N_i + N_d + N_e} \cdot \frac{N_{BBC}^{vis}}{N_i + N_e} \qquad [72,\ 74]$$

The term $dN_e/dt|_{t=0}$ is the extrapolated slope of $N_e(t)$, where t is the momentum exchange squared in the interaction. All of these terms have been measured in references [71], [72] and [73]. Combining terms and propagating errors as described by [74] yields:

$$\sigma_{BBC} = 51.2 \pm 1.7\ mb \qquad [74]$$

We now have a normalization for the BBC detector system which will yield the luminosity for subsequent data runs:

$$\mathcal{L} = \frac{-f_0}{\sigma_{BBC}} \cdot \ln(1 - \frac{R}{f_0}) \qquad [74]$$

where R is the BBC count rate; and $f_0^{-1} \sim 3.5\ \mu sec$ is the beam crossing period. The log term is a poisson correction to treat possible multiple interactions per beam bunch crossing. The original cross section normalization measurement was made at low luminosity ($\sim 10^{28}\ cm^{-2}\ sec^{-1}$) where multiple interactions are less likely; when extrapolating to high luminosity there is an increasing probability of having more than one interaction in one crossing. For crossings with multiple interactions, that crossing will only be counted once by the BBC.

7.2 Sources of Error

The dominant source of error in the luminosity comes from the systematic error in the total cross section measurement used in the normalization, an error of $\sim 3.1\%$. Another small contribution to the normalization error includes BBC detector/trigger event systematics of $\sim 0.5\%$. The normalization also depends on the material between the BBC and the interaction point; in particular the beam pipe was changed in the middle of our data run. Comparisons to occupancy rates in the central detector before and after the change in beam pipe indicate how no clear shift in BBC rates, but a $\sim 1.0\%$ uncertainty is taken to account for this possibility. This uncertainty also takes into account variations in detector geometries from 1988 to the 1992 data run.

In computing the integrated luminosity, we must correct for correlated backgrounds, i.e., backgrounds coming from beam interactions with the residual gas in the beam pipe. These corrections are taken from runs with missing bunches (one missing p or $\bar{p}$) and are luminosity dependent. An error of $\sim 1\%$ is taken due to our limited understanding of such processes, and a $\sim 1\%$ uncertainty due to store to store variations.

The net effect of all these sources of error is $\sim 3.6\%$ on the normalized integrated luminosity. These effects are described in detail in the above mentioned references [71], [72], [73] and [74].

7.3 Event Vertex Correction

The data samples always make a cut on the event z vertex position:

$$-60\ cm \leq z_{vertex} \leq +60\ cm$$

in order to constrain the interactions to the fiducial central part of the vertex detector (VTX). The acceptance Monte Carlos generate random event z vertices with a distribution truncated at $z = \pm 60\ cm$. However, the acceptances and efficiencies measured in chapter 4 do not correct for the fact that the luminosity is calculated from the full z_{vertex} distribution.

7.3.1 Vertex Distribution Models

We can model the z_{event} distribution as approximately a Gaussian with mean and sigma of:

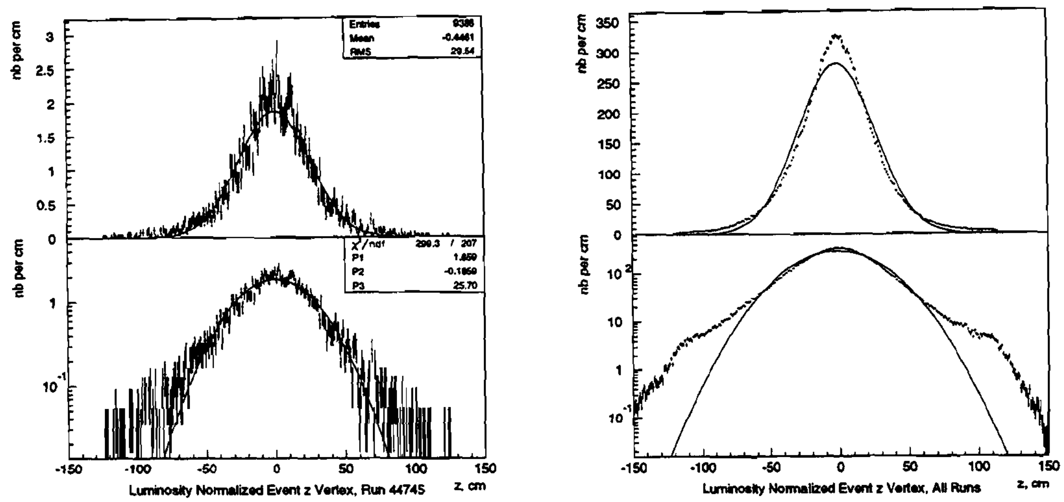

Figure 7.2: Event Vertex Distributions, Single and All Runs

$$z_0 = -1.48 \pm 0.11 \ cm \qquad \sigma_z = 26.65 \pm 0.18 \ cm$$

We obtain these values by a study of the event vertex distributions of the minimum bias data sample – a sample triggered on either the beam-beam counters described above, or from a random crossing. The distribution from each run can be fitted to a Gaussian, as shown in figure 7.2 on the left. When the distributions from all runs are combined, with each run distribution normalized to the run's luminosity, we have the distribution in figure 7.2 on the right. A best fit Gaussian is super-imposed over the distribution, and clearly does not fit the distribution. In chapter 4 we demonstrated that the acceptances are insensitive to the shape of the distribution. In contrast, the value of the vertex efficiency is quite sensitive to the shape and tails of the distribution, and so we must carefully model the functional form of the input z distribution.

However, in order to compute the individual W and Z cross sections, we need an accurate measure of the efficiency of the $|z| \leq 60 \ cm$ cut. This efficiency is primarily dependent on the nature of the proton and anti-proton beams, and effectively reduces the "visible" luminosity available to the cross section measurement:

$$\int \mathcal{L}_{visible} = \int \mathcal{L}_{BBC} \cdot \epsilon_{vertex}$$

As such, this efficiency represents a correction to the luminosity and effects only the individual cross sections and not the ratio.

A variety of ways exist to calculate the vertex efficiency. We want to compute the area of the luminosity curve between $-60\ cm \leq z \leq +60\ cm$ divided by the total area:

$$\epsilon_{vertex} = \frac{\int_{-60}^{+60} d\mathcal{L}(z)}{\int_{-\infty}^{+\infty} d\mathcal{L}(z)}$$

The overall normalization of $\mathcal{L}(z)$ drops out in the ratio, so we are concerned only with the form as a function of z. Taking the Gaussian best fit from figure 7.2 as the functional form of $\mathcal{L}(z)$ yields an efficiency of:

$$\epsilon_{vertex} = 97.54 \pm 0.68\% \quad (Gaussian\ Fit)$$

The simple Gaussian clearly does not adequately match the data. As a comparison, we take the data distribution in the same figure histogram as representative of $\mathcal{L}(z)$. Performing the integration on the data points (area method) yields:

$$\epsilon_{vertex} = 93.21 \pm 0.65\% \quad (Area\ Method)$$

The two methods of computing ϵ_{vertex} disagree significantly. We do not necessarily believe the area method, as the background shape and efficiency fall-off have not been parameterized in the distribution. Instead, we use the explicit expression for luminosity in terms of beam parameters:

$$\mathcal{L} = N_p N_{\bar{p}} \int \frac{1}{\sqrt{2\pi}\sigma_z} \frac{e^{\frac{-z^2}{2\sigma_z}}}{4\pi\sigma_x(z)\sigma_y(z)} dz$$

where:

$$\sigma_x^2(z) = \frac{1}{6\pi\gamma}\beta_x(z)\epsilon_x + (\eta(z)\frac{dp}{p})^2 \qquad \sigma_y^2(z) = \frac{1}{6\pi\gamma}\beta_y(z)\epsilon_y$$

$$\beta(z) = \beta^*[1 + (\frac{z - z_{min}}{\beta^*})^2] \qquad \sigma_z = \frac{\sigma_z^p \cdot \sigma_z^{\bar{p}}}{\sqrt{(\sigma_z^p)^2 + (\sigma_z^{\bar{p}})^2}}$$

Here N_p and $N_{\bar{p}}$ are the number of protons and anti-protons per bunch; σ_p and $\sigma_{\bar{p}}$ are the bunch lengths; σ_x and σ_y are the beam sizes in the transverse plane; β is the Tevatron beta function; $\eta(z)$ is the momentum dispersion function. The accelerator provides independent measurements of each of the parameters in the expressions above. Using the approximations $\beta_x^* \approx \beta_y^*$ and $z_x^{min} \approx z_y^{min}$ and neglecting the small momentum dispersion, $\eta(z)\frac{dp}{p} \to 0$, we obtain the proportionality:

$$\frac{d\mathcal{L}(z)}{dz} \propto \frac{e^{\frac{z^2}{2\sigma_z^2}}}{[1 + (\frac{z - z_{min}}{\beta^*})^2]}$$

7.3.2 *Computing the Event Vertex Correction*

Over the year long course of data taking, the $p\bar{p}$ beam parameters changed significantly from run to run. Therefore, to obtain the value of ϵ_{vertex}, we compute the efficiency on a run-by-run basis, then take the run luminosity weighted average to get the net efficiency:

$$\epsilon_{vertex} = \frac{\sum(\int \mathcal{L})^{Run} \cdot \epsilon_{vertex}^{Run}}{\sum(\int \mathcal{L})^{Run}}$$

where the sum is performed over all runs in the data set. For each individual run, the σ_z value is determined from the average of σ_z measurements over the course of the data run, determined from the independently measured proton and anti-proton beam sizes by the Fermilab Accelerator Division (σ_z^p and $\sigma_z^{\bar{p}}$) [75]. We take the maximum value of the minimum bias vertex distribution to obtain z_{min}. We are left with determining the β^* parameter, which is unfortunately poorly known and very difficult to measure independently. Instead, we let the value of β^* float and then compute the net vertex efficiency as a function of the effective data set value, β_{eff}^*. Figure 7.3 plots the efficiency over a range of $\beta_{eff}^* = 29\ cm$ to $38\ cm$. We note that the efficiency varies significantly over this range.

To obtain the best value of the β_{eff}^*, we compute the χ^2 as a function of β_{eff}^* by comparing the net luminosity curve with the min-bias z distributions in the relatively background free region $|z| \leq 60\ cm$. The net luminosity curve is constructed in the same way as the net efficiency:

$$\frac{d\mathcal{L}}{dz}(z, \beta_{eff}^*) = \mathcal{N} \cdot \sum_{i=Run} (\int \mathcal{L})^i \cdot \frac{d\mathcal{L}}{dz}(z, \sigma_z^i, z_{min}^i, \beta_{eff}^*)$$

where the sum i is over all runs, weighted by run luminosity. The normalization factor $\mathcal{N}$ is determined by the area under the data curve in the region $|z| \leq 60\ cm$; the χ^2 is then computed in the same region, bin width $\Delta z = 1\ cm$. The plot of this χ^2 as a function of β^*_{eff} is shown in figure 7.3. Note that in all cases we have normalized and fit to the $|z| \leq 60\ cm$ region, since we believe this region to be relatively background free.

The function in figure 7.3 (left) minimizes the χ^2 at a value of $\beta^*_{eff} = 33.0\ cm$, yielding a central value for the vertex correction of $\epsilon_{vertex} = 95.55\%$. Figure 7.4 plots the composite luminosity curve with this nominal value of β^*_{eff} in the $|z| \leq 60\ cm$ range. Note the small but persistent deviation from the luminosity curve; the following subsection evaluates the uncertainty due to this deviation. Figure 7.4 (right) plots the entire range of the z vertex distribution, $|z| \leq 300\ cm$; note the expected divergence from the luminosity curve beyond $|z| > 60\ cm$, which we attribute to a roughly flat background curve (beam-gas, etc.) convoluted with a vertex detector efficiency fall-off beyond $|z| > 110\ cm$.

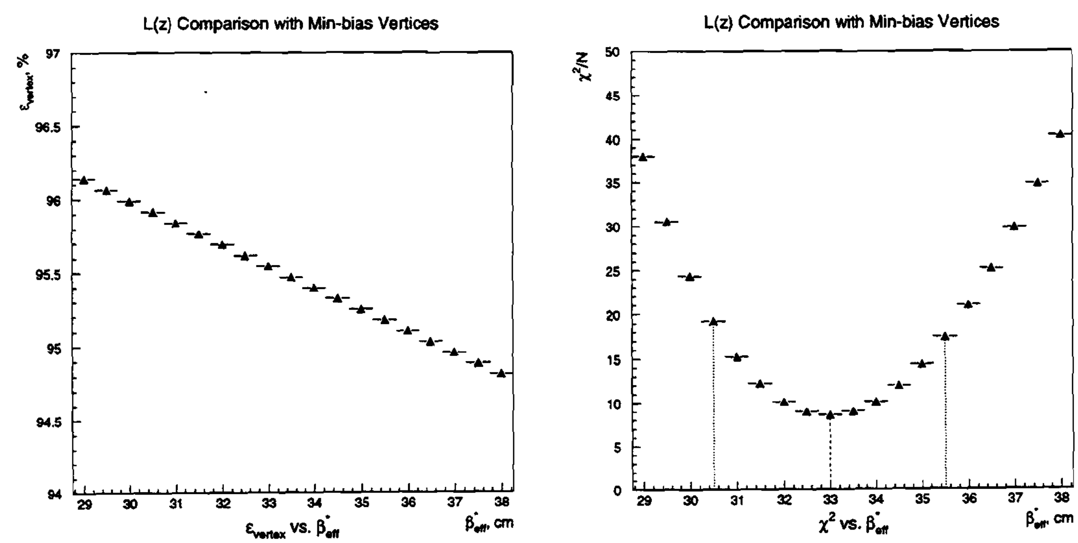

Figure 7.3: Variation of ϵ_{vertex} and fit quality with β^*_{eff}

7.3.3 Uncertainties in the Event Vertex Correction

To estimate the uncertainty on the value of ϵ_{vertex}, we consider the variation of ϵ_{vertex} with the three parameters on which $d\mathcal{L}(z)/dz$ depends. Table 7.1 summarizes the results of the variation of the parameters z_{min}, β^*_{eff}, and σ_z.

From the distribution of the run averaged z vertex position, a more than adequate variation of the z_{min} parameters would be $z_{min} = 0$ and $z_{min} = z_{mean} \times 2$. Table 7.1 indicates a small variation of ϵ_{vertex} with this variation of z_{min}.

For the variation due to the β^*_{eff} parameter, we examine the χ^2 distribution in figure 7.3. The χ^2 minimum occurs at ~ 8.5, well above the desired 1. We expect that our model still does not quite accurately represent the exact shape of the data (see figure 7.4), most likely due to the run-to-run variation in β^* and the unknown background contribution. We take the point at which the χ^2 doubles as representative of the quality of the fit. We read off the two points at which the χ^2 value increases by a factor of 2, corresponding to $\beta^*_{eff} = 30.5\ cm$ and $\beta^*_{eff} = 35.5\ cm$ (indicated by dotted lines in figure 7.3), yielding a measurement of the effective β^* of:

$$\beta^*_{eff} = 33.0 \pm 2.5\ cm$$

We then evaluate the value of ϵ_{vertex} at these points and take the spread as the error in table 7.1.

The σ_z values are taken from the Accelerator Division measurements of the p and $\bar{p}$ longitudinal bunch lengths. The quoted uncertainty from the Accelerator Division on these measurements is $\pm 5\%$ [76], which we believe to be a conservative estimate. However, there may also be additional effects due to the sampling rate of the σ_z measurements over the real time span of the CDF data run, in which the luminosity is decreasing. There are also a number of missing measurements. The typical RMS spread in σ_z for a run is $\sim 4.2\%$, so we take this as a conservative estimate for sampling fluctuations. We add 5% and 4.2% in quadrature, and apply the resulting $\pm 6.5\%$ as a scale factor to the measured values of σ_z and re-compute the corresponding efficiencies and resulting spread.

We add in quadrature the three sources of uncertainty in table 7.1 to obtain the total error of $\pm(1.05)\%$:

$$\epsilon_{vertex} = (95.55 \pm 1.05)\%$$

Applying this number to the luminosity measurement of $\int \mathcal{L}^{BBC} = 18.82 \pm 0.68\ nb^{-1}$, we obtain an effective visible luminosity:

$$\int \mathcal{L}^{vis} = \int \mathcal{L}^{BBC} \cdot \epsilon_{vertex} = 17.99 \pm 0.68\ nb^{-1}$$

Variation	ϵ_{vertex}	Error, δ
Nominal	95.55%	—
$z_{min} \to 0\ cm$	94.30%	
$z_{min} \to \times 2$	95.52%	0.61%
$\beta^*_{eff} = 30.5\ cm$	95.92%	
$\beta^*_{eff} = 35.5\ cm$	95.18%	0.37%
$\sigma_z \to +6.5\%$	94.77%	
$\sigma_z \to -6.5\%$	96.31%	0.77%
Total Error	$(\pm 1.05)\%$	

Table 7.1: Variation of ϵ_{vertex}

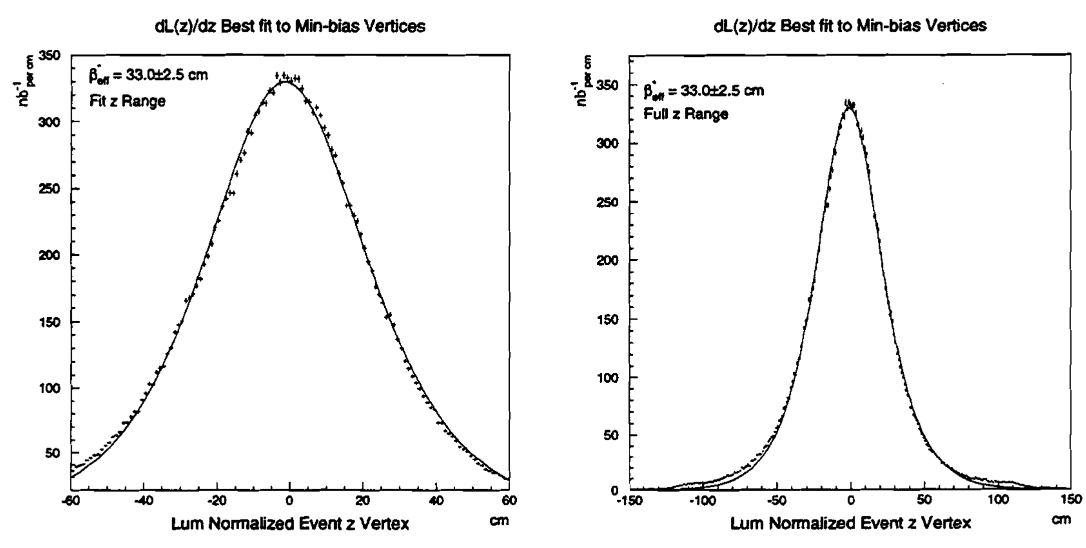

Figure 7.4: Best Luminosity Curve compared with min-bias z distribution, fit region and full region

Chapter 8

Results and Conclusions

With the event counts, backgrounds, efficiencies, acceptances and luminosity developed in the preceeding chapters, we can now assemble all the numbers and compute the measured cross sections and the cross section ratio. With the cross section ratio, we extract the $W \to \mu\nu$ branching ratio and the total W width. A summary of all results is listed in table 8.1.

8.1 Measurement of Cross Sections

Using the cross section formula defined in the event selection chapter:

$$\sigma = \frac{N - B}{\epsilon \cdot A \cdot \int \mathcal{L}}$$

where we correct the integrated luminosity of $\int \mathcal{L} = 18.82 \pm 0.68\ cm^{-2}sec^{-1}$ with the event vertex correction value of $(95.55 \pm 1.05)\%$. Only in computing the cross sections do we use the luminosity or the vertex correction. Collecting the factors N, B, ϵ , A , and $\int \mathcal{L}$ we can now compute the W and Z cross sections times branching ratios:

$$\sigma \cdot B(W \to \mu\nu) = 2.521 \pm 0.032(stat) \pm 0.106(syst) \pm 0.095(lum)\ nb$$

$$\sigma \cdot B(Z \to \mu\mu) = 0.1895 \pm 0.0092(stat) \pm 0.0083(syst) \pm 0.0072(lum)\ nb$$

Here we divide the error on the measurement into three parts. The statistical error ($stat$) consists only of the candidate count statistical uncertainty. The systematic error ($syst$) combines the uncertainties due to the efficiency, acceptance, and background calculations. The luminosity error (lum) combines the uncertainty on the luminosity measurement and the vertex correction; this error is properly a systematic error, but we factor it out for convenience of comparison – previous measurements of the cross sections have been dominated by this uncertainty. The W cross section is dominated by the systematic uncertainties of the efficiency and acceptance, while the Z cross section continues to be dominated by the statistics of the sample. The combined errors are added in quadrature and are listed in table 8.1.

We compare our cross section results with recent theoretical predictions in figure 8.1, plotting $\sigma \cdot B$ vs. the center of mass energy of the proton-antiproton system [50]. The central value of the theoretical prediction is shown as the solid line and was calculated by Stirling using the new $MRS\ A$ [49] parton distribution functions and a next-to-next-to-leading order parton subprocess calculation [53]. The dotted lines give some idea of the theoretical uncertainty – the dominant contribution is due to parton distribution functions and QCD scale uncertainty, with a small W mass dependence, both estimated from reference [51]. (We assume here the fractional theory uncertainty is constant as a function of $\sqrt{s}$.) Also plotted is the previously published result from the UA1 [77] experiment at $\sqrt{s} = 0.63\ TeV$ and the previous CDF measurement [40]. (Note that the CDF plotted points are offset by $\pm 20\ GeV$ from the actual $\sqrt{s}$ values so that overlapping points are readable.)

8.2 Measurement of R_μ

The experimental advantage of computing the ratio of cross sections is clear when we are able to cancel the luminosity, vertex correction, and primary muon efficiencies (to first order). The luminosity completely cancels along with its large uncertainty. The expression for the ratio of cross sections in terms of measured quantities is explicitly:

$$R_\mu = \frac{N_W - B_W}{N_Z - B_Z} \cdot \frac{A_Z}{A_W} \cdot [f_{\mu\mu} \cdot (2\epsilon_s \cdot (1 + \epsilon_c - \epsilon_c \cdot T) - (2 - T) \cdot \epsilon_p)) + (1 - f_{\mu\mu}) \cdot \epsilon_s \cdot (1 - \Delta\epsilon_\eta)]$$

where the term in brackets is the ratio of Z and W efficiencies as defined in previous chapters. Collecting terms, we compute the ratio as:

$$R_\mu = 13.30 \pm 0.67(stat) \pm 0.42(syst)$$

Here we have only two error factors. The statistical error ($stat$) combines the candidate statistics of the W and Z samples, where the Z sample dominates. The systematic error

($syst$) combines uncertainties from the background estimate, the acceptance ratio, and the residual efficiency terms. Note that the ratio has a correlated error between the number of Z candidates and the W background. The Z statistics dominate the total error, which is given by the two components added in quadrature and listed in table 8.1.

8.3 Extraction of $BR(W \to \mu\nu)$ and $\Gamma(W)$

We now take advantage of the decomposition of the ratio stated in the introduction chapter:

$$R_\mu = \frac{\sigma \cdot B(W \to \mu\nu)}{\sigma \cdot B(Z \to \mu\mu)} = \frac{\sigma(W)}{\sigma(Z)} \cdot \frac{\Gamma(W \to \mu\nu)}{\Gamma(W)} \cdot \frac{\Gamma(Z)}{\Gamma(Z \to \mu\mu)}$$

We take the production cross section ratio from theory and the LEP measurements provide the branching ratio of $Z \to \mu\mu$:

$$\frac{\sigma(W)}{\sigma(Z)} = 3.33 \pm 0.03 \ \ [50] \qquad \frac{\Gamma(Z \to \mu\mu)}{\Gamma(Z)} = 0.03366 \pm 0.00019 \ \ [16]$$

We can now extract the W muonic branching ratio $B(W \to \mu\nu)$ based on these external numbers and our measured value of R_μ. We obtain:

$$BR(W \to \mu\nu) = 0.1345 \pm 0.0068(stat) \pm 0.0045(syst)$$

The branching ratio is a derived quantity from the measured R_μ, and like R_μ, is independent of luminosity. Alternatively, we can extract the total width of the W by using the same ratio of production cross sections, the theoretical prediction of the ratio of W and Z branching ratios, and the measured total Z width from LEP:

$$\frac{\Gamma(W \to \mu\nu)}{\Gamma(Z \to \mu\mu)} = 2.696 \pm 0.018 \ \ [48] \qquad \Gamma(Z) = 2.489 \pm 0.007 \ GeV \ \ [16]$$

We then obtain the W total width to be:

$$\Gamma(W) = 1.689 \pm 0.085(stat) \pm 0.057(syst) \ GeV$$

Again, the total width here is a derived quantity from the measured value of R_μ. We compare this value with the theoretical prediction and all other world measurements of the W total width in figure 8.2. The theoretical uncertainties originate from errors on the W mass, top quark mass, and QCD renormalization scale. The UA1, UA2, CDF and

Summary of $W \to \mu\nu$ and $Z \to \mu\mu$ Results		
$\int \mathcal{L} = 18.82 \pm 0.68 pb^{-1}$	W	Z
Inclusive Muons	14,119	
Primary Muons	8354	
Candidates	6222	423
Background	774.8 ± 73.2	1.7 ± 0.8
Signal Events	$5447.2 \pm 68.6 \pm 140.7$	$421.1 \pm 20.5 \pm 1.6$
Efficiency	0.7422 ± 0.0272	$0.7450 \pm^0 .0297$
Acceptance	0.1619 ± 0.0025	0.1649 ± 0.0028
Vertex Correction	0.9555 ± 0.0105	
$\sigma \cdot B$	$2.521 \pm 0.146\ nb$	$0.1895 \pm 0.0143\ nb$
R_μ	13.30 ± 0.78	
$\Gamma(W \to \mu\nu)/\Gamma(W)$	0.1345 ± 0.0081	
$\Gamma(W)/\Gamma(W \to \mu\nu)$	7.437 ± 0.448	
$\Gamma(W)$	1.689 ± 0.102	

Table 8.1: Summary of Results

DØ measurements all use the same method for extracting the W width. The preliminary direct measurement of the W width at the bottom of the figure is outlined in the following appendix and in reference [80].

8.4 Limits on Unknown Decay Channels

The branching ratio $BR(W \to \mu\nu)$ can be used to search for unknown decay modes of the W. If an extra decay channel for the W is allowed, the total width of the W will increase, thus decreasing the muonic branching ratio. Using this effect, we can search for heavy quark pairs up to $M_{u'} + M_{d'} < M_W$. We apply this technique to the top quark and plot the inverse branching ratio versus the top mass in figure 8.3, based on standard model coupling to the top and bottom quarks [79]. Except for the coupling assumption, this method should be model independent in that it makes no assumptions concerning the subsequent decay modes of the top quark. We plot the inverse branching ratio because this quantity is directly proportional to the number of Z candidates (our dominant source of uncertainty), which we expect to be a more nearly Gaussian error distribution.

Under the assumption that the error on the inverse branching ratio is Gaussian, we compute a 95% confidence level limit on the quantity, using the technique described in reference [81]. The inverse branching ratio is bounded by the asymptotic theory prediction for a heavy top. The projection of the 95% confidence level limit onto the theory curve provides a corresponding 95% confidence level limit on the mass of the top quark, or any postulated quark coupling directly to the W and the b quark:

$$M_q > 68\ GeV, \quad 95\%\ C.L.$$

The limits are plotted with the data point in figure 8.3, along with the previous CDF measurement from the 1989 data for comparison.

8.5 Conclusions

We have presented a measurement of the W and Z cross sections in the muon decay channel in $p\bar{p}$ collisions at $\sqrt{s} = 1.8$ TeV. As well, we have presented the ratio of those cross sections, R_μ. From these values we have extracted the $W \rightarrow \mu\nu$ branching ratio and the total W width, $\Gamma(W)$. All of these results are summarized in table 8.1. In table 8.2 we break down the sources of error on the various measurements and extracted values.

In figures 8.1, 8.2 and 8.3 we compare our results with the theoretically predicted values. We note that the individual W and Z cross sections are in reasonable agreement with the theoretical values in figure 8.1. In this plot, we see that the W and Z cross sections have deviated in opposite directions from the standard model predictions. The ratio of cross sections cancels correlated errors (particularly luminosity), and so the ratio ends up deviating by a larger fraction than the individual cross sections.

The ratio of cross sections and the associated extracted branching ratio and W width deviate from the theoretical prediction by about 3 standard deviations. Assuming that the error is Gaussian, there is only a very small probability that this deviation is due to random fluctuations in this single measurement. However, within the context of the several world measurements of the W width in figure 8.2, the probability that a single measurement deviates from the standard model prediction is not so remarkable.

At this time we are unable to constrain the theoretical predictions of the standard model with these measurements. The errors on the W width are too large to be sensitive to possible oblique corrections on the W width contained in the δ correction as defined in chapter 1. The individual cross sections have errors too large to constrain either par-

Source	$\sigma \cdot B(W)$	$\sigma \cdot B(Z)$	$\Gamma(W)$
Statistics	1.3%	4.9 %	5.1 %
Luminosity	3.8%	3.8 %	–
Acceptance	1.6%	1.7 %	1.8 %
Efficiencies	3.7%	4.0 %	1.6 %
Background	1.3%	0.6 %	1.4 %
Theory	–	–	1.0 %

Table 8.2: Sources of Error

ton distributions or the QCD subprocess predictions. However, the measurements here represent a unique test of the consistency of the standard model theory in these respects, without actually constraining the theory further. See the following Appendix for a discussion of prospects for future measurements. The deviation of the extracted W width from the predicted value in this channel merits further measurement during the next run of the Tevatron collider.

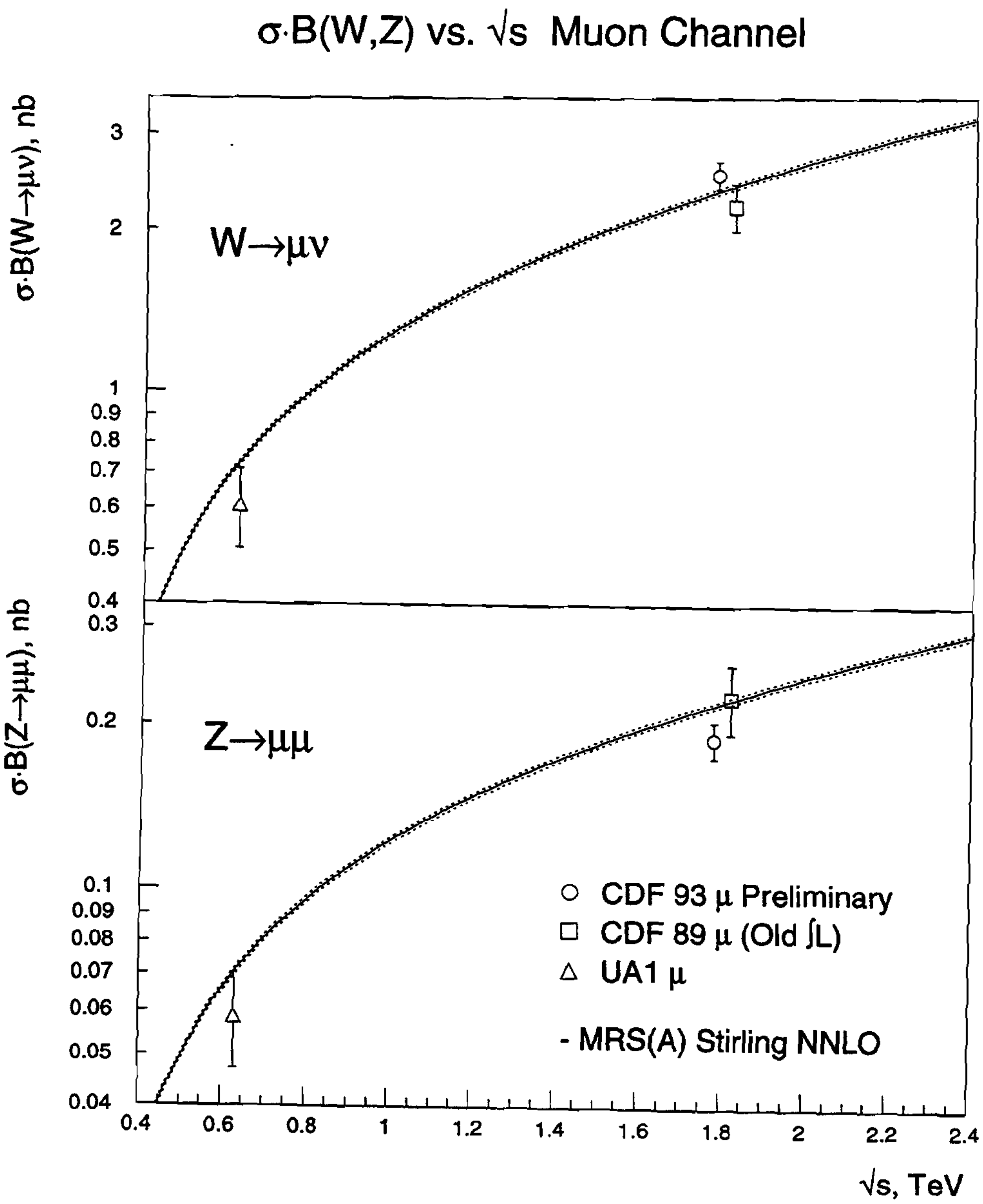

Figure 8.1: W and Z Cross Sections vs. $p\bar{p}$ Center of Mass Energy

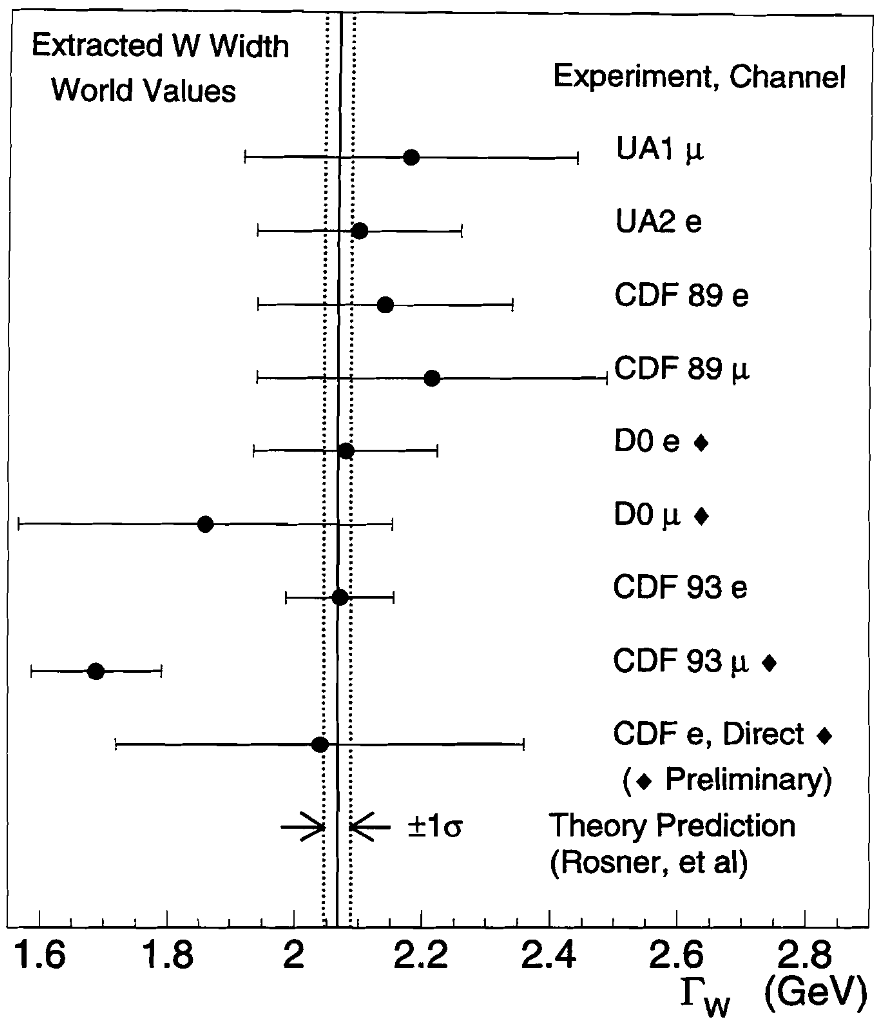

Figure 8.2: Comparison of W Total Width to Theory and other Experiments

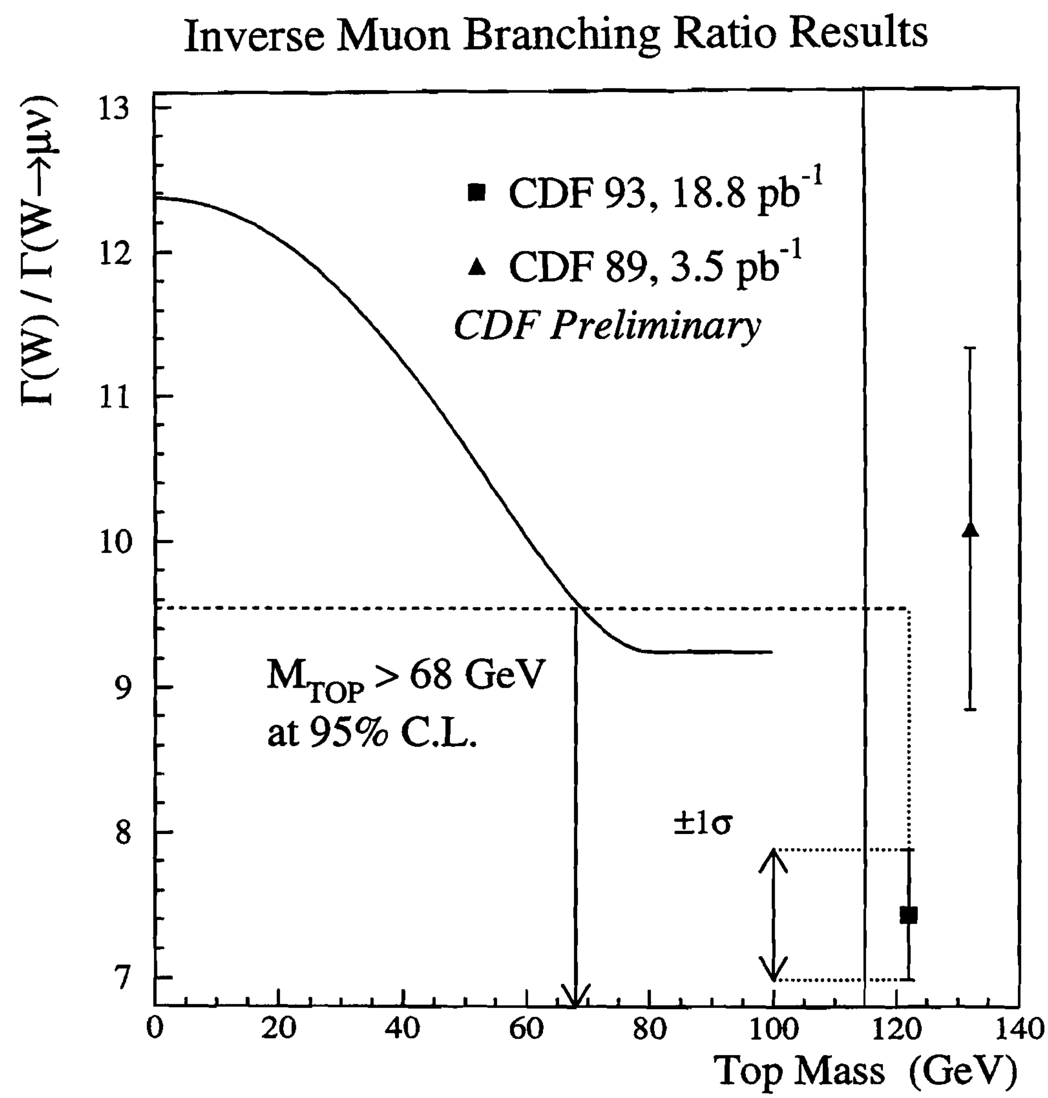

Figure 8.3: Top Quark Mass vs. Inverse Branching Ratio

Appendices

Appendix A

Prospects for Future Measurements

Another data collection run is currently underway at Fermilab. This run is expected to continue until sometime in 1995 with a total additional integrated luminosity of at least $\sim 70\ pb^{-1}$, or perhaps even as high as $\sim 200\ pb^{-1}$. In this appendix we discuss the prospects for improving the cross section and ratio measurements, as well as some possible drawbacks of the new run. A direct measurement of the W width is also discussed.

A.1 Immediate Prospects for Cross Section Measurements

With additional statistics, we expect the statistical errors to be reduced by the usual $\sqrt{N}$ factor. However, the systematic errors should also be reduced since many sources of systematic error have a hidden statistical dependence. In particular, the efficiencies all consistently use the Z sample to measure the selection, chamber and trigger efficiencies. The uncertainty in the chamber and trigger efficiencies dominate the efficiency error and will benefit substantially with a four fold increase in statistics. However, with increased instantaneous luminosity not everything will improve in the measurement.

A.1.1 Improvements

The acceptance uncertainty will also benefit from increased statistics. The W charge asymmetry measurement [55] is currently our most sensitive indicator of the parton distribution functions. This measurement is statistically limited in the 1992-93 data run, and should improve significantly with the added data. The possibility of excluding some parton distribution functions will directly reduce the acceptance uncertainty, most sensitively in the absolute W and Z acceptances.

With increased Z statistics, we also will be able to improve the underlying event model. By simultaneously measuring the Z candidate P_T directly from the decay leptons and from the calorimeter response to the recoil jets, we have an ideal model for the underlying event. The calorimeter response to the Z boost will fold in all factors, including jet recoil, spectator activity, and detector response. With the 1992-93 data run, we are unable to use this method due to the low statistics at higher Z boson P_T. This method was first developed for the current W mass analysis [57] and is feasible in the M_W measurement since the candidates are selected to have low W transverse momentum. Increased Z statistics may allow this method to be used for the cross sections.

A.1.2 Disadvantages

With the rising instantaneous luminosity of the new data run, the spurious background trigger rate begins to diverge, particularly in the area of the CMU detector without CMP coverage. Various schemes with additional trigger requirements have been developed; such schemes will invariably lower the efficiency and increase the systematic uncertainty in the efficiency measurements. If the instantaneous luminosity regularly approaches $\mathcal{L} \sim 10^{31}\ cm^{-1} sec^{-2}$ or more, this inclusive muon trigger region will be completely excluded, thus reducing the geometric acceptance. As well, the Level 2 CFT trigger threshold has already been increased. On the positive side, the CMX inclusive muon trigger is now stable and included as part of regular data taking. This increases the inclusive muon acceptance, but with the caveat that efficiencies are more difficult to understand and compute in the CMX chambers.

We do not expect to improve the sources of error on the luminosity factor. Indeed, as the instantaneous luminosity rises, the systematic error on measuring the BBC rates can conceivably get worse. This situation motivates further the measurement of the ratio rather than the absolute cross sections. With the large uncertainty on the final integrated luminosity and the detector changes involved, we leave this discussion on a qualitative basis only.

A.2 Prospects for Direct W Width Measurement

The extraction of the W width that has been presented here is not a direct measurement and involves several theoretical dependencies. As outlined in reference [39], we should be able to extract a direct measurement of the W width by exploiting the changing $\Gamma(W)$ dependency of the cross section with $\sqrt{\hat{s}}$:

$$\frac{d\sigma}{d\hat{s}} \propto \frac{\Gamma_{ij}\Gamma_{l\nu_l}}{(\hat{s} - M_W^2)^2 + M_W^2\Gamma(W)^2} \text{ [39]}$$

By fitting the M_T tail of the W candidates transverse mass spectrum to the W width, we should be able to extract a direct measurement of the W width. This procedure would use similar methods to those used in the W mass analysis [57], but with restricting the range of M_T to high values. Note that the W mass fitting procedure can let the width float, but is insensitive to the variations in the width value due to the low M_T restrictions. A first use of this method in the $W \to e\nu$ sample can be found in reference [80].

Preliminary looks into using this method in the $W \to \mu\nu$ candidate sample have shown that the muon channel is not ideal for this method. The W candidates at high transverse mass are usually muons of high transverse momentum. Since the P_T uncertainty increases with the square of the P_T, the high tail of W candidates are dominated by tracking anomalies. The W background is also a function of transverse mass, which becomes more sensitive at high mass.

Reference [80] has shown that this method is feasible in the $W \to e\nu$ channel, and yields a value:

$$\Gamma(W) = 2.16 \pm 0.30(stat) \pm 0.16(syst) \text{ [80]}$$

This measurement is highly statistics limited and will benefit greatly during the new run. The total uncertainty is not yet competitive with the value extracted from the cross section ratio, but represents the best current direct measurement of the W width.

A.3 Far Future Prospects for W Physics

In a few years we expect the Fermilab Main Injector to be complete and to replace the Main Ring as the Tevatron injector. The Main Injector should bring about a substantial improvement in the instantaneous luminosity. The accompanying data run could bring up to $\int \mathcal{L} \sim fb^{-1}$, radically improving the statistical prospects. Substantially increased instantaneous luminosity brings a whole host of systematic problems in the operation of the detector and in understanding the underlying event, significantly damaging our potential to measure the W mass and width. The Main Injector represents a major challenge and opportunity to continue precision electroweak measurements. The possibility of an energy upgrade of the Tevatron would allow further studies in the higher kinematic regime, with higher W and Z cross sections.

Also in the next two or three year, the LEP 2 e^+e^- Collider at CERN (located near Geneva, Switzerland) will turn on. LEP 2 will operate at a production of W pairs. In spite of the low threshold rate of W pair production, they should be able to measure the W width to an accuracy of about $\sim 20 - 40\ MeV$ over a few years of running, with optimistic assumptions. As well, the ever increasing luminosity of the HERA $e^{\pm}p$ collider allows a new kinematic window into charged and neutral current interactions.

In the far future, the LHC proton-proton collider operating at $\sqrt{s} \sim 13\ TeV$ will allow measurements in a different kinematic and initial state regime. However, the very high instantaneous luminosity of $\sim 10^{34} cm^{-1} sec^{-2}$ may prohibit precision measurements.

Appendix B

CDF Collaboration

The operation of the CDF Experiment represents the collaborative efforts of many people. The actual collaboration membership evolves from year to year. Below are listed the members of the collaboration during the 1992-1993 data run. The collaboration includes 397 people from 34 different institutions in five different countries, all of whom played some rôle in the CDF experiment described in this thesis. Acknowledgement also goes to the many technicians, assistants and engineers who have helped in the design and construction of the CDF detector, at many of the institutions listed below.

— ◇ —

F. Abe,[13] M. G. Albrow,[7] D. Amidei,[16] J. Antos,[28] C. Anway-Wiese,[4] G. Apollinari,[26] H. Areti,[7] P. Auchincloss,[25] F. Azfar,[21] P. Azzi,[20] N. Bacchetta,[18] W. Badgett,[16] M. W. Bailey,[24] J. Bao,[34] P. de Barbaro,[25] A. Barbaro-Galtieri,[14] V. E. Barnes,[24] B. A. Barnett,[12] P. Bartalini,[23] G. Bauer,[15] T. Baumann,[9] F. Bedeschi,[23] S. Behrends,[2] S. Belforte,[23] G. Bellettini,[23] J. Bellinger,[33] D. Benjamin,[32] J. Benlloch,[15] D. Benton,[21] A. Beretvas,[7] J. P. Berge,[7] S. Bertolucci,[8] A. Bhatti,[26] K. Biery,[11] M. Binkley,[7] F. Bird,[29] D. Bisello,[20] R. E. Blair,[1] C. Blocker,[29] A. Bodek,[25] V. Bolognesi,[23] D. Bortoletto,[24] C. Boswell,[12] T. Boulos,[14] G. Brandenburg,[9] E. Buckley-Geer,[7] H. S. Budd,[25] K. Burkett,[16] G. Busetto,[20] A. Byon-Wagner,[7] K. L. Byrum,[1] C. Campagnari,[7] M. Campbell,[16] A. Caner,[7] W. Carithers,[14] D. Carlsmith,[33] A. Castro,[20] Y. Cen,[21] F. Cervelli,[23] J. Chapman,[16] M.-T. Cheng,[28] G. Chiarelli,[8] T. Chikamatsu,[31] S. Cihangir,[7] A. G. Clark,[23] M. Cobal,[23] M. Contreras,[5] J. Conway,[27] J. Cooper,[7] M. Cordelli,[8] D. P. Coupal,[29] D. Crane,[7] J. D. Cunningham,[2] T. Daniels,[15] F. DeJongh,[7] S. Delchamps,[7] S. Dell'Agnello,[23] M. Dell'Orso,[23] L. Demortier,[26] B. Denby,[23] M. Deninno,[3] P. F. Derwent,[16] T. Devlin,[27] M. Dickson,[25] S. Donati,[23] R. B. Drucker,[14] A. Dunn,[16] K. Einsweiler,[14] J. E. Elias,[7] R. Ely,[14] E. Engels, Jr.,[22] S. Eno,[5] D. Errede,[10] S. Errede,[10] Q. Fan,[25] B. Farhat,[15] I. Fiori,[3] B. Flaugher,[7] G. W. Foster,[7] M. Franklin,[9] M. Frautschi,[18] J. Freeman,[7] J. Friedman,[15] H. Frisch,[5] A. Fry,[29] T. A. Fuess,[1] Y. Fukui,[13] S. Funaki,[31] G. Gagliardi,[23] S. Galeotti,[23] M. Gallinaro,[20] A. F. Garfinkel,[24] S. Geer,[7] D. W. Gerdes,[16] P. Giannetti,[23] N. Giokaris,[26] P. Giromini,[8] L. Gladney,[21] D. Glenzinski,[12] M. Gold,[18] J. Gonzalez,[21] A. Gordon,[9] A. T. Goshaw,[6] K. Goulianos,[26] H. Grassmann,[6] A. Grewal,[21] G. Grieco,[23] L. Groer,[27] C. Grosso-Pilcher,[5] C. Haber,[14] S. R. Hahn,[7] R. Hamilton,[9] R. Handler,[33] R. M. Hans,[34] K. Hara,[31] B. Harral,[21] R. M. Harris,[7] S. A. Hauger,[6] J. Hauser,[4] C. Hawk,[27] J. Heinrich,[21] D. Cronin-Hennessy,[6] R. Hollebeek,[21] L. Holloway,[10] A. Hölscher,[11] S. Hong,[16] G. Houk,[21] P. Hu,[22] B. T. Huffman,[22] R. Hughes,[25] P. Hurst,[9] J. Huston,[17] J. Huth,[9] J. Hylen,[7] M. Incagli,[23] J. Incandela,[7] H. Iso,[31] H. Jensen,[7] C. P. Jessop,[9] U. Joshi,[7] R. W. Kadel,[14] E. Kajfasz,[7a] T. Kamon,[30] T. Kaneko,[31] D. A. Kardelis,[10] H. Kasha,[34] Y. Kato,[19] L. Keeble,[30] R. D. Kennedy,[27] R. Kephart,[7] P. Kesten,[14] D. Kestenbaum,[9] R. M. Keup,[10] H. Keutelian,[7] F. Keyvan,[4] D. H. Kim,[7] H. S. Kim,[11] S. B. Kim,[16] S. H. Kim,[31] Y. K. Kim,[14] L. Kirsch,[2] P. Koehn,[25] K. Kondo,[31] J. Konigsberg,[9] S. Kopp,[5] K. Kordas,[11] W. Koska,[7] E. Kovacs,[7a] W Kowald,[6] M. Krasberg,[16] J. Kroll,[7] M. Kruse,[24] S. E. Kuhlmann,[1] E. Kuns,[27] A. T. Laasanen,[24] S. Lammel,[4] J. I. Lamoureux,[33] T. LeCompte,[10] S. Leone,[23] J. D. Lewis,[7] P. Limon,[7] M. Lindgren,[4] T. M. Liss,[10] N. Lockyer,[21] O. Long,[21] M. Loreti,[20] E. H. Low,[21] J. Lu,[30] D. Lucchesi,[23] C. B. Luchini,[10] P. Lukens,[7] P. Maas,[33] K. Maeshima,[7] A. Maghakian,[26] P. Maksimovic,[15] M. Mangano,[23] J. Mansour,[17] M. Mariotti,[23] J. P. Marriner,[7] A. Martin,[10] J. A. J. Matthews,[18] R. Mattingly,[2] P. McIntyre,[30] P. Melese,[26] A. Menzione,[23] E. Meschi,[23] G. Michail,[9] S. Mikamo,[13] M. Miller,[5] R. Miller,[17] T. Mimashi,[31] S. Miscetti,[8] M. Mishina,[13] H. Mitsushio,[31] S. Miyashita,[31] Y. Morita,[13] S. Moulding,[26] J. Mueller,[27] A. Mukherjee,[7] T. Muller,[4] P. Musgrave,[11] L. F. Nakae,[29] I. Nakano,[31] C. Nelson,[7] D. Neuberger,[4] C. Newman-Holmes,[7] L. Nodulman,[1] S. Ogawa,[31] S. H. Oh,[6] K. E. Ohl,[34] R. Oishi,[31] T. Okusawa,[19] C. Pagliarone,[23] R. Paoletti,[23] V. Papadimitriou,[7] S. Park,[7] J. Patrick,[7] G. Pauletta,[23] M. Paulini,[14] L. Pescara,[20] M. D. Peters,[14] T. J. Phillips,[6] G. Piacentino,[3] M. Pillai,[25] R. Plunkett,[7] L. Pondrom,[33] N. Produit,[14] J. Proudfoot,[1] F. Ptohos,[9] G. Punzi,[23] K. Ragan,[11] F. Rimondi,[3] L. Ristori,[23] M. Roach-Bellino,[32]

W. J. Robertson,[6] T. Rodrigo,[7] J. Romano,[5] L. Rosenson,[15] W. K. Sakumoto,[25] D. Saltzberg,[5] A. Sansoni,[8] V. Scarpine,[30] A. Schindler,[14] P. Schlabach,[9] E. E. Schmidt,[7] M. P. Schmidt,[34] O. Schneider,[14] G. F. Sciacca,[23] A. Scribano,[23] S. Segler,[7] S. Seidel,[18] Y. Seiya,[31] G. Sganos,[11] A. Sgolacchia,[3] M. Shapiro,[14] N. M. Shaw,[24] Q. Shen,[24] P. F. Shepard,[22] M. Shimojima,[31] M. Shochet,[5] J. Siegrist,[29] A. Sill,[7a] P. Sinervo,[11] P. Singh,[22] J. Skarha,[12] K. Sliwa,[32] D. A. Smith,[23] F. D. Snider,[12] L. Song,[7] T. Song,[16] J. Spalding,[7] L. Spiegel,[7] P. Sphicas,[15] A. Spies,[12] L. Stanco,[20] J. Steele,[33] A. Stefanini,[23] K. Strahl,[11] J. Strait,[7] D. Stuart,[7] G. Sullivan,[5] K. Sumorok,[15] R. L. Swartz, Jr.,[10] T. Takahashi,[19] K. Takikawa,[31] F. Tartarelli,[23] W. Taylor,[11] Y. Teramoto,[19] S. Tether,[15] D. Theriot,[7] J. Thomas,[29] T. L. Thomas,[18] R. Thun,[16] M. Timko,[32] P. Tipton,[25] A. Titov,[26] S. Tkaczyk,[7] K. Tollefson,[25] A. Tollestrup,[7] J. Tonnison,[24] J. F. de Troconiz,[9] J. Tseng,[12] M. Turcotte,[29] N. Turini,[3] N. Uemura,[31] F. Ukegawa,[21] G. Unal,[21] S. van den Brink,[22] S. Vejcik, III,[16] R. Vidal,[7] M. Vondracek,[10] R. G. Wagner,[1] R. L. Wagner,[7] N. Wainer,[7] R. C. Walker,[25] G. Wang,[23] J. Wang,[5] M. J. Wang,[28] Q. F. Wang,[26] A. Warburton,[11] G. Watts,[25] T. Watts,[27] R. Webb,[30] C. Wendt,[33] H. Wenzel,[14] W. C. Wester, III,[14] T. Westhusing,[10] A. B. Wicklund,[1] E. Wicklund,[7] R. Wilkinson,[21] H. H. Williams,[21] P. Wilson,[5] B. L. Winer,[25] J. Wolinski,[30] D. Y. Wu,[16] X. Wu,[23] J. Wyss,[20] A. Yagil,[7] W. Yao,[14] K. Yasuoka,[31] Y. Ye,[11] G. P. Yeh,[7] P. Yeh,[28] M. Yin,[6] J. Yoh,[7] T. Yoshida,[19] D. Yovanovitch,[7] I. Yu,[34] J. C. Yun,[7] A. Zanetti,[23] F. Zetti,[23] L. Zhang,[33] S. Zhang,[16] W. Zhang,[21] and S. Zucchelli[3]

(CDF Collaboration)

[1] *Argonne National Laboratory, Argonne, Illinois 60439*

[2] *Brandeis University, Waltham, Massachusetts 02254*

[3] *Istituto Nazionale di Fisica Nucleare, University of Bologna, I-40126 Bologna, Italy*

[4] *University of California at Los Angeles, Los Angeles, California 90024*

[5] *University of Chicago, Chicago, Illinois 60637*

[6] *Duke University, Durham, North Carolina 27708*

[7] *Fermi National Accelerator Laboratory, Batavia, Illinois 60510*

[8] *Laboratori Nazionali di Frascati, Istituto Nazionale di Fisica Nucleare, I-00044 Frascati, Italy*

[9] *Harvard University, Cambridge, Massachusetts 02138*

[10] *University of Illinois, Urbana, Illinois 61801*

[11] *Institute of Particle Physics, McGill University, Montreal H3A 2T8, and University of Toronto, Toronto M5S 1A7, Canada*

[12] *The Johns Hopkins University, Baltimore, Maryland 21218*

[13] *National Laboratory for High Energy Physics (KEK), Tsukuba, Ibaraki 305, Japan*

[14] *Lawrence Berkeley Laboratory, Berkeley, California 94720*

[15] *Massachusetts Institute of Technology, Cambridge, Massachusetts 02139*

[16] *University of Michigan, Ann Arbor, Michigan 48109*

[17] *Michigan State University, East Lansing, Michigan 48824*

[18] *University of New Mexico, Albuquerque, New Mexico 87131*

[19] *Osaka City University, Osaka 588, Japan*

[20] *Universita di Padova, Instituto Nazionale di Fisica Nucleare, Sezione di Padova, I-35131 Padova, Italy*

[21] *University of Pennsylvania, Philadelphia, Pennsylvania 19104*

[22] *University of Pittsburgh, Pittsburgh, Pennsylvania 15260*

[23] *Istituto Nazionale di Fisica Nucleare, University and Scuola Normale Superiore of Pisa, I-56100 Pisa, Italy*

[24] *Purdue University, West Lafayette, Indiana 47907*
[25] *University of Rochester, Rochester, New York 14627*
[26] *Rockefeller University, New York, New York 10021*
[27] *Rutgers University, Piscataway, New Jersey 08854*
[28] *Academia Sinica, Taiwan 11529, Republic of China*
[29] *Superconducting Super Collider Laboratory, Dallas, Texas 75237*
[30] *Texas A&M University, College Station, Texas 77843*
[31] *University of Tsukuba, Tsukuba, Ibaraki 305, Japan*
[32] *Tufts University, Medford, Massachusetts 02155*
[33] *University of Wisconsin, Madison, Wisconsin 53706*
[34] *Yale University, New Haven, Connecticut 06511*

References

References

[1] F. Dostoevsky, *The Brothers Karamazov*, translated from the original Russian by R. Pevear and L. Volokhonsky, Vintage Books, New York (1990).

[2] W. Shakespeare, *Antony and Cleopatra*, from First Folio edition (1623). Quotation contains one alteration from original (spelling update of "iudgement").

[3] J. Milton, *Samson Agonistes*, London (1671).

[4] G. Arnison, et al, (The UA1 Collaboration), *Experimental Observation of Isolated Large Transverse Energy Electrons with Associated Missing Energy at* $\sqrt{s} = 540\ GeV$, Phys. Lett. **122B**, 103-116 (1983); *Experimental Observation of Lepton Pairs of Invariant Mass around* $95\ GeV/c^2$ *at the CERN SPS Collider*, Phys. Lett. **126B**, 398-410 (1983).

[5] S.L. Glashow, *Partial Symmetries of Weak Interactions*, Nucl. Phys. **22**, 579-588 (1961).

[6] S. Weinberg, *A Model of Leptons*, Phys. Rev. Lett. **19**, 1264-1266 (1967).

[7] A. Salam, *Elementary Particle Physics*, ed. by N. Svarthold (Almqvist and Wiksells, Stockholm, 1968), p. 368.

[8] Y. Nambu, *Axial Vector Current Conservation in Weak Interactions*, Phys. Rev. Lett. **4**, 380-382 (1960).

[9] J. Goldstone, *Field Theories with Superconductor Solutions*, Nuovo Cim. **19**, 154-164 (1961).

[10] P.W. Higgs, *Broken Symmetries and the Masses of Gauge Bosons*, Phys. Rev. Lett. **13**, 508-509 (1964); *Spontaneous Symmetry Breakdown without Massless Bosons*, Phys. Rev. **145**, 1156-1163 (1966).

[11] G. 't Hooft, *Renormalization of Massless Yang-Mills Fields*, Nucl. Phys. **B33**, 173-199 (1971); *Renormalizable Lagrangian for Massive Yang-Mills Fields*, Nucl. Phys. **B35**, 167-188 (1971).

[12] E. Fermi, Ric. Sci. **4**, 491 (1933).

[13] O. Klein, in *Les Nouvelles Théories de la Physique*, Proceedings of a symposium held in Warsaw, May-June 1938 (Institut International de Coopération Intellectuelle, Paris, 1938), p. 6.

[14] C.N. Yang and R.L. Mills, *Conservation of Spin and Isotopic Gauge Invariance*, Phys. Rev. **96**, 191-195 (1954).

[15] A. Benvenuti, et al, *Observation of Muonless Neutrino-Induced Inelastic Interaction*, Phys. Rev. Lett. **32**, 800-803 (1974).

[16] The LEP Collaborations and the LEP Electroweak Working Group, *Updated Parameters of the Z^0 Resonance from Combined Preliminary Data of the LEP Experiments*, Proceedings from the Europhysics Conference on High Energy Physics, Marseille, 1993; and the 1993 International Symposium on Lepton-Photon Interactions at High Energies, Cornell.

[17] R. R. Wilson, *The Tevatron*, Phys. Today **10**, 23-30 (1977).

[18] F. Abe, et al (The CDF Collaboration), *The CDF Detector: An Overview*, Nucl. Instr. and Meth. **A271**, 387-403 (1988).

[19] CDF cross sectional view diagram courtesy Randy Keup. Diagram first appeared in published form in reference [43].

[20] F. Bedeschi, et al, *Design and Construction of the CDF Central Tracking Chamber*, Nucl. Instr. and Meth. **A268**, 50-74 (1988).

[21] *The CDF Vertex Detector*, internal note in progress, to be submitted to Nucl. Instr. and Meth. (1994).

[22] G. Ascoli, et al, *CDF Central Muon Detector*, Nucl. Instr. and Meth. **A268** 33-40 (1988).

[23] A. Gauthier, et al, *Design and Performance of Drift Chambers for the Central Muon Upgrade of the CDF Detector*, to be submitted to Nucl. Instr. and Meth.

[24] R. Wagner, et al, *Cosmic Ray Test of the CDF Central Calorimeters*, Nucl. Instr. and Meth. **A267** 330-350 (1988).

[25] L. Balka, et al, *The CDF Central Electromagnetic Calorimeter*, Nucl. Instr. and Meth. **A267** 272-279 (1988).

[26] S. Bertolucci, et al, *The CDF Central and Endwall Hadron Calorimeter*, Nucl. Instr. and Meth. **A267** 301-314 (1988).

[27] Y. Fukui, et al, *CDF End Plug Electromagnetic Calorimeter Using Conductive Plastic Proportional Tubes*, Nucl.. Instr. and Meth. **A267**, 280-300 (1988).

[28] *The CDF End Plug Hadronic Calorimeter*, internal note in progress, to be submitted to Nucl. Instr. and Meth.

[29] G. Brandenburg, et al, *An Electromagnetic Calorimeter for the Small Angle Regions of the Collider Detector at Fermilab*, Nucl. Instr. and Meth. **A267**, 257-271 (1988).

[30] S. Cihangir, et al, *The CDF Forward/Backward Hadron Calorimeter* , Nucl. Instr. and Meth. **A267**, 249-256 (1988)

[31] G. Drake, et al, *CDF Front End Electronics: The RABBIT System*, Nucl. Instr. and Meth. **A269**, 68-81 (1988).

[32] E. Barsoti, et al, *Fastbus Data Acquisition for CDF*, Nucl. Instr. and Meth. **A269**, 82-92 (1988).

[33] D. Amidei, et al, *A Two Level Fastbus Based Trigger System for CDF*, Nucl. Instr. and Meth. **A269**, 51-62 (1988).

[34] G. Ascoli, et al, *CDF Central Muon Level 1 Trigger Electronics*, Nucl. Instr. and Meth. **A269**, 63-67 (1988).

[35] G. W. Foster, et al, *A Fast Hardware Track Finder for the CDF Central Tracking Chambers*, Nucl. Instr. and Meth. **A269**, 93-100 (1988).

[36] D. Amidei, et al, *The Silicon Vertex Detector of the Collider Detector at Fermilab*, Fermilab Preprint FERMILAB-PUB-94-024-E, submitted to Nucl. Instr. and Meth. (January 1994).

[37] J.T. Carrol, et al, *The CDF Level 3 Trigger*, Nucl. Instr. and Meth. **A300**, 552-567 (1991).

[38] E.L. Berger, F. Halzen, C.S. Kim, S. Willenbrock, *Weak Boson Production at Fermilab Tevatron Energies*, Phys. Rev. D **40** 83-91 (1989).

[39] J.L. Rosner, M.P. Worah, T. Takeuchi, *Oblique Corrections to the W Width*, Phys. Rev. D **49**, 1363-1369 (1994).

[40] F. Abe, et al, (The CDF Collaboration), *Measurement of the Production and Muonic Decay Rate of W and Z Bosons in $p\bar{p}$ Collisions at $\sqrt{s}$ =1.8 TeV*, Phys. Rev. Lett. **69** 28-32 (1992).

[41] F. Abe, et al, (The CDF Collaboration), *Measurement of $\sigma B(W \to e\nu)$ and $\sigma B(Z \to e^+e^-)$ in $p\bar{p}$ Collisions at $\sqrt{s}$ = 1.8 TeV*, Phys. Rev. D **44**, 29-52 (1991).

[42] F. Abe, et al, (The CDF Collaboration), *Measurement of the Ratio $B(W \to \tau\nu)/B(W \to e\nu)$ in $p\bar{p}$ Collisions at $\sqrt{s}$ = 1.8 TeV*, Phys. Rev. Lett. **68**, 3403-3407 (1992).

[43] F. Abe, et al, (The CDF Collaboration), *Evidence for Top Quark Production in $p\bar{p}$ Collisions at $\sqrt{s}$ = 1.8 TeV*, Fermilab Preprint FERMILAB-PUB-94-097-E (April 1994). Submitted to Phys. Rev. D.

[44] b and c generated events courtesy Tae Y. Song.

[45] P. Derwent, D. Amidei, D. Gerdes, T. Song, for the CDF Collaboration, *$b\bar{b}$ Correlated Cross Sections*, presented by P. Derwent at the International Conference on High Energy Physics, Glasgow, Scotland (June 1994) and published in proceedings from said conference.

[46] b and c Fragmentation models courtesy the CLEO Collaboration.

[47] The W and Z Tree Level Monte Carlo Generator was first developed by Claudio Campagnari and is documented in several CDF publications, including references [40] and [41].

[48] A.D. Martin, W.J. Stirling, R.G. Roberts, *Parton Distributions Updated* , Phys. Lett. B **306** 145-150 (1993).

[49] A.D. Martin, W.J. Stirling, R.G. Roberts, *Parton Distributions of the Proton*, Rutherford Appleton Laboratory Preprint **RAL-94-055**, June 1994.

[50] W.J. Stirling, *private communication*, based on references [48] and [49], June 25, 1994.

[51] W.J. Stirling, *W, Z and top cross sections at 1.8 TeV*, memorandum, June 23, 1994.

[52] The central values for the plot of cross section vs. $\sqrt{s}$ are from references [50, 51]; the fractional theory errors in the plot are assumed constant as a function of $\sqrt{s}$, and are estimated herein based on numbers from references [49] and [51].

[53] R. Hamberg, T. Matsuura, W.L. van Neerven, *The Contribution of the Gluon-Gluon Subprocess to the Drell-Yan K-Factor*, Nucl. Phys. **B345**, 331-368 (1990); *A Complete Calculation of the Order α_s^2 Correction to the Drell-Yan K-Factor*, Nucl. Phys. **B359**, 343-405 (1991); W.L. van Neerven, E.B. Zijlstra, *The $O(\alpha_s^2)$ Corrected Drell-Yan K-Factor in the DIS and $\overline{MS}$ Schemes*, Nucl. Phys. **B382**, 11-62 (1992).

[54] The CTEQ Collaboration, *article to be published*; some information on the CTEQ parton distribution functions can be found in reference [63].

[55] F. Abe, et al, *The Charge Asymmetry in W-Boson Decays Produced in $p\bar{p}$ Collisions at $\sqrt{s} = 1.8$ TeV*, to be submitted to Phys. Rev. Lett. (1994).

[56] The W Mass value used here is the combined result from the CDF, DØ and UA2 experiments. The most recent results from the CDF and DØ data runs (the same run used in this analysis) are preliminary and are documented in the conference proceedings [57] and [58]. The former CDF results are published in reference [60]. The UA2 results are published in reference [59]. The combined value is listed in reference [57].

[57] D. Saltzberg (For the CDF Collaboration), *A Measurement of the W Mass using Electrons at CDF*, Proceedings from the 9th Topical Workshop on Proton-Antiproton Collider Physics, Tsukuba, Japan, 65-74 (October 1993).

[58] Q. Zhu (For the DØ Collaboration), *Measurement of the W Mass in the DØ Detector*, Proceedings from the 9th Topical Workshop on Proton-Antiproton Collider Physics, Tsukuba, Japan, 75-86 (October 1993).

[59] J. Alitti, et al, (The UA2 Collaboration), *An Improved Determination of the Ratio of W and Z Masses at the CERN $\bar{p}p$ Collider*, Phys. Lett. **B276**, 365-374 (1992).

[60] F. Abe, et al, (The CDF Collaboration), *Measurement of the W Boson Mass in 1.8 TeV $p\bar{p}$ Collisions*, Phys. Rev. D **43** 2070-2093 (1991).

[61] F. Abe, et al, (The CDF Collaboration), *Search for $W' \to e\nu$ and $W' \to \mu\nu$ in $p\bar{p}$ Collisions at $\sqrt{s} = 1.8$ TeV*, Phys. Rev. Lett. **67**, 2609-2613 (1991).

[62] F. Paige, S. Protopopescu, *IsaJet, A Monte Carlo Event Generator for pp and $p\bar{p}$ Reactions*, Brookhaven National Laboratory Report BNL-38034 (1986). IsaJet Version 7.00 (1994) was used, specially modified for the CDF analysis system and modified to include the parton distribution functions from references [48] and [54], using the CERN PDFLib interface package from reference [63].

[63] H. Plothow-Besch, *PDFLib: Nucleon, Pion and Photon Parton Density Functions and α_s Calculations*, CERN Documentation Note W5051-PDFLIB (November 1993). This reference provides the interface to the parton distribution functions found in references [48] and [54] (among others).

[64] F. Abe, et al, (The CDF Collaboration), *Measurement of the W Boson P_T Distribution in $p\bar{p}$ Collisions at $\sqrt{s} = 1.8$ TeV*, Phys. Rev. Lett. **66**, 2951-2955 (1991).

[65] F. Abe, et al, (The CDF Collaboration), *Measurement of the Z Boson P_T Distribution in $p\bar{p}$ Collisions at $\sqrt{s} = 1.8$ TeV*, Phys. Rev. Lett. **67**, 2937-2941 (1991).

[66] The tracking curvature resolution was developed in the internal note: R. Keup, *The Momentum Scale in Run 1a*, CDF Internal Note 2262 (October 1993). Results from this note are documented in reference [57].

[67] The CTC/VTX tracking efficiency was measured by Aesook Byon-Wagner and documented in the following internal collaboration reference: A. Byon-Wagner, *Vertexing/Tracking Efficiency*, Preliminary CDF Internal Note (August 1993).

[68] A. Byon-Wagner, et al, *Cosmic Filtering of Central Muon Events*, CDF Internal Note 1260 (August 1990).

[69] S. Abachi, et al, (The DØ Collaboration), *Search for the Top Quark in $p\bar{p}$ Collisions at $\sqrt{s} = 1.8$ TeV*, Phys. Rev. Lett. **72**, 2138-2142 (1994).

[70] E. Laenen, J. Smith, W.L. Van Neerven, Phys. Lett. *Title* **321B**, 254 (1994).

[71] F. Abe, et al, (The CDF Collaboration), *Measurement of the $p\bar{p}$ Total Cross Section at $\sqrt{s} = 546$ GeV and 1.8 TeV*, Fermilab Preprint FERMILAB-PUB-93-234-E (Nov 1993); Submitted to Phys. Rev. D.

[72] F. Abe, et al, (The CDF Collaboration), *Measurement of Small Angle $p\bar{p}$ Elastic Scattering at $\sqrt{s} = 546$ GeV and 1.8 TeV*, Fermilab Preprint FERMILAB-PUB-93-232-E (Aug 1993); Submitted to Phys. Rev. D.

[73] F. Abe, et al, (The CDF Collaboration), *Measurement of $p\bar{p}$ Single Diffractive Dissociation at $\sqrt{s} = 546$ GeV and 1.8 TeV*, Fermilab Preprint FERMILAB-PUB-93-233-E (Aug 1993); Submitted to Phys. Rev. D.

[74] BBC normalization procedure developed by Paul Derwent and documented in the following internal collaboration references: S. Belforte, P. Derwent, J. Marriner, C. Pilcher, *σ_{BBC} Derivation and Results*, CDF Internal Note 2361 (March 1994); *σ_{BBC} Updates*, CDF Internal Note 2535 (April 1994). The new normalization is first used in published form in reference [43].

[75] We thank Norman Gelfand of the Fermilab Accelerator Division for useful discussions and for his help in accessing the $p\bar{p}$ beam parameters.

[76] Alan Hahn, *Measuring the TeV Luminosity*, Tevatron Collider Luminosity Workshop, Fermi National Accelerator Laboratory, Batavia, Illinois (December 1993).

[77] C. Albajar, et al, (The UA1 Collaboration), *Measurement of the Ratio* $R = \sigma(W)BR(W \rightarrow \mu\nu)/\sigma(Z)BR(Z \rightarrow \mu\mu)$ *and* $\Gamma(W)$ *Total at the CERN* $\bar{p}p$ *Collider*, Phys. Lett. **B253**, 503-510 (1991).

[78] J. Alitti, et al, (The UA2 Collaboration), *A Measurement of the W and Z Production Cross Sections and a Determination of* $\Gamma(W)$ *at the CERN* $\bar{p}p$ *Collider*, Phys. Lett. **B276**, 365-374 (1992).

[79] Calculation of predicted Inverse Branching Ratio vs. Top Mass courtesy Paul Derwent, first appearing in reference [41].

[80] S. Kopp, *A Measurement of the Ratio* $R = \sigma \cdot B(p\bar{p} \rightarrow W \rightarrow e\nu)/B(p\bar{p} \rightarrow Z \rightarrow e^+e^-)$ *in* $p\bar{p}$ *Collisions at* $\sqrt{s} = 1800$ *GeV*, PhD. Thesis, University of Chicago (May 1994).

[81] The Particle Data Group, *Review of Particle Properties*, Phys. Rev. D **45**, III.39 (1992).